

# UC Riverside

## UC Riverside Electronic Theses and Dissertations

### Title

From Liquid Crystals to Viruses: Exploring Kinetics and Self-Assembly Dynamics

### Permalink

<https://escholarship.org/uc/item/7605j1j2>

### Author

Safdari, Mohammadamin

### Publication Date

2024

### Copyright Information

This work is made available under the terms of a Creative Commons Attribution-NonCommercial License, available at <https://creativecommons.org/licenses/by-nc/4.0/>

Peer reviewed|Thesis/dissertation

UNIVERSITY OF CALIFORNIA  
RIVERSIDE

From Liquid Crystals to Viruses: Exploring Kinetics and Self-Assembly Dynamics

A Dissertation submitted in partial satisfaction  
of the requirements for the degree of

Doctor of Philosophy

in

Physics

by

Mohammadamin Safdari

December 2024

Dissertation Committee:

Dr. Roya Zandi, Chairperson  
Dr. Umar Mohideen  
Dr. Thomas Kuhlman

Copyright by  
Mohammadamin Safdari  
2024

The Dissertation of Mohammadamin Safdari is approved:

---

---

---

Committee Chairperson

University of California, Riverside

## Acknowledgments

Attending graduate school is an extremely rewarding and hard experience. It's a period of development, friendship, and limitless learning chances. But without the people who supported me along the way, I could not have accomplished this. I would want to take this time to thank everyone who has supported and assisted me over the years.

First and foremost, I would like to sincerely thank Prof. Roya Zandi, my advisers, for her support, direction, and perceptive remarks. I am appreciative that I got to have her as a counselor, and I will never forget the influence she made on my life.

I would also like to thank my committee members Prof. Mohideen and Prof. Kuhlman for their time and effort in reviewing my dissertation.

I would like to extend my sincere gratitude to Prof. Paul Van der Schoot. It was a pleasure to work with him. His knowledge and perceptions strengthened my projects and given my research important new angles.

I am grateful to Alireza Ramezani, Sanaz Panahandeh, Yinan Dong, Siyu Li, Saeed Ahmad, Yankang Liu, Kevin Yang, and Shuyang Zhang for their friendship as well as for creating a cooperative and encouraging work atmosphere. Their friendliness, technical support, and enthusiasm for our research have contributed to making this experience truly great. The friendships I have developed with them are ones I will always treasure.

The past seven years in Riverside have been the most wonderful times of my life, spending time with my supportive friends. I would like to thank all of them: Alireza Ramzani, Arezoo Etesamirad, Mahdi Soleymani, Seyed Ali Lavasani, Fahimeh Arab, Mohsen Karimi, Reza Biglari, Mahsa Servati, Rasoul Ghadami, Marziye Jafariyazdani, Hoda Naghibi,

Valeh Ebrahimi, MohammadAmin Baniyasi, Sajjad Bahrami, Yasin Mazloumi, Maryam Shahcheraghi, Shirin Masoumi, Javad Saberi, Hora Sobhani, Ayoub Gheitasi, Raziye Jaber, Mahdi Kohansal, Sanaz Panahandeh, Shabnam Etemadi.

Above all, I would like to express my sincere gratitude to my mother Mahnaz Akhlaghi for her constant love and support. Her confidence in me and my abilities has helped me overcome some of the most challenging moments of my academic career. Although we may be physically separated by distance, her love and support will always remain with me. I appreciate everything that you have done. And to my brother Mohammadjavad, thank you for being in my life; you are definitely a blessing. I appreciate all of your support and affection.

Last but not least, I would like to say thank my wife, Zahra, who has been my constant source of support and encouragement throughout my PhD journey. Her unwavering love, patience, understanding, and culinary skills have given me courage. This achievement would not have been possible without her. Thank you for always being there for me; I love you!

## ABSTRACT OF THE DISSERTATION

From Liquid Crystals to Viruses: Exploring Kinetics and Self-Assembly Dynamics

by

Mohammadamin Safdari

Doctor of Philosophy, Graduate Program in Physics

University of California, Riverside, December 2024

Dr. Roya Zandi, Chairperson

This thesis explores three projects, offering valuable insights into the dynamic processes governing soft matter systems. The first project focuses on Tactoids, spindle-shaped droplets of a uniaxial nematic phase suspended in the coexisting isotropic phase. They are found in dispersions of a wide variety of elongated colloidal particles, including actin, fd virus, etc. Recent experiments on tactoids of chitin nanocrystals in water show that electric fields can very strongly elongate tactoids even though the dielectric properties of the coexisting isotropic and nematic phases only slightly differ. However, this observation contradicts the predictions of equilibrium theory as well as findings from Monte Carlo simulations that do not show this kind of extreme elongation to take place at all. We develop an equilibrium model, where the degree of bipolarity of the director field is free to adjust to optimize the sum of the elastic, surface, and Coulomb energies of the system. By means of a combination of a scaling analysis and a numerical study, we investigate the elongation and director field's behavior of the tactoids as a function of their size, the strength of the electric field, the surface tension, anchoring strength, the elastic constants, and the

electric susceptibility anisotropy. We find that tactoids cannot elongate significantly due to an external electric field, unless the director field is bipolar or quasibipolar and somehow frozen in the field-free configuration.

For the second project, we develop a kinetic theory and put forward a relaxational model based on the Oseen-Frank free energy of elastic deformation of a director field coupled to an anisotropic surface free energy. In our model, we use two reaction coordinates to describe the director field and the extent of elongation of the droplets and evaluate the evolution of both as a function of time following the switching on of an electric field. Depending on the relative magnitude of the fundamental relaxation rates associated with the two reaction coordinates, we find that the aspect ratio of the drops may develop a large and very long-lived overshoot before eventually relaxing to the much smaller equilibrium value. In that case, the response of the curvature of the director field lags behind, explaining the experimental observations. Our theory describes the experimental data reasonably well.

The third project focuses on the kinetic theory of virus capsid assembly based on Model A kinetics and studies the dynamics of the interconversion of virus capsids of different sizes triggered by a quench, that is, by sudden changes in the solution conditions. The work is inspired by *in vitro* experiments on functionalized coat proteins of the plant virus cowpea chlorotic mottle virus, which undergo a reversible transition between two different shell sizes ( $T = 1$  and  $T = 3$ ) upon changing the acidity and salinity of the solution. We find that the relaxation dynamics are governed by two-time scales that, in almost all cases, can be identified as two distinct processes. Initially, the monomers and one of the two types of capsids respond to the quench. Subsequently, the monomer concentration re-

mains essentially constant, and the conversion between the two capsid species completes. In the intermediate stages, a long-lived metastable steady state may present itself, where the thermodynamically less stable species predominate. We conclude that a Model A based relaxational model can reasonably describe the early and intermediate stages of the conversion experiments. However, it fails to provide a good representation of the time evolution of the state of assembly of the coat proteins in the very late stages of equilibration when one of the two species disappears from the solution. It appears that explicitly incorporating the nucleation barriers to assembly and disassembly is crucial for an accurate description of the experimental findings, at least under conditions where these barriers are sufficiently large.

# Contents

<b>List of Figures</b>	<b>xi</b>
<b>1 Effect of electric fields on the director field and shape of nematic tactoids</b>	<b>1</b>
1.1 Introduction . . . . .	1
1.2 Free Energy . . . . .	6
<b>2 Scaling Theory &amp; Results</b>	<b>15</b>
2.1 Scaling Theory . . . . .	15
2.1.1 Nearly spherical tactoids . . . . .	17
2.1.2 Elongated tactoids . . . . .	19
2.2 Numerical Results . . . . .	28
<b>3 Dynamics of elongation of nematic tactoids in an electric field</b>	<b>44</b>
3.1 Introduction . . . . .	44
3.2 Methods . . . . .	48
3.3 Results . . . . .	50
3.4 Comparison with Experiment . . . . .	59
<b>4 The Dynamics of Viruslike Capsid Assembly and Disassembly</b>	<b>65</b>
4.1 Introduction . . . . .	65
4.2 Equilibrium theory for capsid competition . . . . .	71
4.3 Kinetics of $T$ -number conversion . . . . .	76
<b>5 Results</b>	<b>82</b>
5.1 Numerical results . . . . .	82
5.2 Comparison with Experiment . . . . .	89
<b>6 Conclusion</b>	<b>97</b>
<b>7 Appendix</b>	<b>99</b>
.1 Bipolar coordinate . . . . .	99
.2 Some useful relations in the bispherical coordinate . . . . .	103
.3 Scaling theory . . . . .	104

.4	Free energy in bispherical coordinates . . . . .	106
.5	Small opening angle . . . . .	111
.6	Linear analysis . . . . .	113
.7	Complete capsid conversions . . . . .	116
	<b>Bibliography</b>	<b>120</b>

# List of Figures

1.1	(a) Polarized optical micrograph illustrating a number of nematic tactoids of different size and extinction pattern associated with the director-field conformation, in a solution of carbon nanotubes in chlorosulfonic acid at 1000 ppm. Arrows show the orientation of crossed polarizers. Schematics of (b) a bipolar tactoid with boojum surface defects at the poles, (c) a homogenous tactoid, and (d) an intermediate tactoid described by virtual boojums outside of the droplet. The parameters $R$ and $r$ represent the major and minor axes of the tactoid, respectively. Adopted from Ref. [6]. . . . .	3
1.2	Cross section (solid) and director field (dashed) of a tactoid presumed in our calculations. The droplet is cylindrically symmetric about its main axis. $2R$ denotes the length of a tactoid and $2r$ its width. $2\tilde{R}$ is the distance between the virtual boojums, which are the focal points of the (extrapolated) director field. For $R = \tilde{R}$ , the virtual boojums become actual boojums, <i>i.e.</i> , surface point defects. Also indicated is $\alpha$ , the opening angle of the spindle-shaped droplet, see also the main text. . . . .	9
2.1	Dependence of (a) the degree of bipolarness $y$ and (b) the aspect ratio $x$ of tactoids on the scaled volume $v$ in the presence of an electric field, according to the scaling theory. Blue solid line: the field strength $\Gamma$ is below the critical value $\Gamma_c$ , and the anchoring strength $\omega$ is somewhat larger than unity. The volumes $v_-$ and $v_+$ demarcate crossovers from quasi bipolar director fields to bipolar ones, and $v_<$ and $v_>$ those from elongated to spherical droplet shapes. Dash-dotted line: same curve, but now for $\Gamma = \Gamma_c$ . Dashed lines: $\Gamma > \Gamma_c$ . For fields above the critical field strength $\Gamma_*$ , the tactoids are always elongated provided the anchoring strength $\omega$ is sufficiently large. See the main text. The slopes of the various curves are listed in Tables I, II and III, and the values of the various crossover volumes and field strengths in Table IV. . . . .	25

2.2	Schematic “phase” diagram of director fields of tactoids in an external field. Plotted is the scaled volume $v$ versus the scaled field strength $\Gamma$ . Indicated are the crossovers between the five regimes, demarcated by the crossover volumes $v_-$ , $v_+$ , $v_<$ , $v_>$ , $v_*$ and $v_c$ . Expressions for the crossover volumes $v_-$ , $v_+$ , $v_<$ and $v_>$ , and the critical field strengths $\Gamma_c$ and $\Gamma_*$ , are listed in table IV. See also the main text. In the region bounded by $v_-$ and $v_c$ , tactoids with sufficiently large anchoring strength $\omega \gg 1$ are elongated with a director field that is quasi bipolar with a bipolarness $y$ that decreases with increasing volume. In the region bounded by $v_c$ and $v_+$ in the upper right-hand corner it is quasi bipolar with a bipolarness that increases with droplet volume. In region bounded by $v_-$ and $v_+$ in the upper left-hand corner the director field is for all intents and purposes bipolar. The tactoids are more or less spherical in the region bounded by $v_<$ and $v_>$ in the upper most left-hand corner, and elongated outside of that region, at least if $\omega \gg 1$ . The volume $v_c$ demarcates the crossover from decreasing to increasing bipolarness for quasi bipolar director fields, the volume $v_*$ that between decreasing aspect ratio to increasing aspect ratio. . . . .	27
2.3	The bipolarness $y$ of the director field of a tactoid in the presence of an electric field as a function of its dimensionless volume $v$ . Indicated by the different symbols are results for different values of the dimensionless electric field strength $\Gamma$ . The dimensionless anchoring strength is fixed at $\omega = 14$ and the dimensionless bend constant at $\kappa = 10$ . . . . .	29
2.4	Bipolarness $y$ of a tactoids as a function of the dimensionless electric field $\Gamma$ for a dimensionless volume $v = 10^7$ . Anchoring strength $\omega = 14$ and dimensionless bend constant $\kappa = 10$ . The solid line shows the scaling of $y$ as with $\Gamma^{0.5}$ . . . . .	30
2.5	Bipolarness $y$ of the droplet as a function of the dimensionless volume $v$ of tactoids in the presence of an electric field for different values of the dimensionless bend constants $\kappa$ indicated by the symbols. Anchoring strength $\omega = 14$ and dimensionless field strength $\Gamma = 100$ . . . . .	30
2.6	Bipolarness of a tactoid as a function of the dimensionless bend constant $\kappa$ in the presence of an electric field. Anchoring strength $\omega = 1.4$ , dimensionless field strength $\Gamma = 100$ and dimensionless volume $v = 10^{-4}$ . . . . .	31
2.7	Bipolarness $y$ of a tactoid as a function of the dimensionless volume $v$ in the presence of an electric field for different values of the anchoring strength, indicated by the symbols. Dimensionless field strength $\Gamma = 100$ and bend constant $\kappa = 10$ . . . . .	32
2.8	Bipolarness $y$ of a tactoid as a function of an anchoring strength $\omega > 1$ for small and large droplets, with dimensionless volumes $v = 10^{-2}$ and $v = 10^6$ . The dimensionless electric field strength is fixed at $\Gamma = 10$ and the dimensionless bend constant at $\kappa = 0$ . Indicated are also the scaling relations $y \sim \omega^{-0.43}$ for the small volume and $y \sim \omega^{-0.62}$ for the large volume. See also the main text. . . . .	33

2.9	Bipolarness $y$ of a tactoid as a function of anchoring strength ( $\omega < 1$ ) for small and large droplets, with dimensionless volumes $v = 10^{-2}$ and $v = 10^6$ . The dimensionless electric field strength is fixed at $\Gamma = 10$ and the dimensionless bend constant at $\kappa = 0$ . Indicated are also the scaling relations $y \sim \omega^{-0.51}$ and $y \sim \omega^{-0.52}$ . See also the main text. . . . .	34
2.10	Bipolarness $y$ as a function of anchoring strength $\omega$ for two different dimensionless bend constants of $\kappa = 0.1$ and $\kappa = 10^3$ . The dimensionless volume is set at a value $v = 10^{-4}$ . Also indicated are the scaling exponent of $-0.43$ for the small value of the bend constant and of $-0.90$ for the large value of the constant. See also the main text. . . . .	35
2.11	The aspect ratio $x$ of a tactoid as a function of the dimensionless volume $v$ for different (dimensionless) electric field strengths $\Gamma$ indicated by the symbols. The anchoring strength is set at $\omega = 14$ and the dimensionless bend constant at $\kappa = 10$ . . . . .	36
2.12	Aspect ratio $x$ and bipolarness $y$ of the director-field as a function of volume of a droplet in the absence of the electric field with $\Gamma = 0$ . Left vertical axis shows us the aspect ratio (we use blue triangles for the aspect ratio) and the right vertical axis shows us bipolarness (cross signs for bipolarness) and the red circles represent the experimental data of [40]. The best fit we obtain by eye are for the parameter values $\kappa = 20$ , $\omega = 1.3$ and $(K_{11} - K_{24})/\sigma = 4 \mu\text{m}$ . Notice that the largest tactoids are bipolar because $y \rightarrow 1$ and the smallest ones quasi bipolar with $y \approx 3$ . . . . .	38
2.13	Aspect ratio $x$ of tactoids as a function of volume $V$ in the presence of an electric field. We compare our numerical results with the experimental data of [40]. The best fit by eye we obtain taking as parameter values $\Gamma = 500$ , $\omega = 1.3$ , $\kappa = 20$ and $(K_{11} - K_{24})/\sigma = 4 \mu\text{m}$ . . . . .	39
2.14	Aspect ratio $x$ of a tactoid as a function of the dimensionless volume $v$ for different electric field strengths $\Gamma$ according to the restricted equilibrium model. See the main text. Anchoring strength $\omega = 14$ and bend elastic constant $\kappa = 10$ . 40	
2.15	Aspect ratio $x$ of a tactoid as a function of the electric field $\Gamma$ according to the restricted equilibrium model. Anchoring strength $\omega = 14$ and dimensionless bend constant $\kappa = 10$ . Different symbols show different volumes: triangles $v = 10^7$ , squares $v = 10^8$ and circles $v = 10^9$ . Indicated are also the scaling exponents, which are close to 0.4 for the three tactoid volumes. . . . .	41
3.1	Polarization microscopic images of the evolution in time of tactoids in an aqueous solution of chitin fibers, following the switching on and off of an AC electric field of root-mean-square magnitude of $E = 160 \text{ V mm}^{-1}$ and a frequency of 300 kHz. (a) to (e): The field is applied at time zero, and a collection of tactoids imaged at 0, 120, 210, 640, and 1080 seconds. (f) to (i): The field is switched off and the same tactoids are imaged after 230, 380, 530, and 820 seconds following the removal of the electric field. Figure reproduced with permission from Ref. [40]. . . . .	46

3.2	Aspect ratio $x$ of a tactoid as a function of dimensionless time $\tau$ for different values of the ratio $\gamma$ of the fundamental relaxation rates associated with the response of the director field and that of the aspect ratio. From top to bottom: $\gamma = 0.01$ (blue), $0.05$ (yellow), $0.1$ (green), $0.5$ (red), $1$ (purple), $10$ (brown), $50$ (light blue). The dimensionless volume of the droplet is $v = 10^5$ , the anchoring strength $\omega = 1.3$ , the dimensionless strength of the electric field $\Sigma = 65$ , and the ratio of the bend and splay elastic constants $\kappa = 20$ . . . . .	53
3.3	Bipolariness of a tactoid $y$ as a function of dimensionless time $\tau$ for the different values of the ratio $\gamma$ of the fundamental relaxation rates associated with the response of the director field and that of the aspect ratio. From bottom to top: $\gamma = 0.01$ (blue), $0.05$ (yellow), $0.1$ (green), $0.5$ (red), $1$ (purple), $10$ (brown), $50$ (light blue). The dimensionless volume of the droplet is $v = 10^5$ , the anchoring strength $\omega = 1.3$ , the dimensionless strength of the electric field $\Sigma = 65$ , and the ratio of the bend and splay elastic constants $\kappa = 20$ . . . . .	53
3.4	Aspect ratio $x$ of tactoid as a function of dimensionless time $\tau$ for different values of the dimensionless electric field strength $\Sigma = 10, 100, 200, 400, 1000, 2000$ (bottom to top). The dimensionless volume of the droplet is $v = 10^2$ , the anchoring strength $\omega = 1.3$ , and the ratio of the bend and splay elastic constants $\kappa = 20$ . The ratio of the fundamental relaxation rates was set at a value of $\gamma = 1/15$ . . . . .	54
3.5	Bipolariness of tactoid $y$ as a function of the dimensionless time $\tau$ for the different electric field strength $\Sigma = 10, 100, 200, 400, 1000, 2000$ (bottom to top). The dimensionless volume of the droplet is $v = 10^2$ , the anchoring strength $\omega = 1.3$ , and the ratio of the bend and splay elastic constants $\kappa = 20$ . The ratio of the fundamental relaxation rates was set at a value of $\gamma = 1/15$ . . . . .	55
3.6	Aspect ratio of tactoids $x$ as a function of time for the different dimensionless volume $v = 1, 310, 2340, 5780, 10000$ (bottom to top, central part). The electric field strength is $\Sigma = 65$ , the anchoring strength $\omega = 1.3$ , the ratio of the fundamental relaxation times $\gamma = 1/15$ and the ratio of the bend and splay elastic constants $\kappa = 20$ . . . . .	57
3.7	Bipolariness of tactoid $y$ as a function of the dimensionless time $\tau$ for different dimensionless volume $v = 1, 310, 2340, 5780, 10000$ (bottom to top on the right). The electric field strength is $\Sigma = 65$ , the anchoring strength $\omega = 1.3$ , the ratio of the fundamental relaxation times $\gamma = 1/15$ and the ratio of the bend and splay elastic constants $\kappa = 20$ . . . . .	57
3.8	The evolution of the aspect ratio $x$ as a function of the dimensionless time $\tau$ . The thick solid blue curve shows the response to switching on of the field at time zero. The curves in bold dash black, solid green, dotted red, dash-dotted pink, and thin dashed orange show what happens after shutting of the field. The dimensionless volume of the droplet is $v = 5 \cdot 10^3$ , the anchoring strength $\omega = 1.3$ , the strength of the electric field is $\Sigma = 425$ , the ratio of the bend and splay elastic constants $\kappa = 20$ , and the ratio of the fundamental relaxation rates $\gamma = 1/15$ . . . . .	59

3.9	Time evolution of the aspect ratio of three droplets of different dimensionless volumes $v$ , indicated by different colors (from top to bottom on the right): solid green for $v = 5780$ , dash-dotted orange for $v = 2340$ and dashed blue for $v = 310$ . Dots are experimental data points extracted from Ref. [40] and the drawn curves display our curve fits. We set the anchoring strength $\omega = 1.3$ , the ratio of bend to splay $\kappa = 20$ , the coefficient of the electric field strength $\Sigma = 190$ the ratio of relaxation rate $\gamma = 0.5$ and $\Gamma_\alpha = 1.6 \times 10^{-4} s^{-1}$ . The $r^2$ values for the quality of the curve fits are 0.61, 0.91, and 0.94 for dashed blue, dash-dotted orange and solid green curve respectively. . . . .	61
3.10	Aspect ratio of tactoids $x$ as a function of their volume $V$ in $\mu m^3$ for different times. a) Experimental findings for chitin in water, taken from [40]. b) Our theoretical predictions are based on the curve fitting. Parameter values for the theoretical predictions: $\omega = 1.3$ , $\kappa = 20$ , $\Sigma = 500$ , $\gamma = 1/20$ and $\Gamma_\alpha = 1.6 \times 10^{-4} s^{-1}$ . Results for the same moment in time are presented with the same color. Blue circles: 120 seconds, red triangles: 210 s, green squares: 410 s, black diamonds: 640 s, purple triangles: 850 s, orange triangles: 1080 s. See also the main text. . . . .	63
4.1	Relation between the fraction of protein in $T = 1$ capsids, $\eta_{1,\infty}$ , and that in $T = 3$ capsids, $\eta_{3,\infty}$ (4.6), for different values of the parameter $\alpha$ , according to Eq. (4.7). From top to bottom: $\alpha = 0.01$ (red), $\alpha = 0.63$ (purple), and $\alpha = 1.19$ (blue). The dashed lines demarcate the maximum value of $\eta_{3,\infty}$ for every value of $\eta_{1,\infty}$ for different maximum fractions of subunits present in capsids: $\eta_1 + \eta_3 = 1$ , $2/3$ and $1/3$ from top to bottom. The solid black line describes the special case $\eta_{3,\infty} = \eta_{1,\infty}$ . . . . .	74
4.2	The equilibrium fraction of proteins in $T = 1$ capsids, $\eta_1$ , and in $T = 3$ capsids, $\eta_3$ , as a function of the binding free energies of the two structures, $g_1$ and $g_3$ (see Eqs. 4.6 and 4.8). The orange surface shows $\eta_3$ and the blue surface shows $\eta_1$ . The dimensionless overall protein concentration was set at $c = 2 \cdot 10^{-5}$ , and the aggregation numbers for the two species set to values of $q_1 = 30$ and $q_3 = 90$ implying that the protein subunits are dimers of the coat protein. See also the main text. . . . .	77
4.3	The equilibrium fraction of protein in $T = 3$ capsids, $\eta_3 = \eta_{3,\infty}$ (solid lines), and $T = 1$ capsids, $\eta_1 = \eta_{1,\infty}$ (dashed lines), as a function of the difference in the dimensionless binding free energies $\Delta g \equiv g_3 - g_1$ . Shown are results for different values of $g_1$ , indicated by different colors, with purple for $g_1 = -14$ , green for $g_1 = -11$ , blue for $g_1 = -10.4$ , and red for $g_1 = -9$ . The dimensionless overall protein concentration was set at $c = 2 \cdot 10^{-5}$ , and the aggregation numbers set equal to $q_1 = 30$ and $q_3 = 90$ implying that the subunits are dimers of the coat proteins. Note that the transition does not occur at $\Delta g = 0$ . See also the main text. . . . .	77

4.4	Dimensionless fundamental relaxation rates $\lambda_{\pm}$ of the linearized kinetic equations (4.11) and (4.12) describing the conversion between $T = 1$ and $T = 3$ capsids as a function of the fraction of $T = 3$ capsids $\eta_3$ and kinetic coefficient $\Gamma = 1$ . The blue surface shows $\lambda_-$ and the orange one $\lambda_+$ . We set $q_3 = 3q_1 = 90$ to model CCMV capsid coat proteins that are present in solution as dimers. . . . .	80
5.1	Time evolution of the fraction of coat proteins $\eta_T$ in capsids with triangulation numbers $T = 1$ (red) and $T = 3$ (blue), as well as the fraction in monomers $1 - \eta_1 - \eta_3$ (green), as a function of dimensionless time $\tau$ . Indicated are results for different values of the ratio of assembly rates $\Gamma = 10$ (solid), $\Gamma = 1$ (dashed), and $\Gamma = 0.1$ (dotted). The initial conditions are $\eta_1(0) = \eta_3(0) = 0.40$ and the final states are $\eta_{1,\infty} = 0.80$ and $\eta_{3,\infty} = 0.18$ . We set $q_3 = 3q_1 = 90$ presuming the coat proteins to form dimers. See also the main text. . . . .	84
5.2	Time evolution of the fraction of coat proteins $\eta_T$ in capsids with triangulation numbers $T = 1$ (red) and $T = 3$ (blue), as well as the fraction in monomers $1 - \eta_1 - \eta_3$ (green), as a function of dimensionless time $\tau$ . Indicated are results for different values of the ratio of assembly rates $\Gamma = 10$ (solid), $\Gamma = 1$ (dashed), and $\Gamma = 0.1$ (dotted). The initial conditions are $\eta_1(0) = \eta_3(0) = 0.001$ and the final states are $\eta_{1,\infty} = 0.001$ and $\eta_{3,\infty} = 0.80$ . We set $q_3 = 3q_1 = 90$ presuming the coat proteins to form dimers. See also the main text. . . . .	86
5.3	Time evolution of the fraction of coat proteins $\eta_T$ in capsids with triangulation numbers $T = 1$ (red) and $T = 3$ (blue), as well as the fraction in monomers $1 - \eta_1 - \eta_3$ (green), as a function of dimensionless time $\tau$ . Indicated are results for different values of the ratio of assembly rates $\Gamma = 10$ (solid), $\Gamma = 1$ (dashed), and $\Gamma = 0.1$ (dotted). The initial conditions are $\eta_1(0) = 0.2$ and $\eta_3(0) = 0.6$ and the final states are $\eta_{1,\infty} = 0.6$ and $\eta_{3,\infty} = 0.2$ . We set $q_3 = 3q_1 = 90$ presuming the coat proteins to form dimers. See also the main text. . . . .	88
5.4	Time evolution of the fraction of monomers $1 - \eta_1 - \eta_3$ , as a function of dimensionless time $\tau$ . Indicated are results for different values of the ratio of assembly rates $\Gamma = 10$ (solid), $\Gamma = 1$ (dashed), and $\Gamma = 0.1$ (dotted). The initial conditions for $T = 3 \rightarrow T = 1$ (black) are $\eta_1(0) = 0.2$ and $\eta_3(0) = 0.6$ with final states $\eta_{1,\infty} = 0.6$ and $\eta_{3,\infty} = 0.2$ . For the $T = 1 \rightarrow T = 3$ (green) we swap the initial and final conditions of $T = 3 \rightarrow T = 1$ . We set $q_3 = 3q_1 = 90$ presuming the coat proteins to form dimers. See also the main text. . . . .	89
5.5	Fraction of protein in various species $\eta_T$ as a function of time $t$ in hours. Symbols: results from two data sets where following a quench $T = 3$ capsids convert into $T = 1$ capsids. Only the first 168 hours of the measurements of Timmermans <i>et al.</i> [134] are shown. The red, blue, and green lines indicate the fractions of $T = 1$ , $T = 3$ , and free subunits. See also the main text. . .	94

5.6	<p>Fraction of protein in various species <math>\eta_T</math> as a function of time <math>t</math> in hours. Symbols: results from two data sets where following a quench <math>T = 1</math> capsids convert into <math>T = 3</math> capsids. Only the first 168 hours of the measurements of Timmermans <i>et al.</i> [134] are shown. The red, blue, and green lines indicate the fractions of <math>T = 1</math>, <math>T = 3</math>, and free subunits. See also the main text. . .</p>	95
.1	<p>Parameters in bipolar coordinates: Each point <math>P</math> on a curve can be described by two parameters <math>\tau</math> and <math>\eta</math>. The angle <math>\eta</math> at point <math>P</math> sees the two foci while <math>\tau</math> is the logarithm of the ratio of distances to two fixed (focal) points. The values of <math>\eta</math> and <math>\tau</math> are constant on the red and blue circles, respectively. The three-dimensional bispherical coordinate can be obtained by rotating the bipolar coordinate around the axis connecting the two focal points <math>F_1</math> and <math>F_2</math>. The third coordinate in the bispherical coordinate is denoted by the azimuthal angle <math>\phi</math> not shown in the figure. Adopted from [61] . . . . .</p>	100
.2	<p>The relation between cylindrical coordinates and bispherical coordinates. For simplicity, we assume a point on the curve in the <math>\phi = 0</math> plane. . . . .</p>	101
.3	<p>Both <math>\xi</math> and <math>\tau</math> along with <math>\eta</math> are constant values on blue circles and red arcs respectively. <math>x_c</math> is the <math>x</math>-component of the right larger blue circle from the origin and the <math>R_c</math> is the radius of the same circle. . . . .</p>	102
.4	<p>Fraction of protein in various species <math>\eta_T</math> as a function of time <math>t</math> in hours. Symbols: results from two data sets where following a quench <math>T = 1</math> capsids convert into <math>T = 3</math> capsids. For two months of the measurements of Timmermans <i>et al.</i> [134] are shown. The red, blue, and green lines indicate the fractions of <math>T = 1</math>, <math>T = 3</math>, and free subunits. See the text in Appendix B. .</p>	118
.5	<p>Fraction of protein in various species <math>\eta_T</math> as a function of time <math>t</math> in hours. Symbols: results from two data sets where following a quench <math>T = 3</math> capsids convert into <math>T = 1</math> capsids. For two months of the measurements of Timmermans <i>et al.</i> [134] are shown. The red, blue, and green lines indicate the fractions of <math>T = 1</math>, <math>T = 3</math>, and free subunits. See also the text in Appendix B.</p>	119

# Chapter 1

## Effect of electric fields on the director field and shape of nematic tactoids

These results were published in [1]. I contributed to this work by performing the formal analysis, investigation, theoretical modeling, and visualizations.

### 1.1 Introduction

If an isotropic phase of rod-like colloidal particles undergoes a phase transition leading to a coexisting, uniaxially ordered nematic phase, then this typically happens via an intermediate stage characterized by an isotropic background phase in which are dispersed spindle-shaped droplets called tactoids, see Fig. 1.1. These tactoids eventually sediment and coalesce to form a macroscopic nematic phase, although this may take a very long time [2, 3,

4, 5, 6, 7]. First discovered in 1925 by Zocher in vanadium pentoxide sols [8], who also coined the term tactoids (“Taktoide” in German), they have since been observed in a plethora of molecular, polymeric and colloidal lyotropic liquid crystals. These include dispersions of tobacco mosaic virus particles [9], iron oxyhydroxide nanorods [10], polypeptides [11], carbon nanotubes [6, 12, 13], fd virus particles [14, 15], F-actin fibers [16], actin filaments [17, 18], chromonic liquid crystals [19], amyloid fibers [20] and cellulose nanocrystals [21, 22, 23, 24].

The peculiar, pointy and elongated shape of the tactoids, which reflects the underlying symmetry of the nematic phase, was initially explained in terms of the surface anchoring of the director field, presumed to be uniform [25]. The fact that the degree of elongation depends on the volume of the droplets, and that polarization microscopic images show their director field to be bipolar rather than uniform, at least if they are sufficiently large [6], reveals that this explanation is incomplete. In a bipolar configuration the director field conforms to a bi-spherical coordinate system, illustrated in Fig. 1.1 and in more detail in Fig. 1.2. If the focal points of the coordinate system reside on the poles of the droplets, representing proper surface defects known as boojums [26], the director field is then properly bipolar.

Theoretical studies of van Kaznacheev *et al.* [27, 28] and Prinsen *et al.* [29, 30, 31] have revealed that the boojums are by and large virtual, situated outside of the droplet in an extrapolated director field, and that the director field is almost always incompletely bipolar and hence only quasi bipolar [5, 27, 29, 32, 33, 34]. The smaller the droplet, the further the virtual boojums move away from the poles of the droplets and the more strongly the

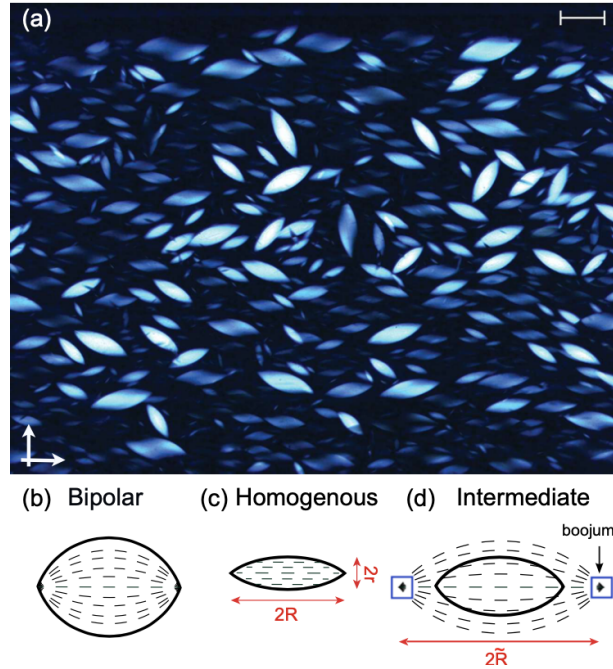


Figure 1.1: (a) Polarized optical micrograph illustrating a number of nematic tactoids of different size and extinction pattern associated with the director-field conformation, in a solution of carbon nanotubes in chlorosulfonic acid at 1000 ppm. Arrows show the orientation of crossed polarizers. Schematics of (b) a bipolar tactoid with boojum surface defects at the poles, (c) a homogenous tactoid, and (d) an intermediate tactoid described by virtual boojums outside of the droplet. The parameters  $R$  and  $r$  represent the major and minor axes of the tactoid, respectively. Adopted from Ref. [6].

director field resembles that of a spatially uniform director field that represents its ground state. The full crossover from uniform to bipolar director fields has only recently been observed experimentally for tactoids in dispersions of carbon nanotubes in chlorosulfonic acid, both in bulk and sessile, that is, on planar surfaces [6, 13], see Fig. 1.1.

What has emerged, is a picture in which there are two length scales that predict the structure and shape of tactoids of a certain size. Following de Gennes, these length scales may perhaps be called extrapolation lengths, and are defined as ratios of elastic constants and surface energies [35]. These surface energies are the bare surface tension between the

isotropic and nematic phases, and the surface anchoring energy penalising a deviation from the preferred planar anchoring of the director field of elongated colloidal particles along the interface [36]. Droplets that are smaller than the smallest of these two length scales, that is, the length scale associated with the surface anchoring, tend to have a uniform director field and elongated shape. If a droplet is larger than the larger extrapolation length, which is associated with the bare surface tension, then it tends to be bipolar and nearly spherical. Droplets of a size in between these two length scales remain elongated but have director field in between uniform and bipolar, see Fig. 1.1.

The situation becomes more complex if yet another length scale enters the stage. For instance, if the nematic is not uniaxial but chiral, that is, cholesteric, then the cholesteric pitch interferes with these two length scales. This gives rise to an additional regime separating uniaxial from twisted nematic (cholesteric) configurations [31, 37, 38, 39]. The same is true if an external electric or magnetic field is applied to nematic rather than cholesteric tactoids. The impact of a magnetic field on tactoids of vanadium pentoxide fibers dispersed in water was investigated experimentally and theoretically by Kaznacheev *et al.*, who found that an externally applied magnetic field stretches tactoids, at least if they are sufficiently large [27]. This, indeed, points at the existence of another pertinent length scale.

The existence of such a length scale was recently confirmed by Metselaar *et al.*, who studied the impact of a high-frequency electric AC field on tactoids of chitin fibers dispersed in water [40]. These authors find very large elongations of tactoids in the presence of an electric field, with aspect ratios increasing from about two in zero field to about twenty for droplets larger than some critical size. Their numerical simulations, based on the lattice

Boltzmann method, mimic this observation, showing that in order to obtain a very large length-to-breadth or aspect ratio for the droplets, a large anchoring strength is required. Interestingly, large anchoring strengths are also known to lead to quite elongated tactoids in zero field, but the effect is apparently somehow dramatically enhanced by an electric field that arguably aligns the fibers and hence also the director field along the field direction.

If the planar anchoring of the director field to the interface between the coexisting isotropic and nematic phases were absolutely rigid and strictly bipolar, then the theory of Kaznacheev and collaborators [27] would predict an in principle unbounded growth of the length of the tactoids with increasing electric or magnetic field strength.<sup>1</sup> Actually, the chitin tactoids are not actually strictly bipolar but quasi bipolar, in which case the anchoring would be imperfect.

Interestingly, in the lattice Boltzmann simulations of Metselaar *et al.*, the director field seems to respond to the external alignment field not by keeping the bi-spherical geometry and simply stretching it, as is presumed in the calculations of Kaznacheev and co-workers. Instead, the director field seems to become uniform in the center of the droplet to bend sharply close to the interface in order to accommodate planar anchoring [41]. This is highly surprising, because such a change in the geometry of the director field would require very large local deformation of the director field and associated with that would be a large elastic free energy of deformation. We should perhaps not exclude the possibility that the limited spatial resolution of the simulations produces such a strong director field deformation [41].

---

<sup>1</sup>Tactoids can also be stretched by the effect of an elongational flow field, as was recently shown by H. Almohammadi, M. Bagnani and R. Mezzenga, Flow-induced order-order transitions in amyloid fibril liquid crystalline tactoids, Nat. Comm. 11 (2020), 5416.

## 1.2 Free Energy

We consider a nematic droplet suspended in an isotropic fluid medium. The free energy  $F$  describing the droplet in an external electrical field consists of a sum of three terms,

$$F = F_E + F_S + F_C, \quad (1.1)$$

representing the Frank elastic free energy associated with a potentially deformed director field  $F_E$ , an interfacial free energy  $F_S$ , and a Coulomb energy  $F_C$ .

Focusing on twist-free bipolar director fields, the Frank elastic free energy of the droplet reads [42],

$$F_E = \int \left[ \frac{1}{2} K_{11} (\vec{\nabla} \cdot \vec{n})^2 + \frac{1}{2} K_{33} \left( \vec{n} \times (\vec{\nabla} \times \vec{n}) \right)^2 - \frac{1}{2} K_{24} \vec{\nabla} \cdot \left( \vec{n} \vec{\nabla} \cdot \vec{n} + \vec{n} \times (\vec{\nabla} \times \vec{n}) \right) \right] dV, \quad (1.2)$$

where the integration is over the entire volume  $V$  of the droplet,  $\vec{n}$  represents the position-dependent director field, and  $K_{11}$ ,  $K_{33}$  and  $K_{24}$  are the elastic moduli of the splay, bend and saddle-splay deformations, respectively [35]. Here, we do not allow for twisted director fields that may arise if the bend elastic constant is sufficiently small [38]. Note that these parity-broken structures are anyway suppressed if the tactoids are elongated [31].

Within a Rapini-Papoular approximation [43], the interfacial free energy can be written as

$$F_S = \sigma \int \left[ (1 + \omega (\vec{q} \cdot \vec{n})^2) \right] dA, \quad (1.3)$$

where  $\sigma$  is the interfacial tension between the nematic phase of the droplet and isotropic medium,  $\omega$  is a dimensionless anchoring strength and the integration is over the interfacial area  $A$  of the droplet. We presume that  $\omega > 0$ , implying that the anchoring penalises a director field  $\vec{n}$  that is not parallel to the interface, that is, at right angles to the surface normal  $\vec{q}$ . Rod-like particles prefer a planar anchoring of the nematic at the interface with the coexisting isotropic phase for entropy reasons [3, 36, 44]. In principle, both the surface tension and anchoring strength could depend on the curvature of the interface, but even for very small droplets the effect seems to be very small [34].

Finally, the Coulomb energy of a nematic droplet in an electric field  $\vec{E}$  can be written as [35, 45],

$$F_C = -\frac{1}{8\pi}\epsilon_a \int (\vec{n} \cdot \vec{E})^2 dV, \quad (1.4)$$

where  $\epsilon_a = \epsilon_{\parallel} - \epsilon_{\perp} \geq 0$  is the dielectric susceptibility anisotropy of the dispersion of rod-like particles, which can be described as a second-rank tensor with components  $\epsilon_{\parallel}$  and  $\epsilon_{\perp}$  parallel and perpendicular to the droplet axis [46]. Note that we ignore a potential permanent dipole moment on the particles and that we have not explicitly written a constant term that is not a function of the director field. It is important to note that both  $\epsilon_{\parallel}$  and  $\epsilon_{\perp}$  are not all that different from the dielectric constant of the isotropic phase, because the dielectric response of the suspension is dominated by that of the solvent [40]. This means that any elongation of the droplets caused by an electric field is not due to a difference between the dielectric properties of the isotropic and nematic phases, as would be the case for a thermotropic nematic tactoid suspended in a polymeric fluid [47], but due to the anisotropy of the dielectric response of the nematic phase itself.

Having collected all contributions to the free energy, we need to address an issue of some contention, which is whether or not the susceptibility anisotropy, the surface energies and the elastic constants depend on the strength of the electric field. In principle, they do. The reason is that these quantities depend on the level of alignment of the particles in the coexisting isotropic and nematic phases [36, 48, 49, 50]. We also note that strictly speaking the isotropic phase becomes paranematic in the presence of an alignment field. In fact, the isotropic-to-nematic phase transition ends in a critical point, at which both the interfacial tension and anchoring should vanish [7, 51, 52, 53]. To keep our analysis as simple as possible, and within the philosophy of linear response theory, we shall ignore any impact of the electric field on the elastic constants and surface energies, and presume the external field in some sense to be sufficiently weak not to affect these quantities, yet sufficiently strong to deform the tactoids.

To find the equilibrium shape and director-field configuration of tactoids, we would need to solve the appropriate Euler-Lagrange equations that result from a minimization of the free energy, given in Eq. 1.1. The minimization is with respect to the director field  $\vec{n}(\vec{r})$ , which depends on the spatial coordinate  $\vec{r}$  as well as on the droplet shape. This has to be done subject to the conditions of a constant droplet volume and a constant unit length of the director,  $|\vec{n}| \equiv 1$  [42], which produces a quite complex mathematical problem, also numerically, in view of the free boundary [29, 38].

Hence, we follow the earlier work of Kaznacheev *et al.* [27, 28] and Prinsen *et al.* [29, 30, 31], and restrict the geometry of both the director field and droplet shape. For the shapes of the droplets we use circle sections rotated about their chord, producing potentially

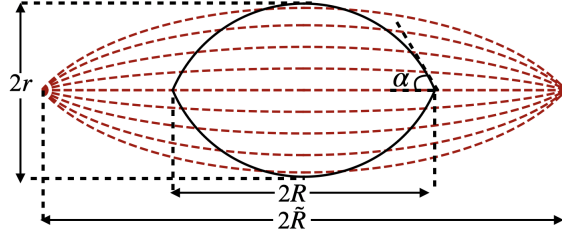


Figure 1.2: Cross section (solid) and director field (dashed) of a tactoid presumed in our calculations. The droplet is cylindrically symmetric about its main axis.  $2R$  denotes the length of a tactoid and  $2r$  its width.  $2\tilde{R}$  is the distance between the virtual boojums, which are the focal points of the (extrapolated) director field. For  $R = \tilde{R}$ , the virtual boojums become actual boojums, *i.e.*, surface point defects. Also indicated is  $\alpha$ , the opening angle of the spindle-shaped droplet, see also the main text.

elongated droplets with sharp ends that are very similar to the tactoid shapes found in a wide variety of experiments, including those of Metselaar *et al.* [40]. We are aware that the equilibrium shape of the poles is a cusp if  $0 \leq \omega < 1$  and the director field (nearly) uniform, which in that case has a more rounded form. However, as we showed in [29], the free energy difference between the exact Wulff shape, the spindle shape and ellipsoids of revolution is minute for  $\omega < 1$ , so we deem the approximation not to be a grave one.

For the director field we employ a bispherical coordinate system first used by Williams to describe spherical bipolar droplets [38], and more recently by Prinsen *et al.* [29, 30, 31], Jamali *et al.* [6, 13] and Kaznacheev *et al.* [27, 28] for elongated bipolar droplets. We do not fix the position of the foci of the bispherical director field to the poles of the tactoid to allow for a smooth interpolation between a uniform and bipolar director field, although we do prescribe them to reside on the main axis of revolution of the tactoid. See also Fig. 1.2.

Within this prescription, the shape and director-field configuration of a tactoid is completely described by two parameters, at least if the volume of the droplet is known. These two parameters are the opening angle  $\alpha$  and the ratio  $y \equiv \tilde{R}/R$  of the distance between the virtual boojums,  $2\tilde{R}$ , and length of the droplet,  $2R$ . The former quantity describes the aspect ratio  $x \equiv R/r = \cot(\alpha/2)$  of the droplet, with  $r$  the half width of the droplet, and the latter the degree of “bipolariness” of the director field. For a spherical droplet, we have  $x = 1$  and  $\alpha = \pi/2$ , whilst for a strongly elongated one  $x \gg 1$  and  $\alpha \ll 1$ . For a tactoid with a uniform director field  $y \gg 1$ , and for a bipolar tactoid  $y \rightarrow 1$ , see also Fig. 1.2. We note that the quantities  $x$  and  $y$  will explicitly contribute to the scaling theory presented in the following section.

It turns out practical to render the free energy dimensionless, and define  $f = f(\alpha, y) \equiv \sigma F / (K_{11} - K_{24})^2$ . The optimal free energy minimizes  $f$  with respect to the opening angle  $\alpha$  or aspect ratio  $x$  and the bipolariness  $y$ , keeping the volume  $V$  of the droplet constant. Let the dimensionless volume be defined as  $v \equiv V (\sigma / (K_{11} - K_{24}))^3$ . The dimensionless free energy  $f$  can then be written as a sum of surface and volume terms

$$\begin{aligned}
f(\alpha, y) = & v^{2/3} \phi_v^{-2/3}(\alpha) [\phi_\sigma(\alpha) + \omega \phi_\omega(\alpha, y)] \\
& + v^{1/3} \phi_v^{-1/3}(\alpha) [\phi_{11}(\alpha, y) + \kappa \phi_{33}(\alpha, y)] \\
& - v \phi_v^{-1}(\alpha) \Gamma \phi_C(\alpha, y),
\end{aligned} \tag{1.5}$$

where we refer to the Supplementary Information (SI) for details. The first line represents the two surface contributions, the second line corresponds to the three types of elastic deformation of the director field, and the last is related to the Coulomb energy. Here,

$\kappa \equiv K_{33}/(K_{11} - K_{24})$  measures the magnitude of the bend elastic constant relative to the effective splay constant, and  $\Gamma = \frac{1}{8\pi}\epsilon_a E^2 \sigma^{-2} (K_{11} - K_{24})$  is the appropriate quantity to probe the impact of the electric field relative to the surface tension and elastic deformation.

For the case of lyotropic nematics of rod-like particles, we typically have  $\sigma \approx 10^{-7} - 10^{-6}$  N m<sup>-1</sup> for the surface tension [54], and  $K_{33}/K_{11} \approx 1 - 10^2$  and  $K_{11} \approx 10^{-12} - 10^{-11}$  N for the elastic constants [13, 29, 55, 56, 57]. Dimensionless anchoring strengths  $\omega$  are typically in the range from about 1 to 10 [6, 12, 28, 30].

All three terms are renormalized by a function measuring how the opening angle  $\alpha$  affects the droplet volume for a given aspect ratio  $x$ . The common factor is given by

$$\phi_v(\alpha) = \frac{7\pi}{3} + \frac{\pi}{2} \left( \frac{1 - 4\alpha \cot \alpha + 3 \cos 2\alpha}{\sin^2 \alpha} \right). \quad (1.6)$$

The first line of Eq. 1.5 consists of the sum of a contribution from the bare surface tension,

$$\phi_\sigma(\alpha) = 4\pi \left( \frac{1 - \alpha \cot \alpha}{\sin \alpha} \right), \quad (1.7)$$

and a term originating from the anchoring of the director field to the interface,

$$\begin{aligned} \phi_\omega(\alpha, y) &= \frac{\pi}{2} (y^2 - 1)^2 \sin^3 \alpha \\ &\times \int_0^\pi d\xi \left[ \frac{\sin^2 \xi \cos^2 \xi}{N(y, \xi, \alpha) (1 + \sin \xi \cos \alpha)^3} \right], \end{aligned} \quad (1.8)$$

for which we have not been able to obtain an explicit expression. Here,

$$N(y, \xi, \eta) = \left( \sin \xi \cos \eta + \frac{1}{2} Z(\xi, \eta) (y^2 - 1) \right)^2 + y^2 \sin^2 \xi \sin^2 \eta, \quad (1.9)$$

and

$$Z(\xi, \eta) = 1 + \sin \xi \cos \eta. \quad (1.10)$$

Note that in Eq. 1.8, we inserted  $\eta = \alpha$  to obtain the expression for  $N$  in Eq. 1.9.

The contribution of the splay and saddle-splay deformation to the Frank elastic energy also gives rise to an integral that we have also not been able to solve analytically,

$$\begin{aligned} \phi_{11}(\alpha, y) = & 8\pi \int_0^\pi d\xi \int_0^\alpha d\eta \sin^2 \xi \cos^2 \xi \sin \eta \\ & \times \frac{1}{N(y, \xi, \eta) (1 + \sin \xi \cos \eta)^3}, \end{aligned} \quad (1.11)$$

where we note that within our family of bispherical director fields, the saddle-splay deformation merely renormalizes the contribution from the splay deformation, giving rise to an effective splay constant that is the difference of the splay and bend-splay constants, explaining the scaling of the free energy that we introduced above in terms of this difference [29, 30]. The contribution of the bend elastic deformation reads

$$\begin{aligned} \phi_{33}(\alpha, y) = & 8\pi \int_0^\pi d\xi \int_0^\alpha d\eta \sin^4 \xi \sin^3 \eta \\ & \times \frac{1}{N(y, \xi, \eta) (1 + \sin \xi \cos \eta)^3}. \end{aligned} \quad (1.12)$$

Finally, the free energy of the interaction of the nematic droplet with an electric field yields an even more daunting integral,

$$\begin{aligned} \phi_C(\alpha, y) = & 8\pi \int_0^\pi d\xi \int_0^\alpha d\eta \frac{\sin^2 \xi \sin \eta}{(1 + \sin \xi \cos \eta)^3} \\ & \times \frac{(y^2 Z^2 + \sin^2 \xi \sin^2 \eta - \cos^2 \xi)^2}{N(y, \xi, \eta) (1 + \sin \xi \cos \eta)^2}. \end{aligned} \quad (1.13)$$

Details of the derivation of all these expressions can be found in the SI.

The various integrals can be solved explicitly for the cases  $y = 1$  and  $y \rightarrow \infty$ , but so far have eluded analytical evaluation for the general case  $y \geq 1$  [27, 29]. Hence, we need to take recourse to a numerical evaluation and minimization with respect to the opening angle  $\alpha$  and the bipolarity  $y$ . We recall that there is a one-to-one mapping between the opening angle  $\alpha$  and the aspect ratio  $x$  of the tactoids. From Eq. 1.5 we deduce that our parameter space is quite substantial: (i) the scaled volume of the droplets,  $v$ , (ii) the dimensionless anchoring strength  $\omega$ , (iii) the ratio of the bend and splay elastic constants  $\kappa$ , and (iv) the dimensionless strength of the magnetic field  $\Gamma$ .

Before numerically solving the pertinent equations in Section IV, we first analyze in Section III the problem from the perspective of scaling theory for (nearly) spherical and (highly) elongated droplets. This allows us to demarcate the crossovers between the various parameter regimes, and find the scaling exponents relevant to the behavior of the droplet shape and director field. As we shall see in Section IV, our scaling theory and our variational theory are consistent with each other.

For those not interested in the full scaling analysis, which is rather technical in nature and details transitions between no fewer than five regimes, we refer to Figs. 2.1 and

2.2 that summarize our main findings. The scaling relations that we find are summarized in Tables I, II and III, and Table IV lists all crossover volumes and external field strengths.

## Chapter 2

# Scaling Theory & Results

### 2.1 Scaling Theory

Rather than getting the exact expression for the free energy Eq. 1.5, we may also estimate the equilibrium shape and director-field configuration of a tactoid by applying simple geometric arguments or resorting to asymptotic relations valid for the various integrals that we introduced in the preceding section. We assume that the droplet looks like a spindle with the short axis  $r$  and the long axis  $R \geq r$ , and that its director-field is quasi bipolar, *i.e.*, the director field converges outside the droplet to virtual point defect or boojums, see Fig. 1.2. The (half) distance between the (virtual) defects is  $\tilde{R} \geq R$ .

Referring to the free energy functions Eqs. 1.1-1.4, we notice that the elastic and electric-field contributions must be proportional to the droplet volume  $V \propto Rr^2$ , while the surface contributions must be proportional to the area of the droplet  $S \propto rR$ . Following Prinsen *et al.* [30], we argue that the radius of curvature of a bend deformation must scale as  $\tilde{R}^2/r$  and that of the splay as  $\tilde{R}^2/R$ . Furthermore, the anchoring strength term,

proportional to  $(\vec{q} \cdot \vec{n})^2$ , scales as  $(r^2/R^2)(1 - R^2/\tilde{R}^2)^2$  [13, 30], as we in fact also show in the SI. Finally, the field term  $(\vec{E} \cdot \vec{n})^2$  is proportional to  $E^2 r^2 R^2 / \tilde{R}^4$ .

As already alluded to in the previous section, there are two quantities that a nematic droplet can optimize in order to lower its free energy: the aspect ratio  $x = R/r \geq 1$  and the bipolarity  $y = \tilde{R}/R \geq 1$ . The dimensionless free energy of a droplet with aspect ratio  $x$  and bipolarity  $y$  reads within our scaling ansatz

$$f(x, y) \sim v^{2/3} x^{1/3} (1 + \omega x^{-2} (1 - y^{-2})^2) + v^{1/3} y^{-4} x^{-4/3} (1 + \kappa x^{-2}) + \Gamma v x^{-2} y^{-4}, \quad (2.1)$$

where we have ignored all constants of proportionality. The values of the dimensionless anchoring strength  $\omega$ , bend constant  $\kappa = K_{33}/(K_{11} - K_{24})$ , electric field strength  $\Gamma = \frac{1}{8\pi} \sigma^{-2} \epsilon_a E^2 (K_{11} - K_{24})$  and volume  $v \equiv V \sigma^3 / (K_{11} - K_{24})^3$  determine what values of  $x$  and  $y$  minimize the free energy  $f$ . The first term in Eq. 2.1 represents the surface free energy, the second term the elastic deformation and the last term the interaction of the droplet with the external electric field. Notice that the various terms can also be derived from Eq. 1.1 by applying a formal expansion for small  $\alpha \simeq x^{-1}$ , and keeping only the leading order term of each contribution. We refer to SI for details.

As we shall see, there are always two terms that dominate the shape and director field of a tactoid: either the surface and elastic energy, or the surface and Coulomb energy. This is a result of the different scaling with the dimensionless volume  $v$ :  $v^{1/3}$  for the elastic free energy,  $v^{2/3}$  for the interfacial free energy and  $v$  for the Coulomb free energy. This means that droplet size crucially determines the shape and director field behavior of tactoids.

It is important to note at this point that the specific form of our scaling ansatz for the free energy, Eq. 2.1, automatically ensures that  $y \geq 1$  but not that  $x \geq 1$ . The former follows directly from the observation that the first term has a minimum for  $y = 1$ , whilst all the other terms decrease as  $y > 0$  increases. Further, Eq. 2.1 does *not* hold for lens-shaped tactoids, that is, for  $x < 1$ . Indeed, the surface free energy for  $x \ll 1$  would require a term proportional to an area that scales as  $r^2$  rather than the  $Rr$  that is valid for  $x \geq 1$ . Similar arguments hold for the elastic and Coulomb terms [33, 58, 59].

In order to deal with the fact that our free energy does not automatically ensure the condition that  $x \geq 1$  for  $\omega \geq 0$ , we have to separate the case of elongated droplets with  $x \gg 1$  from that of spheroidal droplets with  $x \approx 1$ . In fact, for  $\omega < 0$  the tactoids become lens-shaped with  $x < 1$ , a case we do not consider in this work as it has been dealt with elsewhere. [33, 58, 59]. The case  $x \approx 1$  can be investigated by putting  $x = 1$  in the free energy, and not optimizing with respect to both  $x$  and  $y$ , but only with respect to  $y$ . The crossover from elongated to spheroidal emerges automatically from our analysis, as we shall see. In what follows, we first analyze the the simpler case for which the aspect ratio is close to unity, and next consider the case where the aspect ratio is significantly larger than unity.

### 2.1.1 Nearly spherical tactoids

As we shall see in the next subsection, tactoids are always nearly spherical if the anchoring strength  $\omega$  is about unity or smaller (see Eq. 1.3), irrespective of the value of the scaled volume  $v$  and that of the scaled strength of the electric field  $\Gamma$ . If  $\omega \gg 1$ , then the droplets become spherical only for a range volumes that we will specify below, and then only if the field strength is below some critical value.

Minimizing the free energy  $f(1, y)$  for nearly spherical droplets with respect to the bipolarity  $y$ , we find for its optimal value

$$y^2 \simeq 1 + \omega^{-1}(1 + \kappa)v^{-1/3} + \Gamma\omega^{-1}v^{1/3}. \quad (2.2)$$

This expression immediately highlights the importance of the volume of the droplet. The director field is uniform, corresponding to  $y \gg 1$ , either if  $\omega^{-1}(1 + \kappa)v^{-1/3} \gg 1$  or  $\Gamma\omega^{-1}v^{1/3} \gg 1$ . In other words, if  $v \ll v_- = \omega^{-3}(1 + \kappa)^3$  or  $v \gg v_+ = \omega^3\Gamma^{-3}$ . For droplet volumes  $v_- \leq v \leq v_+$ , the director field is (quasi) bipolar, and  $y \approx 1$ .

Thus, we find that there are potentially three different regimes and two critical volumes that dictate the behavior of the droplet. For  $v \ll v_-$ , we obtain the scaling relation

$$y \sim v^{-1/6}\omega^{-1/2}(1 + \kappa)^{1/2}, \quad (2.3)$$

whilst for  $v \gg v_+$ , we have

$$y \sim v^{1/6}\Gamma^{1/2}\omega^{-1/2}. \quad (2.4)$$

Notice that the exponents of  $-1/6$  for volumes  $v \ll v_-$  and of  $+1/6$  for  $v \gg v_+$  are universal.

A summary of these results is given in Table 2.1.

We notice that as the electric field strength increases,  $v_+$  decreases and the two critical volumes merge into one critical volume:  $v_- = v_+$ . This happens at a critical electric field  $\Gamma_c \simeq \omega^2(1 + \kappa)^{-1}$ . If  $\Gamma \geq \Gamma_c$ , the bipolarity  $y$  is always greater than unity for any size of the droplet, and the droplet is never fully bipolar. The crossover of a decreasing bipolarity to an increasing one with increasing volume then happens at a critical volume

	$v < v_-$	$v_- < v < v_+$	$v_+ < v$
$\Gamma \leq \Gamma_c$	$y \sim \omega^{-1/2} v^{-1/6}$	$y \sim 1$	
$\Gamma_c \leq \Gamma$	$(1 + \kappa)^{1/2}$		$y \sim \Gamma^{1/2} \omega^{-1/2} v^{1/6}$

Table 2.1: Summary of the various scaling regimes for the bipolarness  $y$  of nearly spherical tactoids ( $x \simeq 1$ ) in the presence and absence of an electric field, for large, intermediate and small droplet sizes  $v$ , relative to the crossover volumes  $v_-$  and  $v_+$ . If the electric field is weak and  $0 < \Gamma < \Gamma_c$ , the bipolarness of the droplet has three different regimes. Under a strong field,  $\Gamma > \Gamma_c$  there are two regimes. Expressions for the crossover volumes  $v_-$  and  $v_+$  and the critical field strength  $\Gamma_c$  are listed in table IV. Notice that for  $\Gamma = 0$ ,  $v_+ \rightarrow \infty$  and there are strictly speaking only two regimes.

$v_c = \omega^{-3}(1 + \kappa)^3$ , where we inserted  $\Gamma_c$  in the expression for  $v_+$ . If  $\Gamma > \Gamma_c$ , we find the crossover to occur for  $v_c = \Gamma^{-3/2}(1 + \kappa)^{3/2}$  that can be found by equating Eqs. 2.3 and 2.4.

The summary of the results of this subsection is presented in Table 2.1.

So, in conclusion, if  $\Gamma > \Gamma_c$ , then  $y \gg 1$  decreases with increasing volume  $v$  of the tactoid until larger than the critical value  $v_c$ . If larger than  $v_c$ ,  $y$  increases again with increasing volume and  $y$  does not approach the value of unity, that is, the tactoid does not become bipolar. For  $\Gamma < \Gamma_c$ , the director field is bipolar if  $v_- < v < v_+$ , but not outside of this range of volumes. For  $v < v_-$  the bipolarness  $y$  decreases with increasing volume, whilst for  $v > v_+$  it increases with increasing volume. All in all this demarcates three scaling regimes for the degree of bipolarness of the director field.

As we shall see next, for elongated tactoids the number of regimes increases to five.

### 2.1.2 Elongated tactoids

For elongated tactoids, matters become significantly more complex. To calculate the optimal values for the bipolarness  $y$  and the aspect ratio  $x$  for  $x \gtrsim 1$ , we need to minimize

the free energy Eq. 2.1 with respect to both  $x$  and  $y$ . This gives rise to the following set of coupled equations,

$$y^4 = \omega x^{-2} (y^2 - 1)^2 + v^{-1/3} x^{-5/3} (1 + \kappa x^{-2}) + v^{1/3} \Gamma x^{-7/3}, \quad (2.5)$$

and

$$y^2 = 1 + \omega^{-1} x^{1/3} (1 + \kappa x^{-2}) v^{-1/3} + \Gamma \omega^{-1} v^{1/3} x^{-1/3}. \quad (2.6)$$

Inserting the last two terms of Eq. 2.6 in Eq. 2.5, we find

$$\frac{x^2}{\omega} = (1 - y^{-2}) + (1 - y^{-2})^2. \quad (2.7)$$

Inserting this back in Eq. 2.6 produces a non-linear equation entirely in terms of the quantity  $y$ . Unfortunately, we have not been able to solve this expression exactly. It can of course be solved numerically, but this would obviously defeat the purpose of the scaling theory. Fortunately, the governing equations can be solved asymptotically in a number of useful limiting cases that we will discuss next.

For instance, we have seen in the preceding section that for very large and very small droplet volumes the director-field must be nearly homogeneous, implying that  $y \gg 1$ . We note that large and small here refers to the critical volumes  $v_-$  and  $v_+$ , introduced already in the preceding subsection for nearly spherical tactoids but that now will conform to slightly different expressions given below. Eq. 2.7 tells us that if  $y \rightarrow \infty$ , the director field is uniform, and the aspect ratio is (apart from a multiplicative constant) equal to  $\sqrt{\omega}$ . This

is consistent with the exact result  $x = 2\omega^{1/2}$  obtained by means of the Wulff construction for  $\omega \geq 1$  [29].

Inserting  $x \simeq \omega^{1/2}$  in Eq. 2.5 gives, to leading order for large values of  $y$ ,

$$y^2 \sim v^{-1/3}\omega^{-5/6} \left(1 + \kappa\omega^{-1}\right) + v^{1/3}\omega^{-7/6}\Gamma. \quad (2.8)$$

This means that for sufficiently small droplets

$$y \sim v^{-1/6}\omega^{-5/12} \left(1 + \kappa\omega^{-1}\right)^{1/2}, \quad (2.9)$$

whilst if they large sufficiently large we have

$$y \sim v^{1/6}\omega^{-7/12}\Gamma^{1/2}. \quad (2.10)$$

It is worth mentioning that the result for large droplets does *not* depend on the value of  $\kappa$  that is a measure for the magnitude of the bend elastic constant. Recall that in Eqs. 2.3 and 2.4, we find the same scaling of the bipolarity with the dimensionless volume for nearly spherical droplets. The scaling with the anchoring strength is slightly different, however.

Equation 2.9 applies for  $v \ll v_- = \omega^{-5/2}(1 + \kappa\omega^{-1})^3$  and Eq. 2.10 for  $v \gg v_+ = \Gamma^{-3}\omega^{7/2}$ , as can be deduced from Eq. 2.8. These critical volumes differ slightly from those we calculated for nearly spherical tactoids, as already announced. We conclude that if  $v_- \leq v \leq v_+$  the elongated droplets must be bipolar.

If  $v_+$  drops below  $v_-$ , the tactoids are always more or less uniform, and  $x \simeq \omega^{1/2}$ . This happens at a critical field strength  $\Gamma_c = \omega^2(1 + \kappa\omega^{-1})$  that we find by setting  $v_+ = v_-$ .

The crossover of decreasing to increasing bipolarness with increasing volume now occurs at a critical volume  $v_c = \omega^{-3}$  for  $\Gamma = \Gamma_c$ . If  $\Gamma > \Gamma_c$ , the crossover happens at a critical volume  $v_c = \Gamma^{-3/2}\omega^{1/2}(1 + \kappa\omega^{-1})^{3/2}$ , which we find by equating Eqs. 2.9 and 2.10.

What the aspect ratios of the tactoids are when  $v_- \leq v \leq v_+$ , so when the director field is no longer uniform, can be inferred from Eqs. 2.6 by inserting  $y = 1 + \delta$  in Eq. 2.7 and presuming that  $\delta \ll 1$ . Solving these equations then gives to leading order in  $\delta = x^2\omega^{-1} \ll 1$  an expression for the aspect ratio:  $x^{5/3} \sim v^{-1/3}(1 + \kappa x^{-2}) + v^{1/3}\Gamma x^{-2/3}$ . For small droplets with a volume  $v_+ \gg v > v_-$ , we have  $x \sim v^{-1/5}$  if we ignore the contribution from the bend elasticity; thus the droplet becomes less elongated with increasing volume. For larger ones,  $v_- \ll v < v_+$ , the aspect ratio  $x \sim v^{1/7}\Gamma^{3/7}$  grows again with increasing volume.

As we need to insist that  $x > 1$  for the equations to hold, we take the value of  $x = 1$  as the crossover to the regimes where the droplets are more or less spherical. Inserting this condition in the equation for the aspect ratio gives  $1 \sim v^{-1/3}(1 + \kappa) + v^{1/3}\Gamma$ , which we translate in two crossover volumes. In the absence of a field, the crossover from an elongated droplet with  $x = \omega^{1/2}$  to a nearly spherical droplet with  $x = 1$  occurs for  $v = v_<$  with  $v_< \equiv (1 + \kappa)^3 > v_-$  another crossover volume. For sufficiently weak fields, they start to elongate again if  $v_> < v < v_+ = \Gamma^{-3}\omega^{7/2}$  with the crossover volume  $v_> \equiv \Gamma^{-3}$  smaller than  $v_+$  since we presume that  $\omega > 1$ . For  $v > v_+$  the director field is uniform and the aspect ratio obeys again  $x \sim \omega^{1/2}$ .

The picture that emerges is one where for  $v < v_-$  the nematic droplets have a more or less uniform director field with an aspect ratio of about  $\omega^{1/2}$ , and the same for  $v > v_+$ . If  $v > v_-$ , the droplets become increasingly bipolar and the aspect ratio decreases

with increasing volume. If the scaled volume  $v$  increases further to get closer to  $v_+$ , the bipolar character of the director field diminishes again with increasing volume, while the aspect ratio increases to its maximum value of about  $\omega^{1/2}$ , see Fig. 2.1. Notice that we have presumed that  $\omega \gg 1$ ; otherwise, we would not have  $x \gg 1$ .

Somewhere in the size range  $v_- \leq v \leq v_+$ , the droplets actually become nearly spherical, in which case the theory of the preceding section applies. This happens in the range of volumes for which  $v_< < v < v_>$ . The nearly spherical drop regime disappears if  $v_< = v_>$ . Equating these critical volume shows that this occurs for field strengths  $\Gamma$  larger than the critical value of  $\Gamma_* \equiv (1 + \kappa)^{-1}$ . In that case we only have crossover from decreasing elongated to increasing elongated at a crossover volume  $v_* = \Gamma^{-5/4}$ . Since  $\Gamma_* < \Gamma_c$ , we conclude that for  $\omega \gg 1$  we lose the spherical tactoid regime before we lose the bipolar director field.

The summary of these results are presented in Tables 2.2, 2.3, and 2.4, as well as in Fig. 2.2, showing the different regimes and crossovers. The conclusion of our scaling theory is that the aspect ratio of the nematic droplets is at most  $\omega^{1/2}$ , independent of the volume or the field strength. In other words, external fields cannot elongate a tactoid to aspect ratios beyond those that are found in the absence of a field, at least for the family of director fields that we presume. We return to this issue in the Discussion section below.

In the next section, we present the numerical evaluation of our variational theory and obtain the mathematically exact response of the director field and the shape of the droplet in the presence of an electric field, and compare these with the scaling theory. As

we shall see, our scaling predictions are robust. This means also that the conclusions that we base them on are robust.

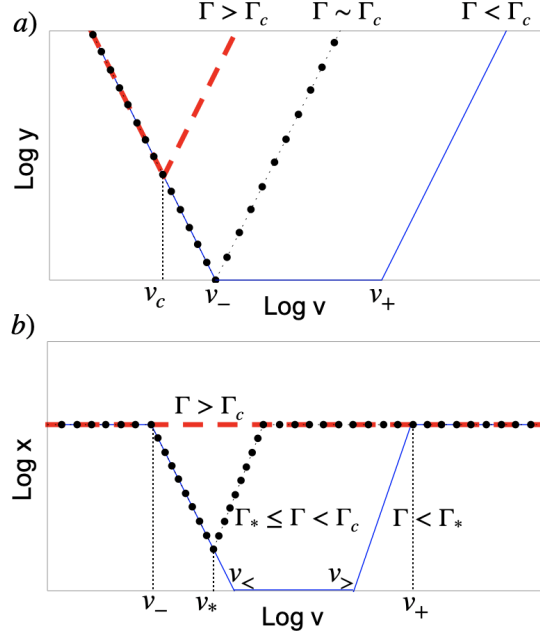


Figure 2.1: Dependence of (a) the degree of bipolarity  $y$  and (b) the aspect ratio  $x$  of tactoids on the scaled volume  $v$  in the presence of an electric field, according to the scaling theory. Blue solid line: the field strength  $\Gamma$  is below the critical value  $\Gamma_c$ , and the anchoring strength  $\omega$  is somewhat larger than unity. The volumes  $v_-$  and  $v_+$  demarcate crossovers from quasi bipolar director fields to bipolar ones, and  $v_<$  and  $v_>$  those from elongated to spherical droplet shapes. Dash-dotted line: same curve, but now for  $\Gamma = \Gamma_c$ . Dashed lines:  $\Gamma > \Gamma_c$ . For fields above the critical field strength  $\Gamma_*$ , the tactoids are always elongated provided the anchoring strength  $\omega$  is sufficiently large. See the main text. The slopes of the various curves are listed in Tables I, II and III, and the values of the various crossover volumes and field strengths in Table IV.

	$v < v_-$	$v_- < v < v_+$	$v_+ < v$
$\Gamma \leq \Gamma_c$	$y \sim \omega^{-5/12} v^{-1/6}$	$y \sim 1$	
$\Gamma_c \leq \Gamma$	$(1 + \kappa\omega^{-1})^{1/2}$		$y \sim \Gamma^{1/2} \omega^{-7/12} v^{1/6}$

Table 2.2: This table summarises the various scaling regimes for the bipolariness  $y$  of elongated tactoids ( $x \gg 1$ ) in the presence and absence of an electric field, for large, intermediate and small droplet sizes  $v$ , relative to the crossover volumes  $v_-$  and  $v_+$ . If the electric field is weak and  $0 < \Gamma < \Gamma_c$ , the bipolariness of the droplet has three different regimes. Under a strong field,  $\Gamma > \Gamma_c$  there are two regimes. Expressions for the crossover volumes  $v_-$  and  $v_+$  and the critical field strength  $\Gamma_c$  are listed in table IV. Notice that for  $\Gamma = 0$ ,  $v_+ \rightarrow \infty$  and there are strictly speaking only two regimes.

	$v < v_-$	$v_- < v < v_<$	$v_< < v < v_>$	$v_> < v < v_+$	$v_+ < v$
$\Gamma < \Gamma_*$			$x \sim 1$		
$\Gamma_* < \Gamma < \Gamma_c$		$x \sim v^{-1/5}$		$x \sim \Gamma^{3/7} v^{1/7}$	
$\Gamma_c < \Gamma$			$x \sim \sqrt{\omega}$		

Table 2.3: This table summarises the various scaling regimes for the aspect ratio  $x$  of tactoids in the presence and absence of an electric field, for large, intermediate and small droplet sizes  $v$ , relative to the crossover volumes  $v_-$  and  $v_+$ , and  $v_<$  and  $v_>$ . For simplicity, we have dropped any dependence of the aspect ratio on  $\kappa$ . Expressions for the crossover volumes  $v_-$ ,  $v_+$ ,  $v_<$  and  $v_>$ , and the critical field strengths  $\Gamma_c$  and  $\Gamma_*$ , are listed in table IV. Notice that for  $\Gamma = 0$ ,  $v_+ \rightarrow \infty$  and  $v_> \rightarrow \infty$ .

	$\omega \lesssim 1$	$\omega \gtrsim 1$
$v_-$	$\omega^{-3} (1 + \kappa)^3$	$\omega^{-5/2} (1 + \kappa\omega^{-1})^3$
$v_+$	$\omega^3 \Gamma^{-3}$	$\omega^{7/2} \Gamma^{-3}$
$v_c$	$\Gamma^{-3/2} (1 + \kappa)^{3/2}$	$\Gamma^{-3/2} \omega^{-1} (1 + \kappa\omega^{-1})^{3/2}$
$v_<$	—	$(1 + \kappa)^3$
$v_>$	—	$\Gamma^{-3}$
$v_*$	—	$\Gamma^{-5/4}$
$\Gamma_*$	—	$(1 + \kappa)^{-1}$
$\Gamma_c$	$\omega^2 (1 + \kappa)^{-1}$	$\omega^2 (1 + \omega^{-1} \kappa)^{-1}$

Table 2.4: Listing of all crossover volumes  $v$  and critical field strengths  $\Gamma$ , for small and large values of the anchoring strength  $\omega$ . Crossovers from elongated to spherical tactoids only occur if  $\omega$  is sufficiently large.

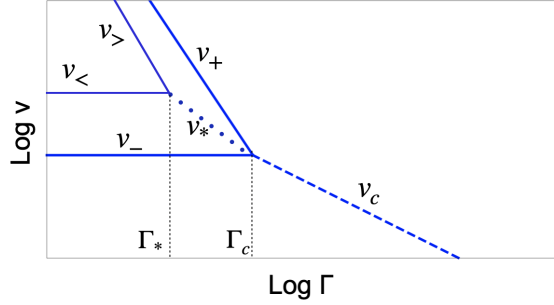


Figure 2.2: Schematic “phase” diagram of director fields of tactoids in an external field. Plotted is the scaled volume  $v$  versus the scaled field strength  $\Gamma$ . Indicated are the crossovers between the five regimes, demarcated by the crossover volumes  $v_-$ ,  $v_+$ ,  $v_-$ ,  $v_+$ ,  $v_*$  and  $v_c$ . Expressions for the crossover volumes  $v_-$ ,  $v_+$ ,  $v_-$  and  $v_+$ , and the critical field strengths  $\Gamma_c$  and  $\Gamma_*$ , are listed in table IV. See also the main text. In the region bounded by  $v_-$  and  $v_c$ , tactoids with sufficiently large anchoring strength  $\omega \gg 1$  are elongated with a director field that is quasi bipolar with a bipolarness  $y$  that decreases with increasing volume. In the region bounded by  $v_c$  and  $v_+$  in the upper right-hand corner it is quasi bipolar with a bipolarness that increases with droplet volume. In region bounded by  $v_-$  and  $v_+$  in the upper left-hand corner the director field is for all intents and purposes bipolar. The tactoids are more or less spherical in the region bounded by  $v_-$  and  $v_+$  in the upper most left-hand corner, and elongated outside of that region, at least if  $\omega \gg 1$ . The volume  $v_c$  demarcates the crossover from decreasing to increasing bipolarness for quasi bipolar director fields, the volume  $v_*$  that between decreasing aspect ratio to increasing aspect ratio.

## 2.2 Numerical Results

The scaling theory of the preceding section has enabled us to identify different scaling regimes, which we now investigate by numerically minimizing the free energy Eq. 1.5. To this end, we evaluate Eq. 1.5 for opening angles  $0 \leq \alpha \leq \pi$  and degrees of bipolarity of the director field  $1 \leq y \leq \infty$  and find the values of these quantities for which the free energy  $f$  is minimal. So, for a given scaled volume  $v$ , anchoring strength  $\omega$ , ratio of bend-to-splay elastic constants  $\kappa$  and electric field strength  $\Gamma$ , we obtain the optimal values of both  $\alpha$  and  $y$ . We recall that the aspect ratio of the tactoids  $x$  is directly linked to the opening angle via the relation  $x = \cot(\alpha/2)$ . In order to find the minimum free energy, we numerically calculate all integrals given in Sect. II.

It is clear that the electric field drives the director field to align itself with it, implying that the major axis of a tactoid orients parallel to the electric field. This happens irrespective of whether the director-field configuration is uniform or bipolar. If the electric field is sufficiently weak, the director-field is not perturbed by the electric field. If the field is sufficiently strong, we would expect the director field of the droplet to become homogeneous, even if the director field in the absence of a field is bipolar. What weak and strong here mean depends on volume of a tactoid as we have seen in the preceding section, and is schematically summarized in the Figs. 2.1 and 2.2.

Figure 2.3 confirms this expectation. Shown is the bipolarity  $y$  as a function of the dimensionless volume  $v$  of the tactoids, for the case where we (arbitrarily) set for the dimensionless bend constant  $\kappa = 10$  and for the anchoring strength  $\omega = 14$ . Indicated are results for different values of the dimensionless electric field  $\Gamma$ . We confirm the scaling

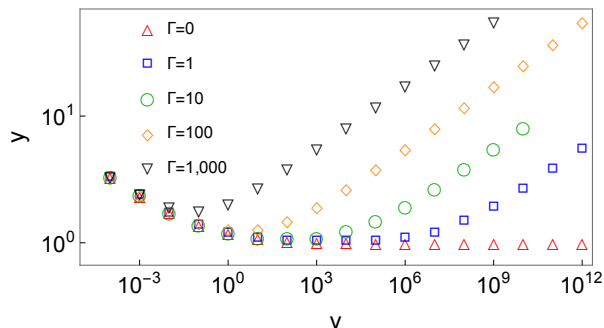


Figure 2.3: The bipolarity  $y$  of the director field of a tactoid in the presence of an electric field as a function of its dimensionless volume  $v$ . Indicated by the different symbols are results for different values of the dimensionless electric field strength  $\Gamma$ . The dimensionless anchoring strength is fixed at  $\omega = 14$  and the dimensionless bend constant at  $\kappa = 10$ .

prediction that two critical volumes emerge, one associated with the crossover from a quasi bipolar to a bipolar director field,  $v_-$ , and one with the crossover from a bipolar to quasi bipolar director field,  $v_+$ . For  $\Gamma \geq 100$ , we only find quasi bipolar director fields characterized by a bipolarity  $y > 1$  for all volumes  $v$ . The scaling exponent  $\beta$  we find for  $y \sim v^\beta$  equals  $\beta = -0.15$  for small volumes and  $\beta = +0.16$  for large volumes, values that agree reasonably well with the predicted exponents of  $-1/6$  and  $+1/6$  that we obtained from the scaling theory and are quoted in table 2.2.

Figure 2.3 also shows that the bipolarity  $y$  increases with the electric field strength  $\Gamma$ , if the volume of a tactoid is sufficiently large,  $v > v_+$ . According to the scaling prediction Eq. 2.10,  $y$  should scale as  $\Gamma^{1/2}$ . Figure 2.4, in which we plotted the bipolarity as a function of the field strength for the case where  $\omega = 14$  and  $\kappa = 10$ , confirms that the scaling exponent is 0.5 over three decades of  $\Gamma$ . So, indeed, increasing the field strength leads to director fields that become increasingly homogeneous, as one would in fact expect from the scaling theory of the previous section. See also Table 2.2.

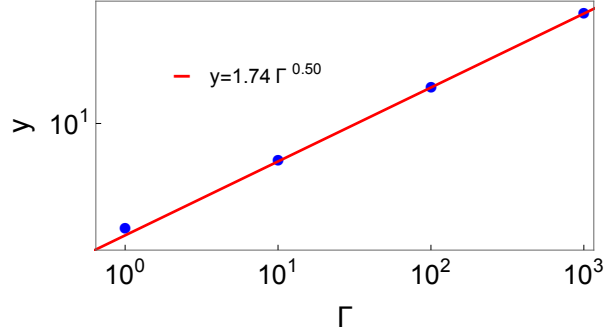


Figure 2.4: Bipolarity  $y$  of a tactoids as a function of the dimensionless electric field  $\Gamma$  for a dimensionless volume  $v = 10^7$ . Anchoring strength  $\omega = 14$  and dimensionless bend constant  $\kappa = 10$ . The solid line shows the scaling of  $y$  as with  $\Gamma^{0.5}$ .

According to the scaling theory of the preceding section, the impact of the (scaled) bend elastic constant  $\kappa$  on the bipolarity  $y$  of a tactoid is negligible for sufficiently large tactoids in the presence of an external field. See Table II. It is negligible for small tactoids too, but only provided  $\kappa \ll \omega$ . Our numerical results presented in Fig. 2.5 confirms for the case  $\omega = 14$ , the bipolarity is an invariant of  $\kappa$  for sufficiently large volumes, but becomes a function of  $\kappa$  for values larger than about 10, as expected from the scaling theory.

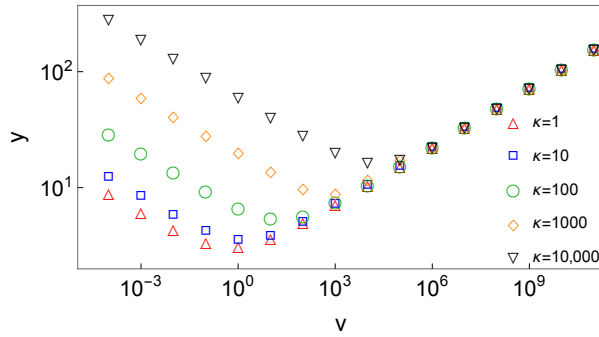


Figure 2.5: Bipolarity  $y$  of the droplet as a function of the dimensionless volume  $v$  of tactoids in the presence of an electric field for different values of the dimensionless bend constants  $\kappa$  indicated by the symbols. Anchoring strength  $\omega = 14$  and dimensionless field strength  $\Gamma = 100$ .

For bend elastic constants  $\kappa > 10 \approx \omega$ , the bipolarness should exhibit a power-law scaling predicted by the scaling relation Eq. 2.9 that then takes the simpler form  $y \sim v^{-1/6} \omega^{-11/12} \kappa^{1/2}$ . In Fig. 2.6 we have plotted the bipolarness  $y$  as a function of  $\kappa$  for  $\Gamma = 100$  and  $v = 10^{-4}$ . The exponent that we measure is 0.49, which is indeed close to the value obtained from the scaling theory.

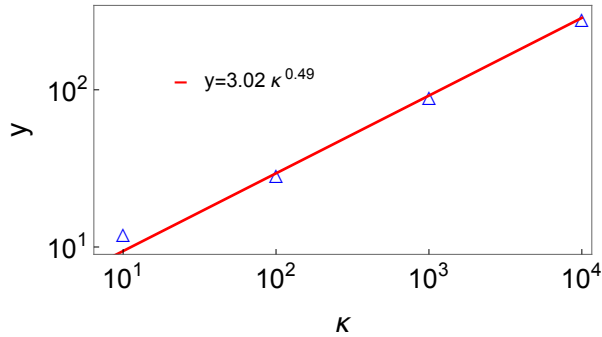


Figure 2.6: Bipolarness of a tactoid as a function of the dimensionless bend constant  $\kappa$  in the presence of an electric field. Anchoring strength  $\omega = 1.4$ , dimensionless field strength  $\Gamma = 100$  and dimensionless volume  $v = 10^{-4}$ .

Our scaling theory also predicts the bipolarness of the tactoids to depend on the anchoring strength,  $\omega$ . Indeed, Eqs. 2.3 and 2.4 for nearly spherical tactoids, and Eqs. 2.9 and 2.10 for elongated ones, predict that both for small and large droplets the bipolarness should shift with shifting anchoring strength. This makes intuitive sense, because the larger the anchoring strength is, the larger the free energy penalty becomes for imperfect planar anchoring. Hence, with increasing anchoring strength the tactoids should become increasingly bipolar. This is what our numerical calculations also confirm, as is shown in Fig. 2.7. On a logarithmic scale the curves shift vertically by an amount that depends on the anchoring strength  $\omega$ .

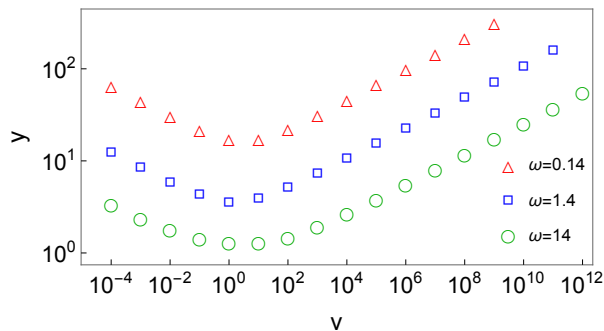


Figure 2.7: Bipolarity  $y$  of a tactoid as a function of the dimensionless volume  $v$  in the presence of an electric field for different values of the anchoring strength, indicated by the symbols. Dimensionless field strength  $\Gamma = 100$  and bend constant  $\kappa = 10$ .

The scaling of the bipolarity  $y$  with the anchoring strength  $\omega$  is highly non-trivial, as is implicit in the scaling predictions Eqs. 2.3 and 2.4 for nearly spherical tactoids, and Eqs. 2.9 and 2.10 for elongated ones. It depends not only on the shape of the tactoids, but also whether the tactoids are large or small, and on whether or not the bend elastic constant is large. To account for this, we plot in Figs. 2.8 and 2.9 the bipolarity  $y$  as a function of the anchoring strength  $\omega$  for two droplet sizes and fixed values of  $\Gamma = 10$  and  $\kappa = 0$ . The appropriate scaling regimes for  $\omega < 1$  for which the droplets are approximately spherical, and  $\omega > 1$  for which they are elongated, are also illustrated in the figure. Four different scaling exponents, which agree rather well with the predictions from scaling theory are shown in the figure.

How the value of the bend elastic constant  $\kappa$  impacts the dependence of the bipolarity  $y$  and the anchoring strength  $\omega$  is highlighted in Fig. 2.10 for a large and small value of  $\kappa$ . For the range of anchoring strengths shown, a small tactoid volume of  $v = 10^{-4}$  and a field strength of  $\Gamma = 10^2$ , we find scaling exponents of  $-0.43$  and  $-0.90$  for the small and

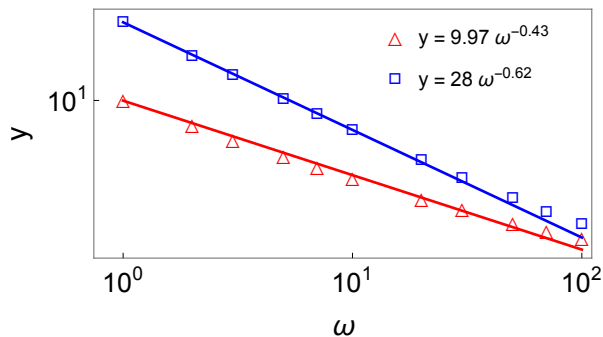


Figure 2.8: Bipolarity  $y$  of a tactoid as a function of an anchoring strength  $\omega > 1$  for small and large droplets, with dimensionless volumes  $v = 10^{-2}$  and  $v = 10^6$ . The dimensionless electric field strength is fixed at  $\Gamma = 10$  and the dimensionless bend constant at  $\kappa = 0$ . Indicated are also the scaling relations  $y \sim \omega^{-0.43}$  for the small volume and  $y \sim \omega^{-0.62}$  for the large volume. See also the main text.

large values of dimensionless bend constants  $\kappa$ , which have to be compared with the scaling predictions of  $-5/12 \simeq -0.42$  and  $-11/12 \simeq -0.92$ . Again, we find quite good agreement between our numerical work and the scaling theory. (See also table II.)

Having exhaustively verified the theoretical scaling predictions for the degree of bipolarity of the tactoids, we now proceed to investigate how their aspect ratio depends on the volume and how it responds to the presence of an electric field. It is well known that, in the absence of an electric field, the aspect ratio of a nematic tactoid decreases with increasing droplet size. This happens to be so not only in bulk, but also if the tactoids deposited on a partially wetting surface [6, 13, 40]. Indeed, from the scaling theory we expect that for  $v > v_-$ , the aspect ratio  $x$  should scale as  $v^{-1/5}$  at least if  $\kappa \ll \omega$  and  $\omega \rightarrow \infty$  [13, 29, 30]. For finite  $\omega = 14$  the decay of the aspect ratio with volume is even a weaker function of the volume, as Fig. 2.11 shows for the field-free case  $\Gamma = 0$ .

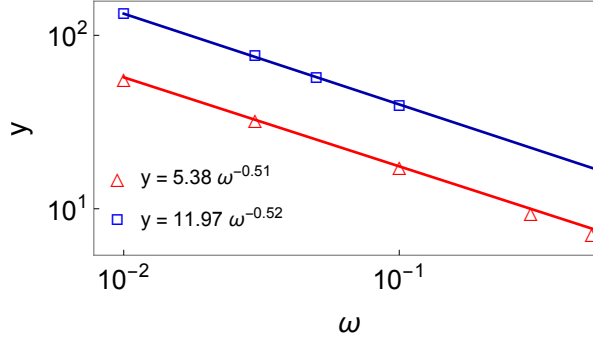


Figure 2.9: Bipolarity  $y$  of a tactoid as a function of anchoring strength ( $\omega < 1$ ) for small and large droplets, with dimensionless volumes  $v = 10^{-2}$  and  $v = 10^6$ . The dimensionless electric field strength is fixed at  $\Gamma = 10$  and the dimensionless bend constant at  $\kappa = 0$ . Indicated are also the scaling relations  $y \sim \omega^{-0.51}$  and  $y \sim \omega^{-0.52}$ . See also the main text.

Notice that for the dimensionless bend constant of  $\kappa = 10$ , the predicted critical magnetic field strength of  $\Gamma_* = 1/11 \simeq 0.09$  coincides with the smallest non-zero value of  $\Gamma$  taken in our numerical calculations. This means that our results of Fig. 2.11 should show conditions characterised by an absence of an intermediate regime with spherical tactoids, excluding the case  $\Gamma = 0$ . See also the phase diagram of Fig. 2.2. The predicted crossover volume  $v_* \sim \Gamma^{-5/4}$  from a decreasing aspect ratio to an increasing aspect ratio varies 5 orders of magnitude for the range of field strengths shown in the figure, in agreement with our numerical results presented in the figure.

What Fig. 2.11 also shows is that for increasingly large fields, the drop in aspect ratio becomes small mirroring the prediction of our scaling theory. This happens for  $\Gamma > \Gamma_c \sim \omega^2/(1 + \kappa/\omega) \simeq 100$  for our choice of parameters, when the drop in aspect ratio in fact disappears. This value is consistent with our numerical findings. In that case the director field is for all intents and purposes uniform irrespective of the volume of the nematic droplet. This means that in our model, there is an upper limit for the aspect ratio, namely  $2\sqrt{\omega}$ .

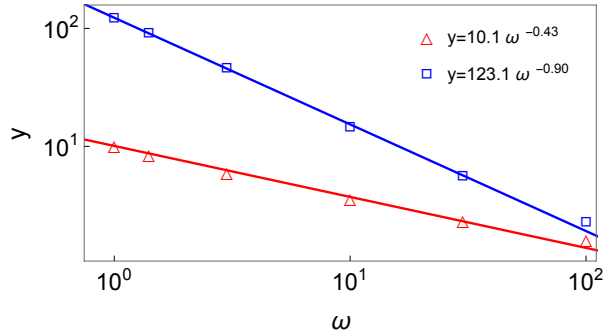


Figure 2.10: Bipolariness  $y$  as a function of anchoring strength  $\omega$  for two different dimensionless bend constants of  $\kappa = 0.1$  and  $\kappa = 10^3$ . The dimensionless volume is set at a value  $v = 10^{-4}$ . Also indicated are the scaling exponent of  $-0.43$  for the small value of the bend constant and of  $-0.90$  for the large value of the constant. See also the main text.

All of this implies that for our choice of director field geometry, an externally applied electric (or magnetic) field *cannot* elongate tactoids beyond their maximum aspect ratio that under the field-free conditions happens for sufficiently small droplets. This, clearly, goes against the grain of the experimental observations of Metselaar *et al.* of tactoids in electric fields [40], and those of Kaznacheev and collaborators in magnetic fields [27]. As we argue in the next section, this must mean that either (i) the director field does not conform to a bispherical geometry in an external alignment field; (ii) the tactoids are in a restricted equilibrium characterized by a bipolariness that is fixed to the value of the field-free initial state; or (iii) the various elastic and surface constants do depend on the strength of the field.

In this paper, we present a model in which the director field and shape of a nematic tactoid can adjust themselves both in order to optimize the interfacial, elastic and Coulomb energy in the presence of an externally applied orienting field. We restrict the shape of the tactoid to that of the family of circle sections of revolution, and the director field to that of

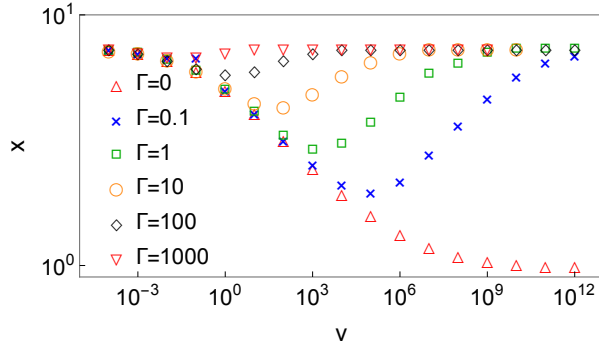


Figure 2.11: The aspect ratio  $x$  of a tactoid as a function of the dimensionless volume  $v$  for different (dimensionless) electric field strengths  $\Gamma$  indicated by the symbols. The anchoring strength is set at  $\omega = 14$  and the dimensionless bend constant at  $\kappa = 10$ .

the family of fields that can be described by bispherical geometries [60, 61]. We find that the known “phase” diagram of nematic tactoids becomes more complex in the presence of an electric field. [29, 30, 31]

In the absence of such an alignment field there are three regimes, separating elongated tactoids with a uniform director field if they are sufficiently small from roundish bipolar ones if very large, with an intermediate size range where the drops are quasi bipolar and somewhat elongated. In the presence of an alignment field, we have identified up to five regimes depending on the strength of the anchoring of the director to the interface. A schematic of the new phase diagram is given in Fig. 2.2.

Close comparison of theoretical predictions based on this model and experimental observations on tactoids of carbon nanotubes in chlorosulfonic acid by Jamali *et al.* have shown that, in the absence of an electric orienting field, there is a very good agreement between the theory and experiments [6]. The predicted gradual crossover from elongated to more or less spherical shapes, and from uniform to bipolar director fields, is confirmed

experimentally, not only for tactoids in bulk solution but also for sessile tactoids, *i.e.*, tactoids on surfaces [13]. Curve fits provide access to information on the surface energies and bend constants [6, 13, 28, 30, 62, 63, 63, 64, 65, 66].

For instance, if we curve fit the theory to the experimental data of Metselaar *et al.* on tactoids formed in dispersions of chitin fibres in water in the absence of an electric field, we obtain a reasonably good agreement if we set  $\omega = 1.6$ ,  $\kappa = 20$  and  $(K_{11} - K_{24})/\sigma = 4 \mu\text{m}$ . See Fig. 2.12, where the aspect ratio  $x$  is plotted against the actual volume of the droplets. Also shown in the figure is the predicted bipolarity  $y$  of the tactoids, which vary between 3 and just over 1 over that range of droplet volumes. It suggests that the tactoids of chitin in water are either bipolar or quasi bipolar, in agreement with experimental observation. [40]

Because of the scatter in the data, and since we do not cover the whole range of volumes from nearly uniform to bipolar director fields as was done in the work of Jamali *et al.* [6], we cannot expect these estimates to be highly accurate. Still, if we take them at face value, we find them to differ quite substantially from the ones found by Jamali *et al.* for carbon nanotubes in chlorosulfonic acid, with  $\omega = 5.6$ ,  $\kappa = 1.3$  and  $(K_{11} - K_{24})/\sigma = 78 \mu\text{m}$  [6]. This, however, should not be too surprising, given that both the elastic constants and surface energies depend sensitively on the dimensions of the particles [36, 54, 56].

Rather unexpectedly, our predictions fail if an external field is applied. In the experiments of Metselaar *et al.*, sufficiently large tactoids elongate up to ten times their original aspect ratio, which is much more elongated than the droplets in the absence of a field [40]. As we have seen in our model calculations, the presence of very large field

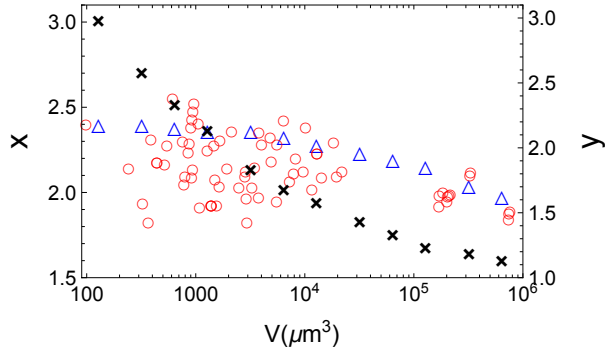


Figure 2.12: Aspect ratio  $x$  and bipolarity  $y$  of the director-field as a function of volume of a droplet in the absence of the electric field with  $\Gamma = 0$ . Left vertical axis shows us the aspect ratio (we use blue triangles for the aspect ratio) and the right vertical axis shows us bipolarity (cross signs for bipolarity) and the red circles represent the experimental data of [40]. The best fit we obtain by eye are for the parameter values  $\kappa = 20$ ,  $\omega = 1.3$  and  $(K_{11} - K_{24})/\sigma = 4 \mu\text{m}$ . Notice that the largest tactoids are bipolar because  $y \rightarrow 1$  and the smallest ones quasi bipolar with  $y \approx 3$ .

strengths do *not* lead to highly elongated shapes but to uniform director fields. As already announced, this might perhaps suggest that the bipolarity of the tactoids cannot respond sufficiently swiftly to the switching on of the external field. Before discussing the accuracy of this presumption, we first investigate its consequences assuming that it is true.

The procedure that we pursue is as follows. First we calculate the bipolarity  $y$  of the director field for the field-free case with  $\Gamma = 0$ . Next, in the presence of an orienting field, so for  $\Gamma > 0$ , we use this value of the bipolarity and optimise the free energy only with respect to the aspect ratio  $x$ . Following this procedure, we do find a strong elongation of the droplets as Fig. 2.13 shown, where we compare the prediction of the full-equilibrium and this *restricted-equilibrium* model with the dynamical data of Metselaar *et al.* for tactoids of chitin in water. Shown is the aspect ratio of the droplets as a function of their volumes for a single electric field strength. For the largest droplets, the full relaxation takes more than

the maximum of 1100 seconds, so the tactoids have not fully equilibrated yet, see Fig. 2.13 of [40].

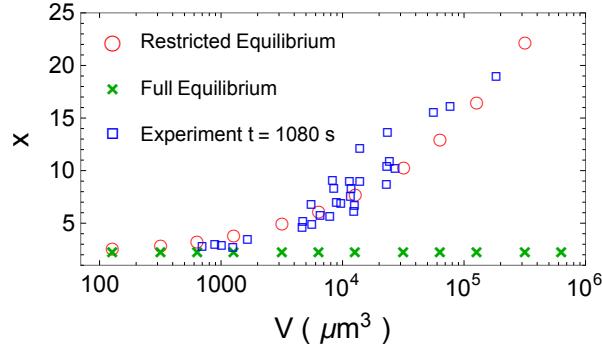


Figure 2.13: Aspect ratio  $x$  of tactoids as a function of volume  $V$  in the presence of an electric field. We compare our numerical results with the experimental data of [40]. The best fit by eye we obtain taking as parameter values  $\Gamma = 500$ ,  $\omega = 1.3$ ,  $\kappa = 20$  and  $(K_{11} - K_{24})/\sigma = 4 \mu\text{m}$ .

It seems that within a restricted-equilibrium calculation, agreement with the experimental data is indeed rather good, even if they do not yet represent fully relaxed tactoids. The data confirm our expectation that the electric field only has an impact on the shape of the tactoids if they are sufficiently large. How large, depends on the strength of the electric field. This is shown in Fig. 2.14, where we show predictions of our restricted-equilibrium model for the aspect ratio  $x$  of nematic droplets as a function of the dimensionless volume  $v$  for different dimensionless field strengths  $\Gamma$ . According to the scaling theory of section III, we should expect an  $x \sim \Gamma^{3/7} v^{1/7}$  for a fully bipolar director field corresponding to sufficiently large droplets. The slopes of the various curves shown in Fig. 2.14 agree with this. Figure 2.15 shows that the scaling with the electric field strength  $\Gamma$  for different tactoid volumes  $v$  also agrees with the scaling prediction of  $3/7 \approx 0.43$ .

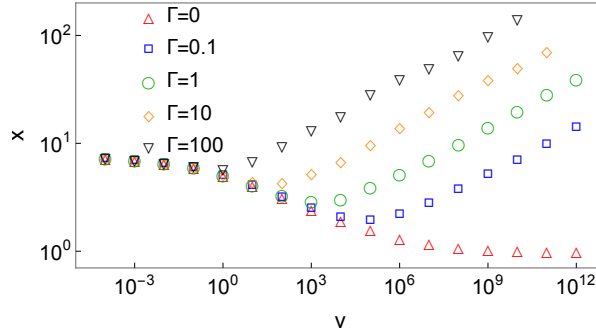


Figure 2.14: Aspect ratio  $x$  of a tactoid as a function of the dimensionless volume  $v$  for different electric field strengths  $\Gamma$  according to the restricted equilibrium model. See the main text. Anchoring strength  $\omega = 14$  and bend elastic constant  $\kappa = 10$ .

All of this of course begs the question why our full equilibrium model, in which the tactoids choose their optimal aspect ratio and director field in response to the external field, does not agree with the experimental observations. Above we have presumed that the bipolarity of the tactoids cannot respond swiftly to the switching on of an electric field, at least less swiftly than the aspect ratio can respond. In that case a restricted equilibrium picture applies, which would be valid for intermediate times. This implies that after an initial increase in aspect ratio, this aspect ratio should decrease again for (potentially) much later times. This has not yet been investigated but would be an interesting avenue of future experimental research.

Whilst this may seem a somewhat far-fetched explanation to align theory and experiment, it does tie in with the observations of Jamali *et al.*, who collected data on hundreds of tactoids of carbon nanotubes in chlorosulfonic acid [6]. Even after 15 days of equilibration, the scatter in the observed aspect ratio remains appreciable and cannot be explained by thermal fluctuations. Indeed, the experiments of Metselaar *et al.* also point at long relaxation times: the largest droplets do not seem completely equilibrated even after

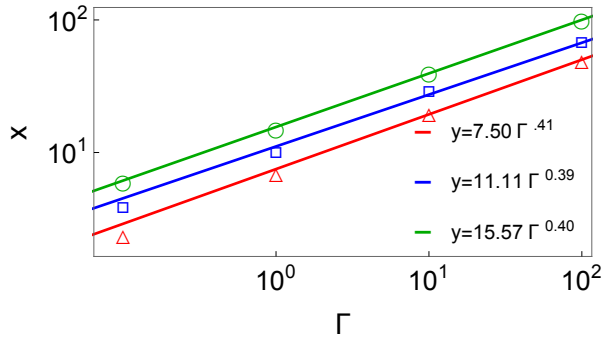


Figure 2.15: Aspect ratio  $x$  of a tactoid as a function of the electric field  $\Gamma$  according to the restricted equilibrium model. Anchoring strength  $\omega = 14$  and dimensionless bend constant  $\kappa = 10$ . Different symbols show different volumes: triangles  $v = 10^7$ , squares  $v = 10^8$  and circles  $v = 10^9$ . Indicated are also the scaling exponents, which are close to 0.4 for the three tactoid volumes.

7000 seconds. On the other hand, the Lattice Boltzmann simulations presented in the work of Metselaar *et al.* [40], which do mirror the large elongation of the tactoids in an external field, point at a relatively swift relaxation of the director field after the external field is switched on.

In the simulations, the director field seems to keep the almost perfect planar alignment to the interface of the tactoid with the surrounding isotropic fluid, while in the bulk of the tactoid the director field seems to become homogeneous [41]. This suggests a different kind of relaxation of the director field in response to the alignment field than the one we presumed in our work, which conserves the geometry of director field. This kind of director field is in our view surprising, as it involves a strong deformation with a small radius of curvature that is very costly in elastic free energy. This is why, generally, it is believed that wall defects in nematics spread out very quickly [35]. (See, however, Tromp *et al.* [67].) We emphasize that in general, the interplay of the defective points (disclinations)

and curvature is not trivial. The complexity arises from solving the elasticity equations in 3D in the presence of defects [68, 69].

In fact, a simple scaling theory supports this view in the context of tactoids. Let us for simplicity take a spherical tactoid of radius  $R$ . A locally deformed director field that preserves perfect planar anchoring would give a free energy of the form  $F \simeq \sigma R^2 + KR^2\xi^{-1} + \gamma R^2\xi$ . Here,  $K$  is some combination of the bend and splay elastic constants,  $\xi \leq R$  is the width of the deformed director field that we equate to its radius of curvature, and  $\gamma = \epsilon_a E^2$  is the Coulomb energy per unit volume. If we optimize  $\xi$ , we get  $\xi = K_{11}^{1/2} \gamma^{-1/2} \leq R$  for  $\gamma \geq K_{11} R^{-2}$ . For  $\gamma \leq KR^{-2}$ , we have  $\xi = R$ .

Hence, we obtain  $F \simeq \sigma R^2 + KR + \gamma R^3$  for  $\gamma \leq KR^{-2}$  and  $F \simeq \sigma R^2 + \gamma^{1/2} + K^{1/2} R^2$  for  $\gamma \geq KR^{-2}$ . For a smooth director field in the limit of large field strengths, we have  $F \simeq \sigma R^2 + \sigma \omega R^2$  because the director field is then approximately uniform. This shows that for  $\gamma \geq \omega \sigma / R$  the uniform director field has a lower free energy than the locally deformed one. Of course, we cannot exclude the possibility that for  $KR^{-2} < \gamma < \omega \sigma / R$  a locally deformed director field wins out albeit that this might also be accompanied by an imperfect anchoring.

In conclusion, we should perhaps not exclude the possibility that the lattice Boltzmann simulations, which are coarse-grained and characterized by rather large interfacial widths even on the scale of the width of the droplets, allow for larger deformations in the interfacial region than a continuum theory would. Because of this, we feel that additional and more comprehensive simulation studies would be useful to perform in order to settle this issue [70].

Finally, we cannot exclude the possibility that the external field has a sizeable impact on both the interfacial tension, the anchoring and on the elastic constants, because they all depend on the degree of orientation order of the particles [36, 48, 49]. Indeed, all of them depend on the degree of alignment of the particles, where we note that the isotropic phase becomes paranematic in the presence of an external field [52, 71, 72]. This implies that the interfacial tension between the nematic droplets and the host phase should decrease with increasing field strength. In fact, it should disappear altogether at some critical field strength. The study presented in this paper shows that these issues can only be resolved with more detailed experimental investigation of the impact of external fields on the properties of isotropic and nematic phases of rod-like colloidal particles.

## Chapter 3

# Dynamics of elongation of nematic tactoids in an electric field

### 3.1 Introduction

Experimental findings on the structure and shape of tactoids seem to be reasonably well described by macroscopic theory, even if they are not very large on the scale of the length of the colloidal particles. Indeed, the application of macroscopic theory makes possible the extraction of information on the elastic constants of the nematic and interfacial free energies between the co-existing isotropic and nematic phases from polarization microscopic images alone if the experimental data include a sufficiently wide range of tactoid sizes [6, 17, 28, 29, 30, 31, 40, 73]. Interestingly, the experiments on the aspect ratio (or length and breadth) as a function of the volume of tactoids typically exhibit a significant amount of scattered data. Puech *et al.* [12] argued that this must be due to thermal fluctuations on account

of the fact that the interfacial free energies of lyotropic nematics must be very low. It so happens that for this type of colloidal system interfacial tensions can be of the order of  $\mu\text{N m}^{-1}$  or even significantly below that [12, 36, 74, 75]. Incidentally, this also explains why tactoids require very little energy to significantly deform, and why the shape and structure of tactoids are so strongly affected by the contact with an adsorbing surface or the presence of an externally applied electric, magnetic or flow field [13, 28, 40, 76].

It is also clear from the work of Jamali *et al.* on nematic tactoids found in dispersions of carbon nanotubes in a superacid, however, that this variation can neither be explained in terms of the magnitude of thermal (equilibrium) fluctuations predicted by macroscopic theory nor by potential errors in the measurement of the aspect ratio of tactoids [6]. This already suggests that the equilibration of the shape and director field of tactoids might be quite slow [77]. In fact, recent work by Mezzenga and collaborators on tactoids in aqueous dispersions of amyloids and of cellulose nanocrystals supports this: tactoids produced via nucleation and growth may have a different aspect ratio and internal structure than those produced in a microfluidic device [78]. This explains to some extent why experiments on tactoids in aqueous dispersions of chitin in the presence of an applied AC electric field [40] show a large disconnect with predictions from equilibrium theory and the results from Monte Carlo simulations [70, 73]. Experimentally, tactoids are able to elongate by a factor of up to about ten through their coupling to the electric field. In contrast, in equilibrium theory and Monte Carlo simulations it is the director field that responds to the external orienting field with the aspect ratio of the tactoids showing much less sensitivity, see also Figure 3.1.

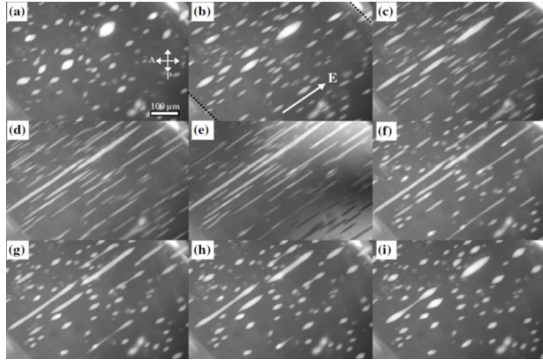


Figure 3.1: Polarization microscopic images of the evolution in time of tactoids in an aqueous solution of chitin fibers, following the switching on and off of an AC electric field of root-mean-square magnitude of  $E = 160 \text{ V mm}^{-1}$  and a frequency of 300 kHz. (a) to (e): The field is applied at time zero, and a collection of tactoids imaged at 0, 120, 210, 640, and 1080 seconds. (f) to (i): The field is switched off and the same tactoids are imaged after 230, 380, 530, and 820 seconds following the removal of the electric field. Figure reproduced with permission from Ref. [40].

In Refs. [70, 73] this discrepancy was elucidated by suggesting that the response of droplet shape and the director field occurs on different time scales: Initially the anchoring enslaves the director field and forces it to follow the droplet shape. Only after the droplet shape has relaxed, then the director field starts relaxing. This eventually leads to the final relaxation of the droplet shape. which in turn leads to the subsequent relaxation of the shape of the drop to the actual equilibrium value in the very much later stages of the process. Indeed, Mezzenga and collaborators recently also suggested that tactoid equilibration might be kinetically controlled, leading to very long-lived metastable states [79]. This, then, would also explain the large scatter in tactoid shape and director field in dispersions that have been left to equilibrate for a long time, in that full equilibrium might not yet have been reached for the tactoids themselves. This is remarkable, given that they typically measure from ten to a few hundreds of  $\mu\text{m}$  in length [6, 13].

In this article, we follow up on our previous work [73], where we investigated the equilibrium shape and structure of nematic tactoids in an external alignment field, and introduce a relaxational dynamics based on two reaction coordinates. These reaction coordinates describe (i) the elongation of a tactoid with a prescribed spindle shape, and (ii) the degree of deformation of the director field where we prescribe the geometry of the deformation. The prescribed droplet shape and director-field geometry allows us to straightforwardly evaluate the well-known Oseen-Frank elastic free energy as well as the surface free energies that we use as input for our dynamical theory. For the surface free energy, we use the ansatz of Rapini and Papoular [43]. By construction, the steady-state solution to our equations produces the optimal aspect ratio and degree of curvature of the director field, given the volume of the drop and the strength of the alignment field [73].

We find that the elongation of tactoids in an electric field is *entirely* a kinetic effect. Depending on the ratio of the two fundamental relaxation rates associated with the two reaction coordinates, we either obtain a monotonic time evolution of both the aspect ratio and curvature of the director field, or a monotonic response of the curvature of the director field and an overshoot in the aspect ratio of the tactoids. The actual response times depend strongly on the strength of the electric field and the volume of the tactoids, appropriately scaled to the elastic constants and interfacial free energies associated with the nematic. Curve-fitting to the experimental data of Metselaars and collaborators [40] gives reasonable agreement, showing that the relaxation of the bipolarity of the director field must be extremely sluggish. The cause of this remains unclear and requires further study.

## 3.2 Methods

We have not been able to analytically evaluate the various integrals, except when the tactoids are extremely elongated and the opening angle becomes very small. In that case, asymptotic relations may be obtained as well as robust scaling estimates [30, 73]. Since we do not wish to restrict ourselves to large aspect ratios, we rely on a numerical evaluation of the integrals. For this, we employ the Mathematica software package [80] and use the *NIntegrate* function to compute integrals and the *D* function to calculate derivatives.

Now that we have formulated our free energy in terms of the two reaction coordinates  $\alpha$  and  $y$ , we are able to formulate our relaxational theory in terms of the generalized forces:

$$\begin{aligned}\frac{\partial\alpha}{\partial t} &= -\tilde{\Gamma}_\alpha \frac{\partial F}{\partial \alpha}, \\ \frac{\partial y}{\partial t} &= -\tilde{\Gamma}_y \frac{\partial F}{\partial y},\end{aligned}\tag{3.1}$$

where we choose to ignore the contribution of cross terms [81], the main reason being to limit the number of adjustable parameters in our model. Here,  $\tilde{\Gamma}_\alpha$  and  $\tilde{\Gamma}_y$  are fundamental relaxation rates that have dimensions of  $\text{J}^{-1}\text{s}^{-1}$ , so reciprocal Joules per second. Because  $y$  describes the deformation of the director field relative to the length of a tactoid this would arguably require the collective reorientation of the colloidal particles in the nematic phase. Hence, we would expect  $\tilde{\Gamma}_y$  to be inversely proportional to a rotational viscosity of the nematic phase. Relaxation of the aspect ratio of the droplets requires the transport of material in both the isotropic and nematic phases. It would therefore seem sensible to presume the relaxation rate  $\tilde{\Gamma}_\alpha$  to be some average of the relevant viscosities of the two phases [46].

For dimensional reasons this then implies that both rates should also be inversely proportional to some volume scale. Considering that the volume scale must represent the volume in which the viscous dissipation takes place, we conclude that both rates must be inversely proportional to the volume  $V$  of a tactoid. Hence, we write for our dynamical equations in terms of the dimensionless free energy  $f$  and tactoid volume  $v$  as

$$\begin{aligned}\frac{\partial\alpha}{\partial t} &= -\frac{\Gamma_\alpha}{v} \frac{\partial f}{\partial\alpha}, \\ \frac{\partial y}{\partial t} &= -\frac{\Gamma_y}{v} \frac{\partial f}{\partial y},\end{aligned}\tag{3.2}$$

where  $\Gamma_\alpha = \tilde{\Gamma}_\alpha V \sigma^2 / (K_{11} - K_{24})$  and  $\Gamma_y = \tilde{\Gamma}_y V \sigma^2 / (K_{11} - K_{24})$  are our scaled fundamental rates with dimensions of reciprocal seconds that do no longer depend on the volume of a drop. Our approach should be equivalent to but extends that of Weirich *et al.* [17] and of Almohammadi *et al.* [77], who balance the rate of change in mechanical energy with the rate of energy dissipation for fixed values of our parameter  $y$ .

To numerically integrate the two rate equations described in Eq. 3.2, we apply the (forward) Euler method function within the Mathematica package [80]. As initial conditions, we use the solutions of  $\partial f / \partial \alpha = \partial f / \partial y = 0$  in the absence of an external field, so for the case  $\Sigma = 0$ . A complete phase diagram describing the shape and director field of tactoids as a function of the dimensionless tactoid volume  $v$  and the dimensionless electric field strength  $\Sigma$  can be found in our earlier work [73]. Notice that we can make time dimensionless by defining  $\tau = t\Gamma_\alpha$ . In scaled time, our dynamical theory therefore introduces a single additional dimensionless group, namely  $\gamma \equiv \Gamma_y / \Gamma_\alpha$ . In our numerical evaluation of the kinetic equations, we choose to make use of a time-adaptive approach in order to efficiently

deal with the fast and slow processes that turn out to characterize the response of tactoids. This means that we dynamically adjust the time step, referred to as  $d\tau$ , during each evaluation step. Specifically, we steadily increase  $d\tau$  by a factor of 1.01 and assess the difference between the new values of  $\alpha$  and  $y$  relative to the ones of the previous time step. If the difference is less than 0.001 for  $\alpha(t+d\tau) - \alpha(t) < 0.001 \alpha(t)$  or  $y(t+d\tau) - y(t) < 0.001 y(t)$ , we continue with a new value of the time step  $d\tau$ . Conversely, if one or both of the differences exceeds the mentioned thresholds, we divided  $d\tau$  by a factor of 50 in each subsequent time step. This adaptive approach is particularly useful in the late stages of simulation when changes in  $\alpha$  and  $y$  become exceedingly small, allowing us to expedite the numerical evaluation of the kinetic equation.

Having presented the main ingredients of our theory, we next discuss our most salient findings and compare our results with the experimental data of Metselaar *et al.* [40].

### 3.3 Results

To determine the conditions under which elongated tactoids can be observed, even if only transiently, it is important to consider the following. As is now well established, small nematic tactoids tend to have a uniform director field, while for sufficiently large ones the director field is (for all intents and purposes) bipolar [6, 29, 30]. Switching on an electric field only acts to reorient tactoids with a uniform director field but does not affect their elongation. Bipolar ones reorient and do not become more elongated if their volume is smaller than some critical value [40]. If sufficiently large, bipolar tactoids may elongate substantially under the action of the field but only if somehow the director field remains

bipolar and does somehow not immediately respond to the electric field [70, 73]. This can only happen if (i) the ratio of the two fundamental relaxation rates  $\gamma = \Gamma_y/\Gamma_\alpha$  is sufficiently small and (ii) the volume of the drop is sufficiently large for the electric field to be able to deform it. Making use of the scaling theory of our previous work [73], we deduce by balancing the interfacial and Coulomb free energies that the latter happens if  $v \gg \Sigma^{-1/3}$ . Note that, typically, the anchoring strength varies from about 1.5 to 6 [6]. For the tactoids to be bipolar, we must in addition insist that  $v \gg \omega^{-5/2}$  [29]. The maximum aspect ratio we expect to find, provided that these conditions are met, is  $R/r \sim \Sigma^{3/7}v^{1/7} \gg 1$  at the level of the scaling theory, so ignoring any constants of proportionality. This shows that the field strength more strongly impacts upon the maximum aspect ratio than the volume does. Our numerical evaluation of the kinetic equations confirms this.

Now that we know under what conditions we might expect transients to arise, we first explore how the ratio of fundamental relaxation rates  $\gamma$  influences the aspect ratio  $x$  and bipolarity  $y$  of tactoids. Figure 3.2 shows the aspect ratio *vs.* time for different values of  $\gamma$ , and fixed values of  $v = 10^5$ ,  $\Sigma = 65$ ,  $\omega = 1.3$ , and  $\kappa = 20$ . The latter two values we obtain from the properties of chitin tactoids in the absence of an electric field [73]. For these values of the parameters, we have  $v\Sigma^3 \gg 1$ , and based on the scaling estimate we expect to see an overshoot of the aspect ratio of the order of 10 to 100 if  $\gamma \ll 1$ . Figure 3.2 confirms this: the aspect ratio goes through a maximum before reaching its equilibrium value in the late stages of the process, and the maximum value reached increases as the magnitude of  $\gamma$  decreases. Also, the smaller the value of  $\gamma$ , the longer lived the high-aspect-ratio states are. For late times, when the tactoids approach the true equilibrium state, the value of

aspect ratio is not so large and does not depend on the ratio of  $\gamma$ . Hence, this confirms that large aspect ratios are possible only for smaller values of  $\gamma$  when the director field has not yet fully equilibrated. Fig. 3.3, showing the degree of bipolarity  $y$  as a function of time, confirms this.

Fig. 3.3 shows that, not entirely unexpectedly, the smaller the value of  $\gamma$  the more slowly the changes in bipolarity occur. This prevents the immediate alignment of particles and therefore that of the director field with the applied external electric field. The particles remain essentially enslaved to the surface anchoring until the internal dynamics allow them to break free from this and relax to the equilibrium value. Fig. 3.3 shows that there is some feedback between the two: whilst the bipolarity does increase monotonically with time, it does seem to develop a weak “shoulder” around the region where the aspect ratio of the droplets reaches its maximum. As time passes, the bipolarity of the tactoid increases reaching its equilibrium value, which leads to a reduction in the aspect ratio to a value consistent with our previous equilibrium results [73]. This is the key reason for the presence of a maximum value for the aspect ratio as a function of time.

We next investigate the impact of the strength of the external electric field on the shape and director-field structure of nematic tactoids. Figure 3.4 shows that the final, equilibrium value of the aspect ratio does not appreciably depend on the electric field strength, at least not for the values of  $\Sigma = 10, 100, 200, 400, 1000$  and  $2000$  shown in the graph and the dimensionless volume of the drop  $v = 10^2$ . This is consistent with previous equilibrium studies, showing that the final state is characterized by a more or less uniform director field and an aspect ratio that approaches the value of  $2\sqrt{\omega}$  if the field is sufficiently

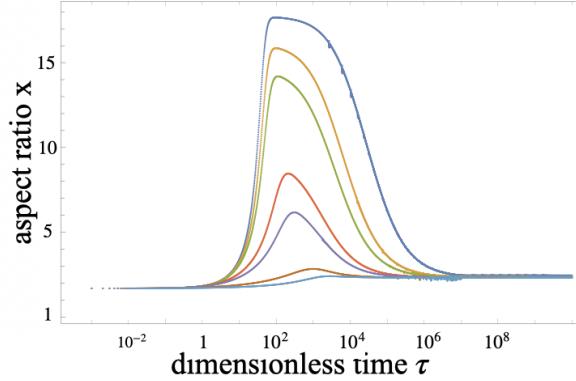


Figure 3.2: Aspect ratio  $x$  of a tactoid as a function of dimensionless time  $\tau$  for different values of the ratio  $\gamma$  of the fundamental relaxation rates associated with the response of the director field and that of the aspect ratio. From top to bottom:  $\gamma = 0.01$  (blue), 0.05 (yellow), 0.1 (green), 0.5 (red), 1 (purple), 10 (brown), 50 (light blue). The dimensionless volume of the droplet is  $v = 10^5$ , the anchoring strength  $\omega = 1.3$ , the dimensionless strength of the electric field  $\Sigma = 65$ , and the ratio of the bend and splay elastic constants  $\kappa = 20$ .

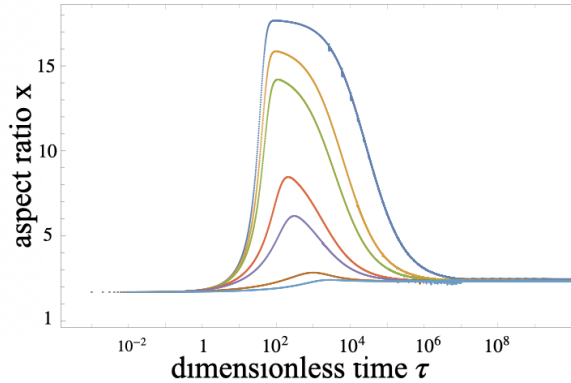


Figure 3.3: Bipolarity  $y$  of a tactoid as a function of dimensionless time  $\tau$  for the different values of the ratio  $\gamma$  of the fundamental relaxation rates associated with the response of the director field and that of the aspect ratio. From bottom to top:  $\gamma = 0.01$  (blue), 0.05 (yellow), 0.1 (green), 0.5 (red), 1 (purple), 10 (brown), 50 (light blue). The dimensionless volume of the droplet is  $v = 10^5$ , the anchoring strength  $\omega = 1.3$ , the dimensionless strength of the electric field  $\Sigma = 65$ , and the ratio of the bend and splay elastic constants  $\kappa = 20$ .

strong [70, 73]. Still, transients with a large aspect ratio do arise with a maximum that increases with the strength of the electric field. We notice that the transients are very

long-lived and more so the larger the field strength. A careful review of the plots of the maximum value of aspect ratio found in Fig. 3.4) shows that it is proportional to  $\Sigma^{0.42}$ . The exponent is close to the prediction of  $3/7$  mentioned earlier. Fig. 3.4 also reveals that the time for a tactoid to reach its maximum elongation becomes shorter as the strength of the electric field becomes stronger. In fact, we find numerically that this time scales as  $\Sigma^{-0.77}$ .

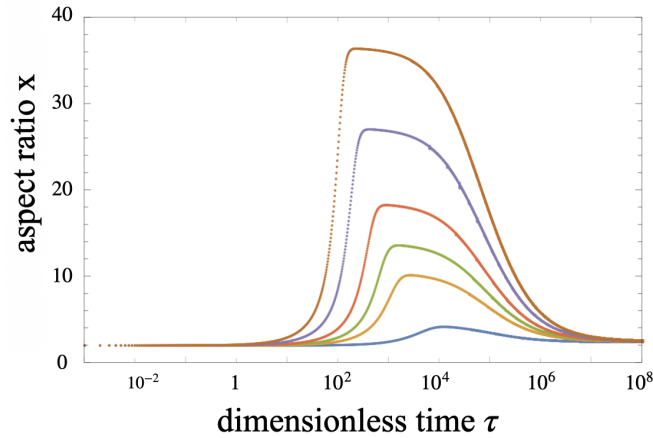


Figure 3.4: Aspect ratio  $x$  of tactoid as a function of dimensionless time  $\tau$  for different values of the dimensionless electric field strength  $\Sigma = 10, 100, 200, 400, 1000, 2000$  (bottom to top). The dimensionless volume of the droplet is  $v = 10^2$ , the anchoring strength  $\omega = 1.3$ , and the ratio of the bend and splay elastic constants  $\kappa = 20$ . The ratio of the fundamental relaxation rates was set at a value of  $\gamma = 1/15$ .

Let us now explore how the bipolariness  $y$  of tactoids depends on the strength of the electric field  $\Sigma$ . As shown in Fig. 3.5, the equilibrium value of bipolariness increases with time, and more so the stronger the electric field. This means that the virtual point defects (the focal points of the extrapolated bipolar director field) move away from the poles of the tactoids and the director field becomes increasingly more homogeneous. A careful examination of our numerical results for late times shows that it increases as  $\Sigma^{0.48}$ . This is consistent with the equilibrium theory of Safdari *et al.* [73], which predicts that the

bipolariness grows with the field strength as  $\Sigma^{0.5}$ . Comparing Figs. 3.4 and 3.5 also shows that the relaxation of the bipolariness to its equilibrium value is very much more sluggish than that of the aspect ratio. In fact, it is more sluggish than what we would expect based on the value of  $\gamma$ , which in the figure is equal to  $1/15$ . This is not all that surprising given that any director field with bipolariness above a value of, say, three is difficult to distinguish from a uniform director field. This implies that any response of the aspect ratio must be very small beyond that.

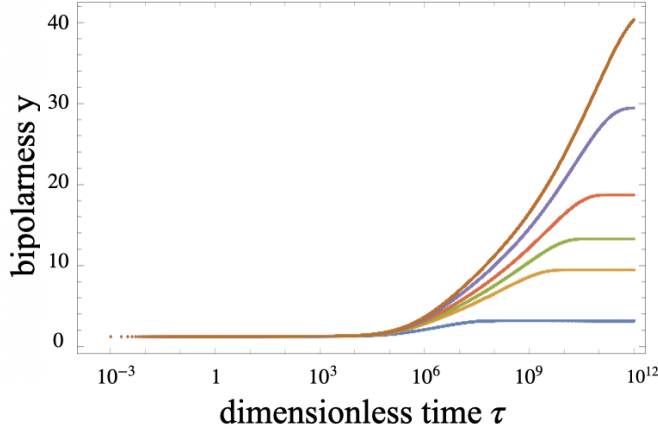


Figure 3.5: Bipolariness of tactoid  $y$  as a function of the dimensionless time  $\tau$  for the different electric field strength  $\Sigma = 10, 100, 200, 400, 1000, 2000$  (bottom to top). The dimensionless volume of the droplet is  $v = 10^2$ , the anchoring strength  $\omega = 1.3$ , and the ratio of the bend and splay elastic constants  $\kappa = 20$ . The ratio of the fundamental relaxation rates was set at a value of  $\gamma = 1/15$ .

Finally, we investigate the effect of the volume of a tactoid on both its bipolariness and aspect ratio for a given external field and a given asymmetry in the relaxation dynamics of the director field and the droplet shape. From the earlier-mentioned scaling theory we expect that the director field is essentially uniform and the drop does not respond to any alignment field other than aligning along the field direction if the dimensionless volume  $v$  is

smaller than  $\omega^{-5/2}$ . For our choice of  $\omega = 1.3$ ,  $v$  needs to be much larger than unity for it to have a noticeable degree of curvature of the director field. For the external field to be able to straighten out the curved director field,  $v$  must be larger than about  $\Sigma^{-5/4}$  according to the scaling theory. If we set  $\Sigma = 65$ , this implies that a tactoid responds to that field as long the tactoid is bipolar, so  $v \gg 1$ . The maximum value of the aspect ratio scales then with the tactoid volume as  $v^{1/7}$ , which predicts a very weak dependence on the volume.

Figures 3.6 and 3.7 show how a variation of the dimensionless volume for  $v = 1, 310, 2340$  and  $5780$  affect the time-evolution of the aspect ratio and bipolarity following the switching on of the electric field for  $\Sigma = 65$ ,  $\omega = 1.3$ ,  $\gamma = 0.1$  and  $\kappa = 20$ . The figure confirms once more that the equilibrium value of the aspect ratio of a tactoid does not, as expected, strongly depend on its volume [70, 73]. For  $v = 1$  the director field is almost uniform with  $y \approx 3$ , so for this volume, the external field has very little impact on both the aspect ratio and bipolarity. The larger tactoids are all essentially bipolar at time zero, with a bipolarity  $y$  close to unity, and these do respond to the switching on of the field. The aspect ratio of this larger droplet does exhibit transient overshoots, while their bipolarity increases monotonically with time as the field straightens the director field.

Figure 3.6 confirms that the maximum value of the aspect ratio increases only weakly with the dimensionless volume that we varied over four decades in magnitude. The timescale required to reach this maximum value decreases with the volume of the drop but also not very strongly. The same can be said about the relaxation of the director field. The equilibrium value of the bipolarity does depend on the volume albeit not very sensitively. According to the scaling theory of Safdari *et al.*, which is confirmed by numerical

minimization of the free energy [73], we expect  $y$  to scale as  $v^{1/6}$ . The late-stage results shown in Fig. 3.7 agree with this prediction, as they should.

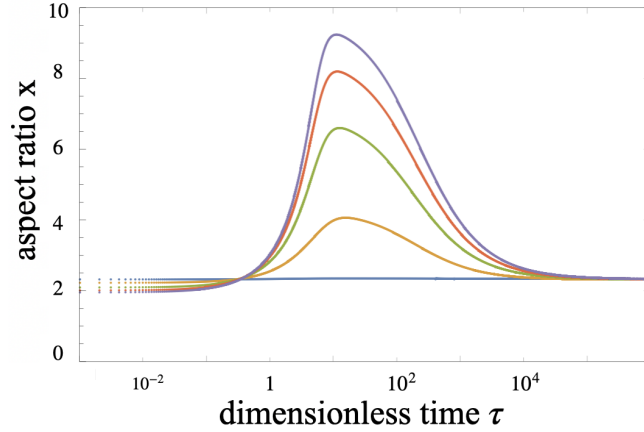


Figure 3.6: Aspect ratio of tactoids  $x$  as a function of time for the different dimensionless volume  $v = 1, 310, 2340, 5780, 10000$  (bottom to top, central part). The electric field strength is  $\Sigma = 65$ , the anchoring strength  $\omega = 1.3$ , the ratio of the fundamental relaxation times  $\gamma = 1/15$  and the ratio of the bend and splay elastic constants  $\kappa = 20$

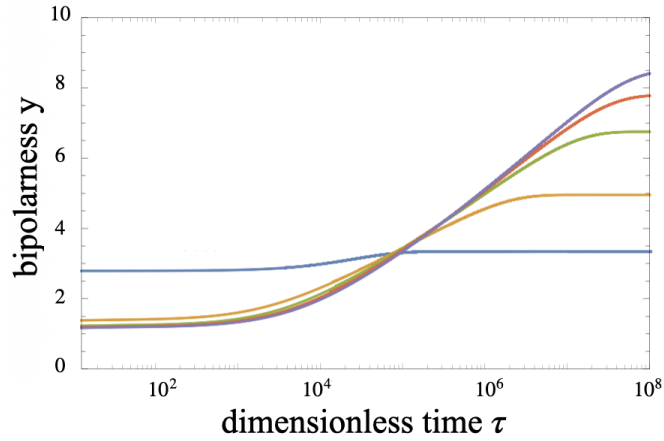


Figure 3.7: Bipolarity of tactoid  $y$  as a function of the dimensionless time  $\tau$  for different dimensionless volume  $v = 1, 310, 2340, 5780, 10000$  (bottom to top on the right). The electric field strength is  $\Sigma = 65$ , the anchoring strength  $\omega = 1.3$ , the ratio of the fundamental relaxation times  $\gamma = 1/15$  and the ratio of the bend and splay elastic constants  $\kappa = 20$ .

After having investigated the response of the switching on of an electric field, we ask ourselves the question what happens when the electric field is turned off and the external field is removed? Specifically, we are interested in understanding the dynamics of the change in aspect ratio during the transition. Does it revert to its initial state swiftly? Or does it remain relatively unchanged? This is a relevant question, because Metselaar *et al.* find that switching off of the field prior to full relaxation in the presence of the field the largest tactoids seem not to revert to the field-free aspect ratios in roughly the same amount time as when the field was switched on [40]. See also Figure 3.1, noting that quantitative data are not available.

To address these questions, we turn on and next turn off the electric field once the tactoids have elongated to a certain fraction of the maximum value for  $\Sigma = 425$  and  $v = 5 \cdot 10^3$ . The results of our numerical calculations are presented in Fig. 3.8. Consistent with the experiments of Metselaar *et al.* [40], we find that the tactoids take more time to approach their equilibrium configurations than the time required to elongate them. For the case shown, the difference in time amounts to three or four orders of magnitude. We notice that the state of elongation at which the field is switched off does not seem to strongly influence the (dimensionless) relaxation time, which for all cases shown in the figure is about 70,000. The blue curve in Fig. 3.8 shows the situation when the electric field remains turned on, showing a considerably slower convergence to the equilibrium state in the presence of the field compared to the cases where the field was switched off, reverting to the equilibrium state in the absence of an alignment field. Both are much larger, though, than the time it takes to reach peak elongation. This illustrates that there are many very divergent

timescales involved in the relaxation of tactoids, highlighting the non-linear character of the kinetics at hand.

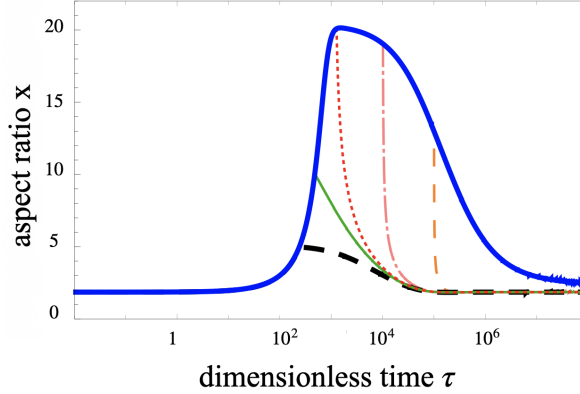


Figure 3.8: The evolution of the aspect ratio  $x$  as a function of the dimensionless time  $\tau$ . The thick solid blue curve shows the response to switching on of the field at time zero. The curves in bold dash black, solid green, dotted red, dash-dotted pink, and thin dashed orange show what happens after shutting of the field. The dimensionless volume of the droplet is  $v = 5 \cdot 10^3$ , the anchoring strength  $\omega = 1.3$ , the strength of the electric field is  $\Sigma = 425$ , the ratio of the bend and splay elastic constants  $\kappa = 20$ , and the ratio of the fundamental relaxation rates  $\gamma = 1/15$ .

In the next section, we apply the theory developed here in order to interpret the experimental results of Metselaar *et al.* [40].

### 3.4 Comparison with Experiment

In a series of measurements, Metselaar *et al.* recently measured the dimensions of tactoids in different batches of an aqueous dispersion of chitin nanocrystals as a function of time, following the application of a high-frequency AC electric field [40]. Experiments were done for root-mean-square field strengths in the range from 160 V/mm to 450 V/mm and frequencies ranging from 300 to 700 kHz. Even though the findings between different

experiments differed quantitatively, qualitatively the results are consistent with each other. Despite the small difference in the dielectric properties of the coexisting isotropic and nematic phases, which are dominated by the contribution from the aqueous solvent, it turns out that electric fields can significantly elongate tactoids at least if these are of sufficiently large volume. See also Figure 3.1. In our previous work [73], focusing on the thermodynamic properties of tactoids in an electric field, we showed we could only get reasonable agreement between theory and experiment for the maximum elongation by invoking a restricted equilibrium. In this restricted equilibrium, we fixed the bipolarity of the tactoids to the equilibrium values obtained in the absence of the field.

Our aim here is to relax the restricted equilibrium, and adjust and calibrate our relaxational model in order to achieve the closest possible alignment with the experimental data. Given that the available data from different experiments agree only qualitatively, we seek to reproduce trends rather than achieve quantitative agreement. For this, we use model parameters obtained by fitting the theory to the available experimental data on field-free aspect ratio for a range of tactoid volumes varying four orders of magnitude [73]. In our previous work, we found the values for the anchoring strength  $\omega = 1.3$ , the ratio of bend to splay elastic constants  $\kappa = 20$ , and the extrapolation length  $(K_{11} - K_{24})/\sigma = 4 \mu\text{m}$ . Hence, in the conversion of dimensionless volume  $v$  to dimension-bearing volume  $V$  we multiply  $v$  by 64 to change the unit of our dimensionless volumes to  $\mu\text{m}^3$ .

Fig. 3.9 shows the aspect ratio  $x = R/r$  vs. the actual time  $t$  in seconds for three different tactoid volumes of  $V \simeq 20 \times 10^3$ ,  $150 \times 10^3$  and  $370 \times 10^3 \mu\text{m}^3$ . Shown are the ratios of lengths and widths of the chitin tactoids obtained experimentally by Metselaar *et al.* [40],

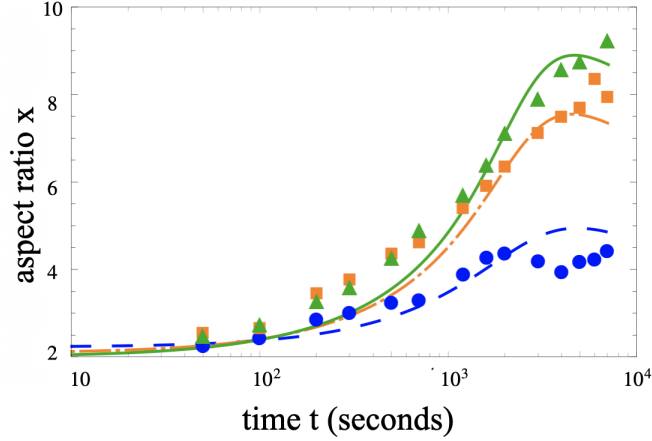


Figure 3.9: Time evolution of the aspect ratio of three droplets of different dimensionless volumes  $v$ , indicated by different colors (from top to bottom on the right): solid green for  $v = 5780$ , dash-dotted orange for  $v = 2340$  and dashed blue for  $v = 310$ . Dots are experimental data points extracted from Ref. [40] and the drawn curves display our curve fits. We set the anchoring strength  $\omega = 1.3$ , the ratio of bend to splay  $\kappa = 20$ , the coefficient of the electric field strength  $\Sigma = 190$  the ratio of relaxation rate  $\gamma = 0.5$  and  $\Gamma_\alpha = 1.6 \times 10^{-4} s^{-1}$ . The  $r^2$  values for the quality of the curve fits are 0.61, 0.91, and 0.94 for dashed blue, dash-dotted orange and solid green curve respectively.

together with the solid curves that are the result of our curve-fitted numerical solutions to the kinetic equations. Each color corresponds to a different volume. To find the best fit, we applied a hyperparameter grid search (on the parameters  $\Sigma$ ,  $\gamma$  and  $\Gamma_\alpha$ ) [82] and minimize the so-called cost function,  $\sum(x_{\text{the}} - x_{\text{exp}})^2/N$  with  $N$  the number of data points, a measure for the mean-square distance between the aspect ratio of the theoretical prediction  $x_{\text{the}}$  and the experimental data points  $x_{\text{exp}}$ . The values for the various parameters that we find are  $\gamma = 0.5$ ,  $\Sigma = 190$  and  $\Gamma_\alpha = 1.6 \times 10^{-4} s^{-1}$ .

We get reasonable agreement between theory and experiments, noting that we use the same values of all of the parameters except the volume of the drops, with coefficients of determination  $r^2$  between 0.61 and 0.95. The curves clearly show that whilst the initial response time goes down with increasing droplet volume, final equilibration actually slows

down and takes longer the larger the tactoids. Our curve-fitting procedure produces maxima that are not quite observed yet in the data, except perhaps for the smallest volume. It is important to point out that setting  $\gamma \ll 1$  produces curves for which the maximum moves to much larger times. In fact, setting  $\gamma = 0$  and suppressing the maximum entirely produces curve fits that have much smaller values of  $r^2$ . In fact, a simple exponential relaxation, put forward in a slightly different context in Refs. [17, 77], cannot describe the experiments in any satisfactory way (results not shown). We expect that for times much larger than, say, 7000 s, the experiments should show a downturn in the aspect ratio. This, now, is a prediction amenable to experimental verification.

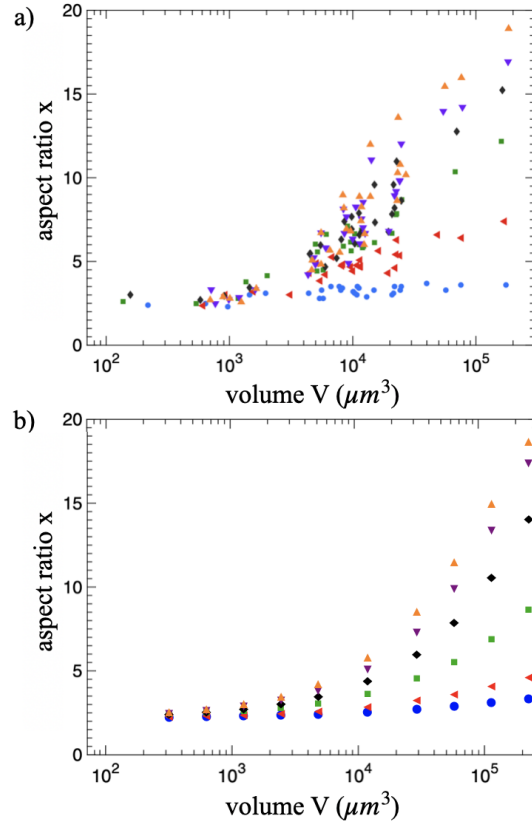


Figure 3.10: Aspect ratio of tactoids  $x$  as a function of their volume  $V$  in  $\mu\text{m}^3$  for different times. a) Experimental findings for chitin in water, taken from [40]. b) Our theoretical predictions are based on the curve fitting. Parameter values for the theoretical predictions:  $\omega = 1.3$ ,  $\kappa = 20$ ,  $\Sigma = 500$ ,  $\gamma = 1/20$  and  $\Gamma_\alpha = 1.6 \times 10^{-4} \text{s}^{-1}$ . Results for the same moment in time are presented with the same color. Blue circles: 120 seconds, red triangles: 210 s, green squares: 410 s, black diamonds: 640 s, purple triangles: 850 s, orange triangles: 1080 s. See also the main text.

In Figure 3.10a) and b) we compare for the time evolution of tactoids ranging three orders in magnitude in size following the switching on of the electric field. Figure 3.10a) shows the experimental findings for the aspect ratio  $x$  of the tactoids as a function volume, and Figure 3.10b) the results of our numerical simulations, where we used the value of  $\Sigma = 500$  estimated from the restricted model of Ref. [73]. The other parameters we set at  $\gamma = 0.05$  and  $\Gamma_\alpha = 1.6 \times 10^{-4} \text{ s}^{-1}$  to obtain reasonable agreement (by eye). Note that the data set of the results of this figure is different from the one shown in Fig. 3.9. Different colors and symbols are used to denote various points in time. Agreement is semi-quantitative. The figures show that for larger droplets, a gradual increase in elongation occurs over time due to the coupling to the external field. In contrast, smaller droplets exhibit minimal changes in their aspect ratios, because the Coulomb energy is not strong enough to be able to affect any changes in the droplet shape as it is strongly volume-dependent. The behavior predicted from our model closely mirrors the trends observed in the experimental data points, indicating an agreement between our simulations and the experimental observations.

We stress that whilst from our perspective the experiments on tactoids in dispersion of chitin in water can only be understood in terms of an overshoot, so far we do not have definitive experimental proof for it. On the other hand, overshoots have also been seen in a more conventional setting of a droplet of water in oil albeit that in this case the overshoot is more modest and arguably the result of a very different physical mechanism [83]. Our hope is that the present work acts to stimulate follow-up experimental work on nematic tactoids in electric fields.

## Chapter 4

# The Dynamics of Viruslike Capsid Assembly and Disassembly

### 4.1 Introduction

There are two major aspects to how viruses in general, and more specifically unenveloped, single-stranded RNA (ssRNA) viruses, infect living cells. The first is the role of the viral genome, responsible for the replication of the virus inside of the host cell. The second is that of the capsid, the protein shell that protects the genome of the virus until it enters the cell in order to release its genome, and produce large numbers of virus particles from the replicated genome and protein components. Therefore, virus capsids must be able to function as a protective transporter as well as a deliverer of genome. These two functions must be executed via controlled shell disassembly and reassembly, depending on the environment and stage in the reproduction cycle [84, 85, 86, 87, 88, 89].

Experimentally, in order to study the physical aspects of the disassembly and reassembly of viruses use is often made of a simple, icosahedral plant virus known as Cowpea Chlorotic Mottle Virus (CCMV). *In vitro* studies have shown that CCMV disassembles spontaneously under appropriate solution conditions. This occurs when the buffer solution containing the virus particles is suddenly changed from neutral to basic pH at high ionic strength [90, 91, 92]. Conversely, solutions containing the coat proteins of CCMV, or those of other viruses such as Brome Mosaic Virus (BMV) and Hepatitis B Virus (HBV), can be made to spontaneously encapsulate negatively charged cargo, which does not need to be the native genome but may include heterologous ssRNAs, synthetic polyanions, or even nanocolloids [93, 94, 95, 96].

The self-assembled particles often have the same size or structure as the native virus but this is not always the case [97, 98, 99, 100, 101]. In some cases, mixtures of differently sized or structured particles self-assemble, as in fact, it is the case for HBV even *in vivo* [102, 103]. *In vitro*, such size competition is often observed too, where the predominance of a certain particle size, or so-called *T*-number, appears to depend on the size of the cargo and even on the solution conditions [104, 105, 106]. We note that under appropriate physico-chemical conditions, or by modifying the coat proteins, e.g., removing or modifying the RNA binding domain, empty or filled capsids of different size and shape may also be produced [107, 108, 109, 110, 111, 112].

The spontaneous conversion between assembled and disassembled states or that between different sizes of assembled particles, with or without cargo, is often modeled in terms of a process akin to a thermodynamic phase transition [91, 105, 106, 113, 114, 115, 116, 117].

This is possible, because (i) the number of proteins required to form a shell is sufficiently large, typically many tens to hundreds of proteins, and (ii) the number of intermediates consisting of incomplete assemblies is exceedingly small in comparison to the number of free coat proteins and complete particles [118, 119]. The latter is believed to be caused by a rim tension associated with proteins at the edge that miss contact with neighboring proteins in the incomplete shell [120]. Scattering experiments [121] and computer simulations seem to support this view [85, 122].

While we have a reasonable understanding of the thermodynamics of viruses and virus-like particles, formed by empty capsids and capsids containing heterologous RNAs, synthetic polyanions, nanocolloids *etc.*, our understanding of the kinetics of assembly and disassembly of such products remains very sketchy indeed [86, 123, 124, 125]. Experimentally, this is in part due to limitations in the spatial and time resolution of the intermediate structures between fully formed capsids and the free subunits in solution [84, 121]. The situation is even more complicated in the presence of a polyelectrolyte cargo [126], where different assembly pathways have been identified that are referred to as “concerted” or “en mass” *vs* “sequential”, which may depend on the solution conditions [93, 123, 127, 128, 129, 130]. Both seem to be governed by nucleation and growth stages.

Clearly, the assembly and disassembly of *empty* capsids is, in principle, conceptually the most simple as it involves only the coat proteins. Even if we focus on the self-assembly kinetics of empty capsids, until recently the experimental focus was mainly on assembly not disassembly. This is probably due to disassembly being a significantly more sluggish process than assembly is, expressing itself in a strong hysteresis of the assembly

and disassembly of virus capsids [120, 131, 132]. Available experimental data on a variant of the HBV coat protein suggests that the disassembly pathway from fully formed capsid to free monomers includes a stage where fractal aggregates are formed albeit that this may well depend on the solution conditions [131]. CCMV capsids seem to involve two types of intermediate states, one large and one small [125]. Again, a lack of spatial and temporal resolution experimentally hampers obtaining a detailed picture of how precisely a virus capsid disintegrates. Computer simulations suggest that in spite of its stochastic character the onset of disassembly may involve only a limited number of distinct contacts between coat proteins [133].

In a recent study, Timmermans *et al.* functionalized the coat protein of CCMV and studied the reversible conversion between a  $T = 3$  capsid at low pH and high ionic strength and a  $T = 1$  capsid at high pH and lower ionic strength [134]. For non-functionalized coat proteins of CCMV, empty  $T = 3$  capsids form due to hydrophobic interactions overwhelming the electrostatics in a solution with 500 mM NaCl at a pH of 5.0, while no structures form when the pH is increased and ionic strength decreased [135]. By functionalizing the coat protein with elastin-like polypeptides, the hydrophobic interactions of the polypeptides at a higher pH of 7.5 with a lower ionic strength of 100 mM NaCl dominate the electrostatic interactions and form the smaller species of capsid [134]. This conversion requires the disassembly of one species in order to assemble the other, as most of the coat proteins present in solution turn out to reside in capsids and not in free protein. The conversion of the modified CCMV coat proteins from  $T = 1$  to  $T = 3$  occurs much more slowly than that from  $T = 3$  to  $T = 1$ . To rationalize this finding, Timmermans *et al.* extended a

classical nucleation theory for virus capsid assembly of a single capsid size to two capsid sizes, introducing also a disassembly pathway [120], which allowed them to interpret their results in terms of free energy barriers between the free monomers, and the  $T = 1$  and  $T = 3$  assembled states, as well as the differences in the binding free energy gains of assembly.

While classical nucleation theory seems to be able to describe the final assembly products and match the experimental data quite well up to a few days after a quench, that is, a sudden change in solution conditions, the curve fitting procedure turns out numerically demanding due to the large number of adjustable system parameters and the scatter in the data. Hence, we ask the question if the experiments of Timmermans *et al.* can also be described by a much simpler model, based on what in the theoretical phase transition community is called Model A kinetics [136, 137]. This kind of kinetics is purely relaxational and hinges on the concept of generalised forces in a free energy landscape. It was applied before to describe the assembly and disassembly kinetics of a single type of empty capsid [137]. Here, we extend it to mixtures of monomers and two species of capsid, and focus on the conversion between these two types of capsid following a quench. For deep quenches nucleation barriers are small, and such an approach should be appropriate.

The advantage of a Model A type of kinetic theory is that it involves the deterministic time evolution of the conversions between individual coat protein subunits and fully formed assemblies, which can be solved analytically for shallow quenches. Analytical solutions are also possible for deep quenches at experimentally relevant timescales, namely for early and late times. This circumstance allows us to identify driving forces in different stages of the size conversion. Indeed, our calculations shows that in the early stages of the

conversion the translational entropy of the free subunits drives the assembly of one of the capsid species, whilst in the later stages the impact of differences in the binding free energy of the two species of capsid predominates.

The remainder of this paper is structured as follows. We first reiterate the equilibrium theory for capsid competition, and analyze in detail the equation of state describing the amount of proteins free and in  $T = 1$  and  $T = 3$  capsids as a function of the overall concentration of coat proteins and two binding free energies. Next, we write the kinetic equations for the fraction of proteins in the various species within the framework of Model A kinetic theory [136], and express these in terms of the equilibrium quantities. We next investigate analytically the evolution of the distribution of proteins for shallow quenches, when initial and final solution conditions are close together, producing two elementary time scales. By numerically solving the equations we confirm that under most quench conditions, even if the initial and final states of aggregation are very different, the approach to equilibrium involves two timescales that we are able to interpret. Next, we apply the theory to the experimental data of Timmermans *et al.* [134], where we conclude that for those experiments Model A kinetics describes the early and intermediate stages of the kinetics reasonably well, but fails to reproduce the ratio of assembly products at the final stage of experiments. It seems that an explicit description of nucleation processes is essential to explain the experimental findings. In the final section, we summarize our results, and discuss under what experimental conditions we expect our theory to work for all times.

## 4.2 Equilibrium theory for capsid competition

Our first goal is to set up a statistical thermodynamic model describing the competition between fully formed shells of different  $T$ -numbers as a function of the solution conditions, which acts to drive the dynamics of the process. Based on the equilibrium theory of capsid assembly, we need only consider the coat protein subunits free in solution and those present in the complete capsids; incomplete intermediate structures (partially formed capsids) are statistically highly improbable on account of a line tension associated with missing neighbors of coat proteins making up the cap rim [118, 119, 120, 137, 138].

Presuming the solution to be dilute, we write the dimensionless free energy  $f$  per coat protein as follows,

$$f = \eta_s \ln c \eta_s - \eta_s + \sum_T \left[ \frac{\eta_T}{q_T} \ln \frac{c \eta_T}{q_T} - \frac{\eta_T}{q_T} + \eta_T g_T \right] \quad (4.1)$$

in terms of the fraction of proteins in free solution  $\eta_s$  and those in the capsid species  $\eta_T$  with  $T = 1, 3, 4, 7, \dots$  the triangulation number of the capsids and associated aggregation number  $q_T$ . Below, we focus on the case where we only have two species in competition with each other, namely  $T = 1$  and  $T = 3$ , which are the most prevalent. (Competition between pseudo  $T = 2$  and  $T = 3$  has been observed in the context of encapsulation of polyanions by virus coat proteins [139].) Further,  $c \ll 1$  is the overall mole fraction of coat proteins in solution, and  $g_T$  the mean dimensionless binding free energy of a single coat protein in a complete capsid of size  $T$ . For stable capsids to form, the latter must be negative, and typically is in the range of  $-10$  to  $-20$  (in units of thermal energy) [106, 140].

The free energy Eq. (4.1) is the sum of an ideal mixing entropy (stemming from the translational entropy of each species) and the net binding free energy accounting for the subunit-subunit interactions in a fully assembled capsid [140]. The optimal distribution of the coat proteins over the various states of assembly minimizes the free energy, requiring that

$$\left(\frac{\partial f}{\partial \eta_T}\right)_{c, g_T, \eta_{T'} = \eta_{T', \infty}} = 0, \quad (4.2)$$

where we define  $\eta_{T, \infty}$  as the value of  $\eta_T$  under conditions of thermodynamic equilibrium. Note that we eliminate the fraction of coat proteins in solution from the free energy by making use of the conservation of mass by inserting the identity  $\eta_s = 1 - \sum_T \eta_T$ . Demanding eq. (4.2) to hold, the equations of state become

$$-\ln \left[ c \left( 1 - \sum_T \eta_{T, \infty} \right) \right] + \frac{1}{q_T} \ln \frac{c \eta_{T, \infty}}{q_T} + g_T = 0, \quad (4.3)$$

representing the law of mass action for all potentially present capsid species.

For the case in which we have a competition between two distinct capsids with triangulation numbers  $T$  and  $T' > T$ , mirroring the experiments of Timmermans *et al.* [134], Eq. (4.3) tells us that we need to solve two equations of state self-consistently, namely

$$\ln [c (1 - \eta_{T, \infty} - \eta_{T', \infty})] = \frac{1}{q_T} \ln \frac{c \eta_{T, \infty}}{q_T} + g_T, \quad (4.4)$$

$$= \frac{1}{q_{T'}} \ln \frac{c \eta_{T', \infty}}{q_{T'}} + g_{T'}. \quad (4.5)$$

Note that  $q_{T'}/q_T = T'/T$ , which is larger than unity if without loss of generality we presume that  $T' > T$ . Furthermore,  $q_T = 60T$  if the coat proteins are monomers and  $q_T = 30T$  if they are dimers as is the case for CCMV.

In the limit of very small degrees of assembly where most proteins remain in free solution and  $\eta_{T,\infty} \ll 1$ , Eqs. (4.4) and (4.5) can be solved to give rise to the solutions  $\eta_T \sim q_T c^{-1} (c/c_{*,T})^{q_T}$  and  $\eta_{T'} \sim q_{T'} c^{-1} (c/c_{*,T'})^{q_{T'}}$  with  $c_{*,T} = \exp(g_T)$  and  $c_{*,T'} = \exp(g_{T'})$  critical concentrations associated with the binding free energies  $g_T$  and  $g_{T'}$ . Since typically  $q_T, q_{T'} \gg 1$ , the transition between the capsid-poor and capsid-rich states is very sharp indeed. In fact, the larger the  $T$  number is, the sharper the transition.

Subtracting Eq. (4.4) from (4.5), and defining the difference in dimensionless binding free energies of the two species as  $\Delta g \equiv g_{T'} - g_T$ , we obtain a simple relation between the fraction of protein present in the two species of capsid

$$\eta_{T,\infty} = \alpha (\eta_{T',\infty})^{T/T'}, \quad (4.6)$$

where

$$\alpha \equiv \left(\frac{T}{T'}\right)^{T/T'} \left(\frac{q_T}{c}\right)^{1-T/T'} \exp(q_T \Delta g). \quad (4.7)$$

We immediately see that if  $\alpha \ll 1$ , which in essence implies  $\Delta g < 0$  as  $q_T \gg 1$ , we must have  $\eta_{T,\infty} \ll 1$ . In that case the  $T'$  species predominates. The two species are equally prevalent if  $\eta_T = \eta_{T'} = \alpha^{T'/(T'-T)}$  provided  $\alpha < 2^{-(T'-T)/T'}$  as by definition  $\eta_T + \eta_{T'} < 1$ . Figure 4.1 illustrates the predicted competition between  $T = 1$  and  $T' = 3$  capsids. As shown in the figure, for  $\alpha = 2^{-2/3} \simeq 0.63$  at relatively low degrees of assembly, most of the protein in

capsids reside in the  $T = 1$  structure. However, if almost all of the proteins present in solution are in capsids, they divide equally among both structures for  $\alpha \simeq 0.63$ . Since  $\alpha \propto c^{-1+T/T'} = c^{-2/3}$ , we conclude that keeping everything else constant but increasing the total protein concentration, the fraction of protein in  $T = 1$  capsids decreases relative to that in  $T' = 3$  capsids. This conclusion extends to any mixture of capsids with  $T' > T$ .

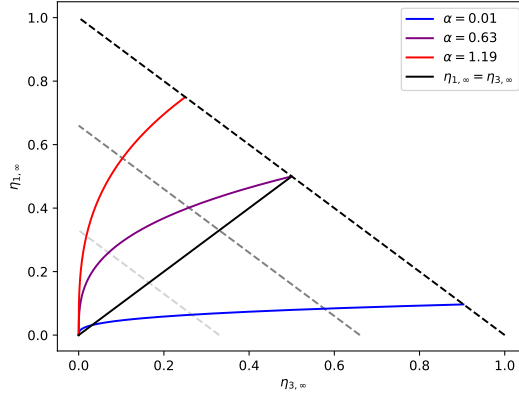


Figure 4.1: Relation between the fraction of protein in  $T = 1$  capsids,  $\eta_{1,\infty}$ , and that in  $T = 3$  capsids,  $\eta_{3,\infty}$  (4.6), for different values of the parameter  $\alpha$ , according to Eq. (4.7). From top to bottom:  $\alpha = 0.01$  (red),  $\alpha = 0.63$  (purple), and  $\alpha = 1.19$  (blue). The dashed lines demarcate the maximum value of  $\eta_{3,\infty}$  for every value of  $\eta_{1,\infty}$  for different maximum fractions of subunits present in capsids:  $\eta_1 + \eta_3 = 1$ ,  $2/3$  and  $1/3$  from top to bottom. The solid black line describes the special case  $\eta_{3,\infty} = \eta_{1,\infty}$ .

Since we have  $\eta_{T,\infty}$  as a function of  $\eta_{T',\infty}$ , we can insert it in Eq. (4.5) to obtain

$$\ln \left[ 1 - \alpha (\eta_{T',\infty})^{T/T'} - \eta_{T',\infty} \right] = \frac{1}{q_{T'}} \ln \left[ \frac{c \eta_{T',\infty}}{q_{T'}} \right] + \ln \left[ \frac{c_{*,T'}}{c} \right], \quad (4.8)$$

for which we have not been able to find an exact analytical solution. However, if  $\eta_{T',\infty}$  is not exceedingly small, the first term on the right-hand side of the equation is much smaller than the second, and we can write

$$1 - \alpha (\eta_{T',\infty})^{T/T'} - \eta_{T',\infty} = \left( \frac{c_{*,T'}}{c} \right). \quad (4.9)$$

This equation can be solved analytically for some values of the ratio  $T'/T$ . For instance, for the competition between  $T = 1$  and  $T = 3$  capsids, we can write Eq. (4.9) as a cubic equation for the quantity  $\eta_{3,\infty}^3$ . Instead of presenting the lengthy expressions, we here focus on the limiting behavior of Eq. (4.9) to extract useful information.

Equation (4.9) reveals that if  $\eta_{3,\infty} \gg \alpha^{3/2}$ , we have  $\eta_{3,\infty} \sim 1 - (c_{*,3}/c)$  provided that  $c \gtrsim c_{*,3}$ , and if  $c \lesssim c_{*,3}$  we must have  $\eta_{3,\infty} \approx 0$ . Interestingly, for the case in which  $\eta_{3,\infty} \ll \alpha^{2/3}$ , we find that  $\eta_{3,\infty}$  once more becomes very small. In that case we again retrieve Eq. (4.9) from Eq. (4.8), except that  $c_{*,3}$  will be replaced by  $c_{*,1}$ , leading to the asymptotic relationship  $\eta_{1,\infty} \sim 1 - (c_{*,1}/c)$  for  $c \gtrsim c_{*,1}$ , while for  $c \lesssim c_{*,1}$  we obtain  $\eta_{1,\infty} \approx 0$ .

In conclusion, if  $c_{*,3} \ll c_{*,1}$  and  $c \lesssim c_{*,3}$ , almost no capsids form. However, for  $c \gtrsim c_{*,3}$  capsids do form, but they are mostly  $T = 3$  structures, even if  $c \gtrsim c_{*,1}$ . If the coat protein concentration is sufficiently large and  $c_{*,1} \approx c_{*,3}$ , both species form in appreciable quantities. Notice that for  $c_{*,1} \approx c_{*,3}$  to hold, the difference in binding free energies of the two species must be much smaller than unity,  $|\Delta g| = |g_3 - g_1| \ll 1$ . As the binding free energies tend to be in the range from 10 to 20 in units of thermal energy, very small differences in binding free energy are required to see co-existence between different  $T$  numbers under conditions of thermodynamic equilibrium.

Figures 4.2 and 4.3 illustrate the competition between the two capsid sizes as a function of the binding free energies  $g_1$ ,  $g_3$  and  $\Delta g$  at a coat protein concentration (mole fraction) of  $c = 2 \cdot 10^{-5}$ . The coat proteins are presumed to be dimeric, mimicking the experiments of Timmermans *et al.* performed with the modified CCMV coat proteins [134]. To this end, we set  $q_1 = 30$  and  $q_3 = 90$ . For the given concentration of coat protein, we expect capsids to disappear from solution if  $g_1$  and  $g_3$  are greater than approximately  $\ln 2 \cdot 10^{-5} \simeq -11$ , as is confirmed by Fig. 4.2. According to Eq. (4.6), the crossover from the  $T = 1$  to  $T = 3$  dominated regimes occurs for  $\eta_{1,\infty} = \eta_{3,\infty} = 1/2 = \alpha^{3/2}$ . This translates to a difference between the binding free energies of  $\Delta g = g_3 - g_1 \simeq -0.3$ . The lack of crossover for  $\Delta g = 0$  is due to the impact of entropy, which favors smaller capsids. Figure 4.3 confirms this fact, and shows  $\eta_{1,\infty}$  and  $\eta_{3,\infty}$  as a function of  $\Delta g$  for different values of  $g_1 = -14, -11, -10.4, -9$ . We expect little assembly for  $g_1 \gtrsim -10$  because the concentration then drops below the corresponding critical concentration. The figure confirms this trend for both  $T$  numbers.

### 4.3 Kinetics of $T$ -number conversion

Having obtained a clear understanding of the thermodynamics of mixtures of differently sized capsids, we now set up a theory that aims to describe the time evolution of the solution composition following a quench. Since we are interested in the deterministic time evolution of the conversion between capsid species, we write the corresponding kinetic equations in terms of what is known as Model A relaxational kinetics, following our earlier

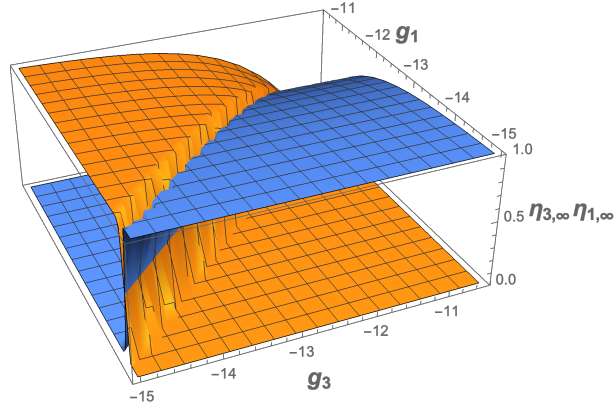


Figure 4.2: The equilibrium fraction of proteins in  $T = 1$  capsids,  $\eta_1$ , and in  $T = 3$  capsids,  $\eta_3$ , as a function of the binding free energies of the two structures,  $g_1$  and  $g_3$  (see Eqs. 4.6 and 4.8). The orange surface shows  $\eta_3$  and the blue surface shows  $\eta_1$ . The dimensionless overall protein concentration was set at  $c = 2 \cdot 10^{-5}$ , and the aggregation numbers for the two species set to values of  $q_1 = 30$  and  $q_3 = 90$  implying that the protein subunits are dimers of the coat protein. See also the main text.

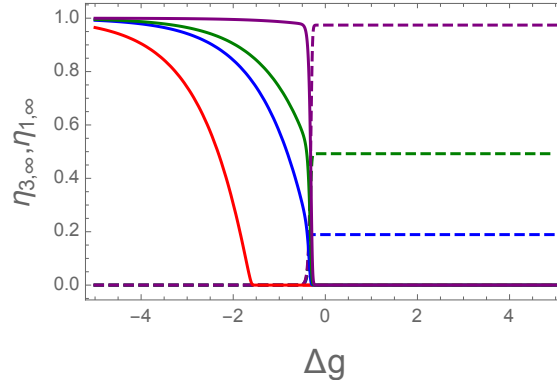


Figure 4.3: The equilibrium fraction of protein in  $T = 3$  capsids,  $\eta_3 = \eta_{3,\infty}$  (solid lines), and  $T = 1$  capsids,  $\eta_1 = \eta_{1,\infty}$  (dashed lines), as a function of the difference in the dimensionless binding free energies  $\Delta g \equiv g_3 - g_1$ . Shown are results for different values of  $g_1$ , indicated by different colors, with purple for  $g_1 = -14$ , green for  $g_1 = -11$ , blue for  $g_1 = -10.4$ , and red for  $g_1 = -9$ . The dimensionless overall protein concentration was set at  $c = 2 \cdot 10^{-5}$ , and the aggregation numbers set equal to  $q_1 = 30$  and  $q_3 = 90$  implying that the subunits are dimers of the coat proteins. Note that the transition does not occur at  $\Delta g = 0$ . See also the main text.

work on single capsid species assembly and disassembly [137]. The governing equations are for the most general case, involving multiple species of capsids, given by

$$\frac{\partial \eta_T}{\partial t} = -\Gamma_T \frac{\partial f}{\partial \eta_T}, \quad (4.10)$$

where  $\Gamma_T$  are phenomenological rate constants associated with the various  $T$ -numbers. As the quench experiments are done at fixed concentration [134], we need not consider their dependence on the total concentration of coat proteins  $c$ . The possibility that the rate constants depend on the concentration of free monomers cannot be excluded, in particular the one for the species that assembles. We choose to ignore this and view the rate constants as adjustable parameters, as is usually done in this kind of dynamical model. Notice that because of the mass conservation  $\eta_s = 1 - \sum_T \eta_T$ , the time evolution of the free monomers in solutions  $\partial \eta_s / \partial t = -\sum_T \partial \eta_T / \partial t$  can be easily obtained.

Investigating the conversion between two capsid species, we focus specifically on the conversion between  $T = 1$  and  $T = 3$  capsids. By inserting our free energy, Eq. (4.1), into the kinetic Eq. (4.10) for  $T = 1$  and  $T = 3$ , and making use of the equations of state for the two species of capsid, Eqs. (4.4) and (4.5), we obtain

$$\frac{\partial \eta_1}{\partial \tau} = \ln \left( \frac{1 - \eta_1 - \eta_3}{1 - \eta_{1,\infty} - \eta_{3,\infty}} \right) - \frac{1}{q_1} \ln \frac{\eta_1}{\eta_{1,\infty}}, \quad (4.11)$$

$$\frac{\partial \eta_3}{\partial \tau} = \Gamma \left[ \ln \left( \frac{1 - \eta_1 - \eta_3}{1 - \eta_{1,\infty} - \eta_{3,\infty}} \right) - \frac{1}{q_3} \ln \frac{\eta_3}{\eta_{3,\infty}} \right]. \quad (4.12)$$

Here, we have made the time  $t$  dimensionless by defining  $\tau \equiv \Gamma_1 t$ , and introduced the kinetic parameter  $\Gamma \equiv \Gamma_3 / \Gamma_1$  that depends on the relative rates of assembly and disassembly of

the  $T = 3$  and  $T = 1$  capsids. As before,  $\eta_{T,\infty}$  denotes the fraction of coat proteins in each species under conditions of thermodynamic equilibrium after the quench, as time goes to  $\tau \rightarrow \infty$  (hence the subscript  $\infty$ ).

While we have not been able to solve these coupled differential equations exactly, approximate analytical solutions can be found in certain experimentally relevant limits. For instance, for shallow quenches or the late stages of the conversion for deep quenches, we can set  $\eta_T(\tau) = \eta_{T,\infty}(1 + \delta_T(\tau))$  where  $|\delta_T(\tau)| \ll 1$ . Inserting this into Eqs. (4.11) and (4.12), Taylor expanding these in terms of  $|\delta_T(\tau)|$  gives rise to a set of linear equations that can be diagonalized. We refer to the Appendix .6 for details. The two fundamental relaxation rates  $\lambda_{\pm}$  obtained through solving the coupled equations are complicated functions of the aggregation numbers and the equilibrium values of the fraction of proteins in the two species. We here only quote their approximate values:

$$\lambda_+ \sim \frac{1 + \Gamma}{\eta_{s,\infty}} + \dots, \quad (4.13)$$

where  $\eta_{s,\infty} = 1 - \eta_{1,\infty} - \eta_{3,\infty}$  is the fraction of coat proteins in free solution, and

$$\lambda_- \sim \frac{\Gamma}{1 + \Gamma} \left[ \frac{1}{\eta_{1,\infty} q_1} + \frac{1}{\eta_{3,\infty} q_3} \right] + \dots \quad (4.14)$$

to leading order in powers of  $1/\eta_{1,\infty} q_1 \ll 1$  and  $1/\eta_{3,\infty} q_3 \ll 1$ . Notice that in the limits  $\Gamma \rightarrow 0$  and  $\Gamma \rightarrow \infty$  one relaxation becomes infinitely faster than the other, as one would expect. Figure 4.4, showing the numerically obtained values for the case  $q_3 = 3q_1 \gg 1$  confirms this.

It appears that one of the relaxation rates,  $\lambda_+$ , depends only on the final total amount of assembled material, or, equivalently, on the fraction of free monomers, not on how the material is distributed over the two competing capsid species. This suggests that this rate describes the response of the free monomers. The other rate,  $\lambda_- \leq \lambda_+$ , does depend on the final distribution over the two capsid species and is not symmetrical with respect to their fractions. It is tempting to assign this rate to the late-stage equilibration involving mainly the two types of capsid and less so that of the free protein subunits.

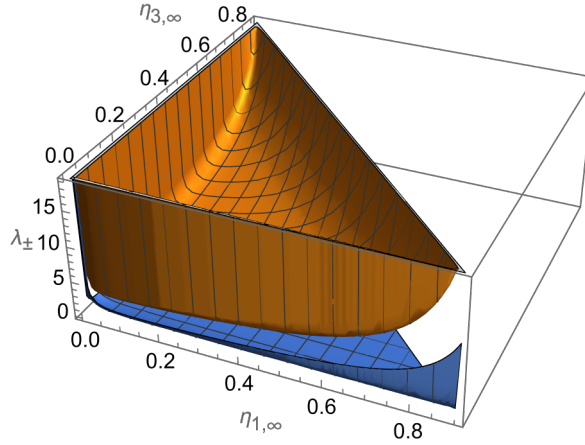


Figure 4.4: Dimensionless fundamental relaxation rates  $\lambda_{\pm}$  of the linearized kinetic equations (4.11) and (4.12) describing the conversion between  $T = 1$  and  $T = 3$  capsids as a function of the fraction of  $T = 3$  capsids  $\eta_3$  and kinetic coefficient  $\Gamma = 1$ . The blue surface shows  $\lambda_-$  and the orange one  $\lambda_+$ . We set  $q_3 = 3q_1 = 90$  to model CCMV capsid coat proteins that are present in solution as dimers.

We believe that this explains most of our numerical results discussed in more detail in the next section, namely that the fraction of proteins in monomers relaxes relatively fast to its final value, after which the assembly of one type of capsid becomes enslaved by the disassembly of the other. Naïvely, this would suggest that in that case we can ignore the first term on the right-hand side of Eqs. (4.11) and (4.12), making the kinetic equations amenable

to analytical solution [137]. However, these solutions cannot be correct, because then  $\eta_1$  and  $\eta_3$  would evolve independently from each other. Indeed, these solutions violate the equality  $\partial\eta_1/\partial\tau = -\partial\eta_3/\partial\tau$  that holds if the concentration of free subunits  $\eta_s = 1 - \eta_1 - \eta_3$  was constant.

For initial conditions where  $\eta_T(0)/\eta_{T,\infty}$  are not very large or very small and for sufficiently short times  $\tau \ll \tau_- \equiv \lambda_-^{-1}$ , we are however able to find an analytical solution for the fraction of proteins in free solution  $\eta_s = 1 - \eta_1 - \eta_3$ . For this, we first ignore the last terms in eqs. (4.11) and (4.12), and obtain  $\partial\eta_1/\partial\tau = \Gamma^{-1}\partial\eta_3/\partial\tau = \ln(\eta_s(\tau)/\eta_{s,\infty})$ . Subsequently combining these two equations gives a dynamical equation for  $\eta_s$  that can be solved exactly to give

$$\left(\frac{1+\Gamma}{\eta_{s,\infty}}\right)\tau = \lambda_+\tau = \text{li}\left[\frac{\eta_s(0)}{\eta_{s,\infty}}\right] - \text{li}\left[\frac{\eta_s(\tau)}{\eta_{s,\infty}}\right], \quad (4.15)$$

where  $\text{li}[x] = \int_0^x dy(1/\ln y)$  is the logarithmic integral. For the first equality we used the identity given in eq. (4.13). This confirms that  $\lambda_+$  must indeed be the relaxation rate associated with the early-stage kinetics dominated by the free monomers and one of the capsid species, in particular if  $\Gamma \gg 1$  or  $\Gamma \ll 1$ .

Consequently, the initial response to the quench must be driven primarily by the translational entropy of the free subunits and the binding free energy of the capsid species. In contrast, the late-stage relaxation, in which there are protein exchanges between the two types of capsids, is basically driven by differences in the binding free energies of the proteins in these two species. Our numerical results, discussed in the next section, confirm this picture albeit with notable exceptions.

# Chapter 5

## Results

### 5.1 Numerical results

We solved the coupled differential equations (4.11) and (4.12) numerically using the SciPy library `scipy.integrate` [141], investigating the interconversion of  $T = 1$  and  $T = 3$  capsids. We systematically varied all input parameters, that is, (i) the starting compositions  $\eta_1(0)$  and  $\eta_3(0)$ , (ii) the final compositions  $\eta_{1,\infty}$  and  $\eta_{3,\infty}$ , and (iii) the ratio of assembly rates  $\Gamma$ , taking as representative values 0.1, 1, and 10. To select the appropriate time interval  $d\tau$  for our numerical studies, we demand that the concentration changes after each time step should be less than 1%. If the concentration change exceeds 1%, we decrease the time interval. Our results turn out to become invariant of the time interval step for  $d\tau < 10^{-3}$  for all cases investigated. For our discussion below, we set its value at  $d\tau = 10^{-4}$ .

We focus in this section on three interesting types of numerical experiments: (i) one starting with a large fraction of proteins equally distributed in both capsids and ending with a large fraction of proteins only in one of the capsids (see Fig. 5.1); (ii) one where the

initial state is one with almost no capsids present in solution, but where most proteins are in capsids in the final (equilibrium) state (Fig. 5.2); (iii) one starting with a large fraction of proteins only in one of the capsids and ending with a large fraction of proteins in the other capsid (Fig. 5.3). We discuss these three general classes using representative examples.

Figure 5.1 shows the time evolution of the various species present in the solution from the initial conditions  $\eta_1(0) = \eta_3(0) = 0.40$  to the final states  $\eta_{1,\infty} = 0.80$  and  $\eta_{3,\infty} = 0.18$ . So, we start off with equal amounts of 40% coat proteins in  $T = 1$  and in  $T = 3$  capsids, and 20% in free solution, ending in much more protein in  $T = 1$  than in  $T = 3$ , that is, 80% *vs* 18%, and almost no free protein. Independent of the rate  $\Gamma$  that defines how swiftly the material in  $T = 3$  capsids responds to changes in the thermodynamic conditions relative to that in  $T = 1$  capsids, the fraction of free monomers indicated by the green curves in Fig. 5.1 decreases monotonically to reach its final steady-state value well before the proteins in capsids have reached a steady state at longer times. We observed this behavior for over 100 cases that we have investigated. This also seems to be consistent with the outcome of the experiments of Timmermans *et al.*, who also observe a nearly constant monomer fraction from the earliest time they were able to do the measurements [134]. See also the next section.

If  $\Gamma = 0.1$ , the response of the fraction of proteins in  $T = 3$  capsids is relatively slow, while for  $\Gamma = 10$  it is fast. This means that if  $\Gamma = 0.1$ , the  $T = 1$  capsids, which are thermodynamically more stable than the  $T = 3$  capsids, quickly absorb monomers from solution to increase their number, whilst the  $T = 3$  capsids do not disassemble yet on account of their slow dynamics. This is what the dotted red and blue curves in Fig. 5.1

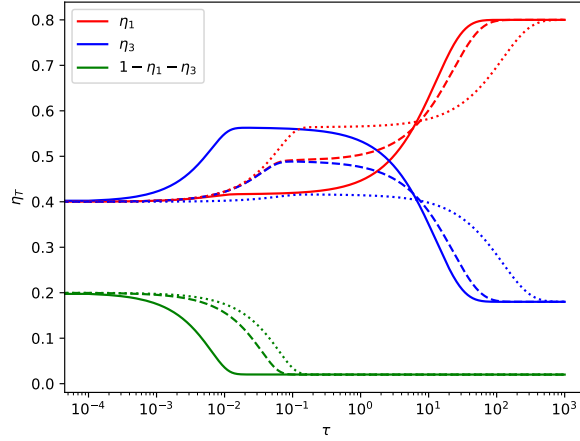


Figure 5.1: Time evolution of the fraction of coat proteins  $\eta_T$  in capsids with triangulation numbers  $T = 1$  (red) and  $T = 3$  (blue), as well as the fraction in monomers  $1 - \eta_1 - \eta_3$  (green), as a function of dimensionless time  $\tau$ . Indicated are results for different values of the ratio of assembly rates  $\Gamma = 10$  (solid),  $\Gamma = 1$  (dashed), and  $\Gamma = 0.1$  (dotted). The initial conditions are  $\eta_1(0) = \eta_3(0) = 0.40$  and the final states are  $\eta_{1,\infty} = 0.80$  and  $\eta_{3,\infty} = 0.18$ . We set  $q_3 = 3q_1 = 90$  presuming the coat proteins to form dimers. See also the main text.

indicate. The figure also reveals that at much later time, after  $\eta_1$  having reached a pseudo plateau,  $T = 3$  shells start to disassemble in order to form additional  $T = 1$  shells at a more or less constant fraction of free coat proteins in solution. So, for this small value of  $\Gamma$  the conversion of  $T = 3$  into  $T = 1$  capsids happens in two steps, first involving the formation of  $T = 1$  capsids using free monomers, and subsequently  $T = 1$  capsids forms upon the disassembly of  $T = 3$  capsids.

Something similar happens for  $\Gamma = 10$ , shown in Fig. 5.1 by the solid curves, but now reversed. In this case, even though the  $T = 3$  shell is less stable than the  $T = 1$  shell, both capsids are more stable than free monomers are. Thus, in the beginning,  $T = 3$  shells start to assemble thereby depleting the free monomers from solution. Next,  $\eta_3$  reaches a pseudo plateau, where it remains constant for quite some time, after which the  $T = 3$  shells

disassemble in favor of the  $T = 1$  shells that in the end are more thermodynamically stable. This happens at a more or less constant free monomer concentration. In this case, the fraction of  $T = 3$  capsids first increases from its initial value and then decreases to a value lower than the initial value. Our results for  $\Gamma = 1$  are similar to those for  $\Gamma = 10$ , except that the overshoot of  $\eta_3$  is much smaller and happens much later.

A careful analysis of Fig. 5.1 thus reveals that there must be two time scales involved, not just in the linear response discussed in the preceding section, see Eqs. (4.13) and (4.14), but also in the full, non-linear response of the system of coat proteins and capsid shells to a quench. If we translate the relaxation rates  $\lambda_{\pm}$  of Eqs. (4.13) and (4.14), obtained from a linear response analysis, to relaxation times  $\tau_{\pm} \equiv \lambda_{\pm}^{-1}$ , then we find  $\tau_+ \simeq 0.018$  and  $\tau_- \simeq 110$  for  $\Gamma = 0.1$ , and  $\tau_+ \simeq 0.0018$  and  $\tau_- \simeq 11$  for  $\Gamma = 10$ . This roughly matches the time scales of the two processes as may be verified in Fig. 5.1.

The picture that emerges remains valid even if we start off from mostly free monomers, as is illustrated in Fig. 5.2. Here, we monitor the time evolution of the various species present in the solution from the initial conditions  $\eta_1(0) = \eta_3(0) = 0.001$  to the final states  $\eta_{1,\infty} = 0.001$  and  $\eta_{3,\infty} = 0.80$ . So, we initiate the assembly with equal amounts of 0.1% coat protein in  $T = 1$  and  $T = 3$  capsids, and 99.8% in free solution, ending in much more protein in  $T = 3$  than in  $T = 1$  with 80% *vs* 0.1%, and 19.9% free protein.

We note that if  $\Gamma = 0.1$  the response of the fraction of proteins in  $T = 3$  shells is relatively slow, while for  $\Gamma = 10$  it is fast. Hence, if  $\Gamma = 0.1$ ,  $T = 1$  capsids swiftly assemble by absorbing free monomers from solution even though the  $T = 3$  shells are the more stable of the two. The thermodynamic stability of the  $T = 1$  capsids exceeds that of the free

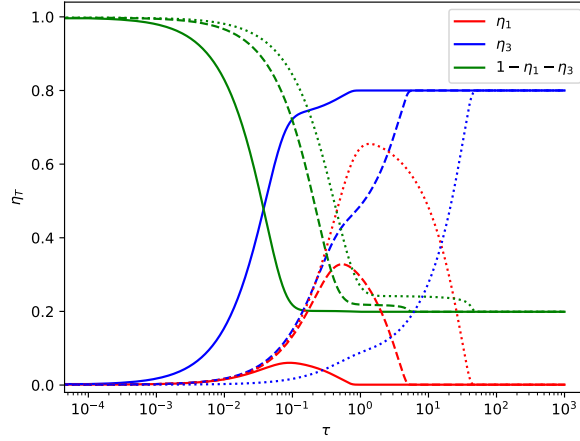


Figure 5.2: Time evolution of the fraction of coat proteins  $\eta_T$  in capsids with triangulation numbers  $T = 1$  (red) and  $T = 3$  (blue), as well as the fraction in monomers  $1 - \eta_1 - \eta_3$  (green), as a function of dimensionless time  $\tau$ . Indicated are results for different values of the ratio of assembly rates  $\Gamma = 10$  (solid),  $\Gamma = 1$  (dashed), and  $\Gamma = 0.1$  (dotted). The initial conditions are  $\eta_1(0) = \eta_3(0) = 0.001$  and the final states are  $\eta_{1,\infty} = 0.001$  and  $\eta_{3,\infty} = 0.80$ . We set  $q_3 = 3q_1 = 90$  presuming the coat proteins to form dimers. See also the main text.

monomers, driving the assembly of the metastable species. As the dotted line in Fig. 5.2 shows, after some time these particles disassemble again in favor of the  $T = 3$  shells. This happens at a more or less constant concentration of free monomers. Again we see that the competition in time involves two species only: first the proteins in  $T = 1$  capsids and in free solution respond to the quench, and after that the protein subunits in  $T = 1$  and  $T = 3$  shells readjust to reach a state of thermodynamic equilibrium.

It transpires that for the given conditions,  $T = 1$  shells appear only temporarily. The larger the value of  $\Gamma$ , the less pronounced this effect is. The appearance and disappearance of the smaller species produces a shoulder and a pseudo plateau in the fraction of protein in the larger species, not dissimilar to what we saw in Fig. 5.1. Again, two time scales appear that we associate with the elementary rates  $\lambda_{\pm}$ . Translated to relaxation

times, we obtain  $\tau_+ \simeq 0.026$  and  $\tau_- \simeq 12$  for  $\Gamma = 0.1$  and  $\tau_+ \simeq 0.012$  and  $\tau_- \simeq 0.25$  for  $\Gamma = 10$ . This roughly matches the time scales of the two processes, as revealed in Fig. 5.2. Note that to obtain these numbers, we used the full expression given in Eq. (.48) in appendix A rather than the asymptotic Eqs. (13) and (14) as  $\eta_{1,\infty}q_1$  is not large enough for these asymptotic expressions to hold.

The final case that we discuss is that where  $\eta_1(0) = 0.2$  and  $\eta_3(0) = 0.6$ , and  $\eta_{1,\infty} = 0.6$  and  $\eta_{3,\infty} = 0.2$ . So, we are deeply in the polymerized regime, with 80% of monomers in capsids: 60% in  $T = 3$  shells and 20% in  $T = 1$  shells at time zero. In thermal equilibrium, these numbers are reversed but their total fraction remains the same. This turns out a special case. Figure 5.3 reveals that, even though the starting and ending fractions of free monomers are the same, the conversion of  $T = 3$  into  $T = 1$  capsids occurs at *approximately* constant free monomer fraction. For  $\Gamma = 10$  there is a slight overshoot (solid line), whilst for  $\Gamma = 1$  and  $\Gamma = 0.1$  there is a slight undershoot (dashed and dotted lines). The over- and undershoots are very small indeed, at most a few per cent.

Again there are two time scales, one of which signifies the onset of the very small over- or undershoot of the free monomers. This happens well before the fraction of protein in capsids responds significantly. The second (much larger larger) time scale is associated with the conversion between the large and smaller species of capsid, *and* with the relaxation of the monomer concentration back to its equilibrium value. The corresponding relaxation times we obtain from the rates of Eqs. (13) and (14) are  $\tau_+ \simeq 0.18$  and  $\tau_- \simeq 100$  for  $\Gamma = 0.1$  and  $\tau_+ \simeq 0.018$  and  $\tau_- \simeq 10$  for  $\Gamma = 10$ . These numbers agree again approximately with what is shown in Figure 5.3 and in Fig. 5.4, where we zoom in on the time evolution of the

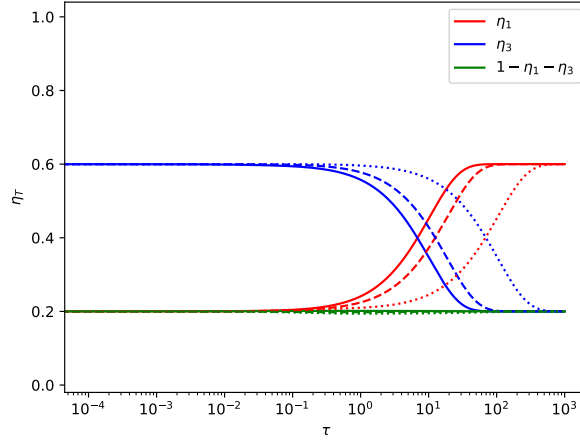


Figure 5.3: Time evolution of the fraction of coat proteins  $\eta_T$  in capsids with triangulation numbers  $T = 1$  (red) and  $T = 3$  (blue), as well as the fraction in monomers  $1 - \eta_1 - \eta_3$  (green), as a function of dimensionless time  $\tau$ . Indicated are results for different values of the ratio of assembly rates  $\Gamma = 10$  (solid),  $\Gamma = 1$  (dashed), and  $\Gamma = 0.1$  (dotted). The initial conditions are  $\eta_1(0) = 0.2$  and  $\eta_3(0) = 0.6$  and the final states are  $\eta_{1,\infty} = 0.6$  and  $\eta_{3,\infty} = 0.2$ . We set  $q_3 = 3q_1 = 90$  presuming the coat proteins to form dimers. See also the main text.

fraction of free monomers. The latter figure also points at the existence of relatively long-lived pseudo plateaus characterized by out-of-equilibrium concentrations of free monomers.

The question arises, what happens if we swap the initial and final fractions for the case shown in Fig. 5.3. We expect from the fundamental relaxation times  $\tau_{\pm}$  this situation to be quite different:  $\tau_+$  does not change since the fraction of free protein does not change, but the second time scale changes considerably to  $\tau_- = 60$  for  $\Gamma = 0.1$  and  $\tau_- = 6.0$  for  $\Gamma = 10$  compared to  $\tau_- \simeq 100$  and  $\tau_- \simeq 10$ , respectively. So, the dynamics does change and cannot be compensated for by simply taking the reciprocal value of  $\Gamma$ . See also Fig. 5.4, showing the time evolution of the fraction of monomer units in free solution for the  $T = 1 \rightarrow T = 3$  (green lines) and  $T = 3 \rightarrow T = 1$  (black lines) conversions. This makes the assembly and disassembly dynamics fundamentally asymmetric, which is also the case for that of a

single species [137]. The effect is not very pronounced, though, as already mentioned and as a comparison of the different curves in Fig. 5.4 shows. The most remarkable difference between the cases  $T = 1 \rightarrow T = 3$  (green lines) and  $T = 3 \rightarrow T = 1$  (black lines) is in the over- and undershoots, which are reversed for corresponding values of  $\Gamma$ .

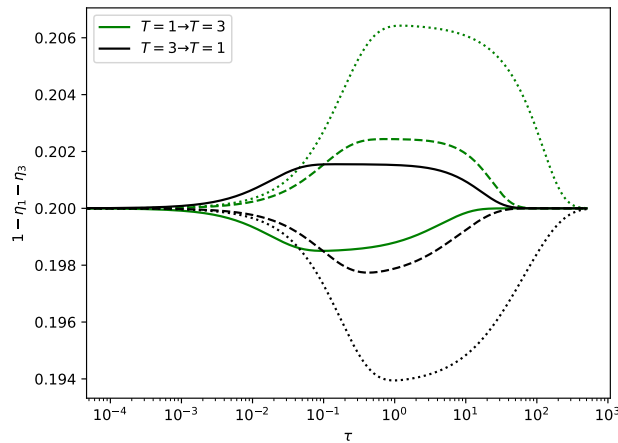


Figure 5.4: Time evolution of the fraction of monomers  $1 - \eta_1 - \eta_3$ , as a function of dimensionless time  $\tau$ . Indicated are results for different values of the ratio of assembly rates  $\Gamma = 10$  (solid),  $\Gamma = 1$  (dashed), and  $\Gamma = 0.1$  (dotted). The initial conditions for  $T = 3 \rightarrow T = 1$  (black) are  $\eta_1(0) = 0.2$  and  $\eta_3(0) = 0.6$  with final states  $\eta_{1,\infty} = 0.6$  and  $\eta_{3,\infty} = 0.2$ . For the  $T = 1 \rightarrow T = 3$  (green) we swap the initial and final conditions of  $T = 3 \rightarrow T = 1$ . We set  $q_3 = 3q_1 = 90$  presuming the coat proteins to form dimers. See also the main text.

This ends our discussion of the numerical evaluation of the dynamical equations.

We next apply the theory in order to describe the experiments of Timmermans *et al.* [134].

## 5.2 Comparison with Experiment

In the experiments of Timmermans *et al.*, aqueous solutions containing CCMV coat proteins functionalized with a hydrophobic elastin-like polypeptide form  $T = 3$  capsids

at pH equal to 5 and ionic strength of 0.5 M whilst at a pH of 7.5 and ionic strength of 0.1 M, they assemble into the smaller  $T = 1$  capsids [134]. The sizes were established using a combination of size exclusion chromatography (SEC) and transmission electron microscopy. Changing (by means of a dialysis step) the acidity and ionic strength from pH 7.5 and 0.1 M to pH 5 and 0.5 M leads to the slow conversion of smaller capsids into larger ones, as is evidenced by SEC. Conversely, SEC also shows that changing the acidity from pH 5 to pH 7.5 and the ionic strength from 0.5 M to 0.1 M leads to the conversion of the larger into the smaller species. Since partial capsids are neither observed in the SEC traces nor in the electron micrographs, the conclusion is that the unstable species disassembles into protein subunits (dimers) that reassemble into the stable species.

Both types of conversions are exceedingly slow to complete. Starting off from 100%  $T = 3$  capsids, after 168 hours only 70% of  $T = 1$  capsids are produced, indicating the conversion has not yet completed at that time. One final data point at 1608 hours shows 92%  $T = 1$  capsids. The initial response to the change in solution conditions is relatively swift; however, after about 2 hours, the rate of conversion slows down considerably. Something rather similar happens in the  $T = 1 \rightarrow 3$  conversion experiments, starting off at 100%  $T = 1$ , the process slows down after about 24 hours. After 168 hours the conversion is only 60% complete. The final data point at 1440 hours shows 98% conversion. In the absence of data between 168 and the final measurements at 1608 and 1440 hours for the two types of experiment, we cannot be certain how long the conversion between species actually takes even if we treat the last points (both taken after about two months) as essentially complete.

Although our model produces a short and a long timescale, mimicking what Timmermans *et al.* observe experimentally, we have not been able to accurately describe the conversion for times below 168 hours and get a complete or near-complete conversion after two months. In this respect, our model is lacking compared to the classical nucleation theory [134], which nicely describes the experiments. However, if we take the data up to 168 hours at face value, assuming that the system has reached the steady state and ignore the full conversion that happens between 168 hours and two months, we can describe the experimental data rather well.

To fit our model to the experimental data of Timmermans *et al.*, [134] we minimize the sum of the cost functions or, equivalently, maximize the coefficient of determination  $r^2$ , between the numerical solutions to our coupled equations and the experimental observations for each species. We define the cost function as  $\Sigma(\eta_{\text{theo}} - \eta_{\text{exp}})^2 / \Sigma(\eta_{\text{exp}} - \bar{\eta}_{\text{exp}})^2 = 1 - r^2$ , where the sum is over all data points for each species,  $\eta_{\text{theo}}$  are the fitted values obtained from the theory,  $\eta_{\text{exp}}$  are the experimental data, and  $\bar{\eta}_{\text{exp}} = \Sigma\eta_{\text{exp}}/N$  where the sum is again over all data points over each species with  $N = 20$  the number of experimental data points for each conversion experiment. Note that we calculate  $r_1^2$  for the conversion of  $T = 1$  to  $T = 3$  and  $r_3^2$  for the conversion of  $T = 3$  to  $T = 1$ . We then maximize the average value of  $(r_1^2 + r_3^2)/2$ . The optimization is accomplished by implementing a hyperparameter optimization method of the grid search variant. [82]

The values for  $\Gamma_1$  and  $\Gamma$  follow from the hyperparameter optimization and the subsequent model fitting. In order to do the model fitting, we took the initial conditions to be the average of the experimental measurements for the  $T = 1$  and  $T = 3$  species. We ran a

grid search for the equilibrium conditions and their corresponding rate constants [142]. The search for  $\eta_{1,\infty}$  and  $\eta_{3,\infty}$  spanned from the smallest to largest species fraction measurements. More specifically, we set one limit of the search to be  $\eta_T(0)$  and the other limit to be  $\eta_T(30\text{hr})$ . We then partitioned this so that the step is 0.01. The value of  $\eta_{T,\infty}$  was chosen in between the range of experimental data. The rate constants  $\Gamma_1$  and  $\Gamma$  were determined by an extensive search of possible values. When determining the cost function, we first scaled the time axis such that  $t\Gamma_1 = \tau$  and then found  $\Gamma$  in order to numerically solve Eqs. (4.11) and (4.12). To convert back to experimental time, we take  $t = \tau/\Gamma_1$ .

In our curve-fitting procedure, we take the initial and final fractions to match the values experimentally observed in the time frame from 0 to 168 hours, and optimize the phenomenological rate constant ratio  $\Gamma$ . It is important to point out that the actual zero time in the experiments is not known accurately on account of the experimental procedure that involves a dialysis step. We refer to the original publication of Timmermans *et al.* for experimental details [134]. The SEC data are consistent with the presence of a fraction of small protein subunits, identified as coat protein dimers, two larger species of particle associated with the  $T = 1$  and  $T = 3$  capsids, and much larger particles that could be aggregates of (incomplete) capsids or protein subunits. The fraction of protein aggregates remains practically constant over the course of time, as does the fraction of free subunits. We count the material in aggregates as part of the fraction of subunits. We do not expect this to significantly affect the numbers of capsids in view of the long timescales involved in assembly and disassembly. Hence, we take the SEC data at face value.

Figure 5.5 shows the results of the combined sets of experiments for the conversion of  $T = 1$  to  $T = 3$  particles. Also indicated are our model fits (solid lines) to the indicated experimental data (symbols). To obtain the curve fits, we set the initial fractions at  $\eta_1(0) = 0.86$  and  $\eta_3(0) = 0.02$ , and the equilibrium fractions at  $\eta_{1,\infty} = 0.42$  and  $\eta_{3,\infty} = 0.44$ . From the latter, and using Eq. (4.3), we conclude that the binding free energies must be equal to  $g_1 \approx -11.4$  and is  $g_3 \approx -11.7$  indicating  $\Delta g = -0.3$ . The curve fitting produces an optimal ratio of rate constants  $\Gamma = \Gamma_3/\Gamma_1 = 23.5$  where the corresponding rate constant for the  $T = 1$  species  $\Gamma_1$  is  $1.0 \text{ hrs}^{-1}$ , using a time step of  $dt = 0.0001 \text{ hrs}$ . Agreement between theory and experiment is fair with an  $r^2$  value of 0.884, where we observe that the agreement is less accurate in the later stages compared to the initial stages. The theory appears to overlook the slight increase in free protein subunit concentration that occurs in the later stages of the process. On the other hand, the scatter in the data is quite large and the two experimental data sets shown only agree approximately with each other.

Figure 5.6 shows the results of the quench experiments, which began with a solution primarily containing  $T = 3$  particles and progressed to conditions where the most dominant species is the  $T = 1$  ones. Again, the symbols indicate the two sets of experimental data and the solid lines the fits to the data. We set the initial fractions at  $\eta_1(0) = 0.01$  and  $\eta_3(0) = 0.72$ , and the equilibrium fractions at  $\eta_{1,\infty} = 0.50$  and  $\eta_{3,\infty} = 0.30$ . From the latter, we obtain for binding energies  $g_1 \approx -11.1$  and  $g_3 \approx -11.3$ , indicating that  $\Delta g = -0.2$ . We extract  $\Gamma = 0.60$  and  $\Gamma_1 = 15.2 \text{ hrs}^{-1}$ , using a time step  $d\tau = 0.0001 \text{ hrs}$ . The agreement between theory and experiment has significantly improved, with an  $r^2$  value of 0.909, even though the scatter in the data remains quite substantial. Notice that we do recover the

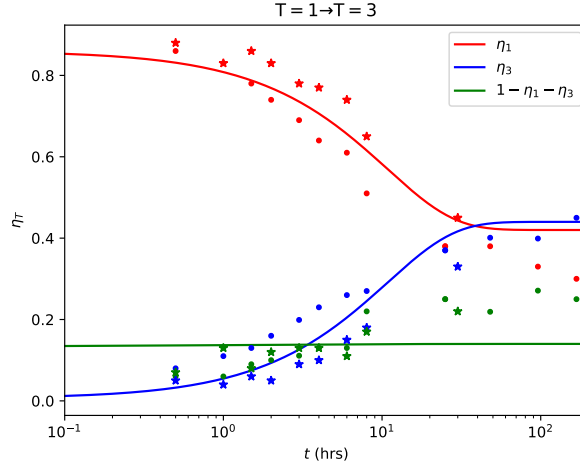


Figure 5.5: Fraction of protein in various species  $\eta_T$  as a function of time  $t$  in hours. Symbols: results from two data sets where following a quench  $T = 3$  capsids convert into  $T = 1$  capsids. Only the first 168 hours of the measurements of Timmermans *et al.* [134] are shown. The red, blue, and green lines indicate the fractions of  $T = 1$ ,  $T = 3$ , and free subunits. See also the main text.

virtually constant fraction of protein subunits. Table 5.1 shows the rate constants and binding free energies obtained from our data fitting analysis of the interconversion of  $T = 1$  and  $T = 3$ .

If we compare the binding free energies  $g_1$  and  $g_3$  that we obtain with those from the nucleation theory in Ref. [134], we find that our values are somewhat smaller in magnitude.

Conversion	$\Gamma_1$ [hrs] <sup>-1</sup>	$\Gamma_3$ [hrs] <sup>-1</sup>	$\Gamma$	$g_1$	$g_3$	$\Delta g$
$T = 1 \rightarrow T = 3$	1.0	23.5	23.5	-11.4	-11.7	-0.3
$T = 3 \rightarrow T = 1$	15.2	9.1	0.60	-11.1	-11.3	-0.2

Table 5.1: The numerical values of the model parameters obtained from fitting the relaxational model to the experimental data for the conversions of  $T = 1 \rightarrow T = 3$  and  $T = 3 \rightarrow T = 1$  capsids with at  $d\tau = 0.01$ .  $\Gamma_1$  and  $\Gamma_3$  are the relaxation rates associated with the assembly and disassembly of the  $T = 1$  and  $T = 3$  capsids, and  $\Gamma = \Gamma_3/\Gamma_1$  their ratio. The dimensionless free energies of binding of coat protein subunits are  $g_1$  and  $g_3$ , and  $\Delta g = g_3 - g_1$  their difference. See also the main text.

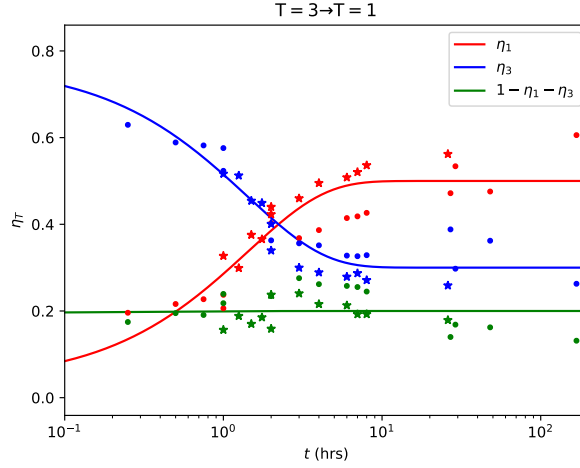


Figure 5.6: Fraction of protein in various species  $\eta_T$  as a function of time  $t$  in hours. Symbols: results from two data sets where following a quench  $T = 1$  capsids convert into  $T = 3$  capsids. Only the first 168 hours of the measurements of Timmermans *et al.* [134] are shown. The red, blue, and green lines indicate the fractions of  $T = 1$ ,  $T = 3$ , and free subunits. See also the main text.

The slightly less negative values that we find should not come as a complete surprise, as our analysis aimed to produce a pseudo-plateau for times approaching 168 hours, which we considered as equilibrium. In contrast, Timmermans *et al.* considered the fractions of the two capsid species after two months as equilibrium values, by which time the less stable species had largely disappeared from the solution.

We further conclude that for the  $T = 1 \rightarrow 3$  conversion experiments  $\Gamma_3 > \Gamma_1$ , while for the  $T = 3 \rightarrow 1$  conversion  $\Gamma_3 < \Gamma_1$ . So, for the former type of experiments, the relaxation rate associated with the  $T = 3$  particle is larger than that associated with the  $T = 1$  particle, and for the latter the reverse is the case. Since  $\Gamma_T$  is a phenomenological rate that somehow incorporates forward and backward rates, this finding is difficult to interpret. The fundamental relaxation time associated with the free monomers that can be deduced from Eq. (4.13), is just below 0.01 h (so less than one minute) for both types of

experiments, which explains why the prediction for the fraction of free monomer subunits remains constant on the time scale of the experiments.

Having completed our discussion of the comparison between theory and experiment, we next summarize our findings and discuss in greater detail the conditions under which our model is likely to be accurate or inaccurate.

## Chapter 6

# Conclusion

This thesis investigates three distinct yet interconnected projects, each contributing to our understanding of soft matter dynamics.

The first project examines tactoids, spindle-shaped droplets of uniaxial nematic phases coexisting with isotropic phases, as seen in various colloidal dispersions such as actin and fd virus. Recent experiments on tactoids of chitin nanocrystals in water show that electric fields can very strongly elongate tactoids, although the dielectric properties of the coexisting isotropic and nematic phases differ only slightly. However, this observation conflicts with the predictions of Monte Carlo simulations, which anticipate such extreme elongation, indicating that this is not the equilibrium state. We developed an equilibrium theory in which the bipolarity of the director field is allowed to freely adjust to minimize the combined elastic, surface, and Coulomb energies of the system. We explore the elongation and behavior of the director field in tactoids, considering factors such as tactoid size, electric field strength, surface tension, anchoring strength, elastic constants, and

anisotropy in electric susceptibility. The study finds that significant elongation occurs only if the director field is bipolar or quasi-bipolar and initially frozen.

In the second project, we developed a kinetic theory and proposed a relaxation model based on the Oseen-Frank free energy. The model employs two reaction coordinates to represent the director field and the elongation of the droplets, analyzing their time-dependent evolution after the application of an electric field. Depending on the relative magnitudes of the fundamental relaxation rates associated with these reaction coordinates, our findings reveal that the droplet aspect ratio can exhibit a significant and prolonged overshoot before eventually settling to its smaller equilibrium value. This delay in the director-field curvature response aligns with the observed experimental behavior. Overall, our theory provides a reasonable description of the experimental data.

The third project develops a kinetic model of virus capsid assembly and size interconversion, inspired by cowpea chlorotic mottle virus experiments. Using Model A kinetics, it describes two time scales of relaxation following environmental changes, which prompt reversible transitions between different capsid sizes. The model explains the intermediate and early conversion stages but highlights the need to incorporate nucleation barriers to fully capture the final equilibration stage of assembly.

Together, these projects advance models that deepen our understanding of complex soft matter behaviors, from tactoid formation to virus assembly.

# Chapter 7

## Appendix

### .1 Bipolar coordinate

In this section, we describe the bispherical coordinates used in the paper to define the structure of our tactoids [27, 29, 38, 60]. Bispherical coordinates are a three-dimensional orthogonal coordinate obtained by rotating the two-dimensional bipolar coordinate system about the axis that connects the two foci  $F_1$  and  $F_2$ , see Figs. 1-3 below. We note that there is more than one way to define bipolar coordinates. Within a bipolar coordinate system, every point  $P$  on a curve can be described by two parameters that we denote  $\tau$  and  $\eta$ . Here,  $\tau = \log(d_1/d_2)$  with  $d_1$  and  $d_2$  the distance from each focal point  $F_1$  and  $F_2$  to that point on the curve, see Fig. .1. As shown in the figure,  $\eta$  corresponds to the angle that sees these two focal points.

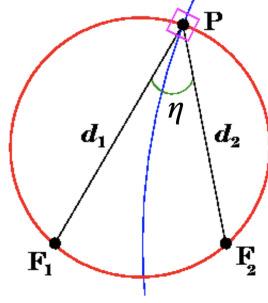


Figure .1: Parameters in bipolar coordinates: Each point  $P$  on a curve can be described by two parameters  $\tau$  and  $\eta$ . The angle  $\eta$  at point  $P$  sees the two foci while  $\tau$  is the logarithm of the ratio of distances to two fixed (focal) points. The values of  $\eta$  and  $\tau$  are constant on the red and blue circles, respectively. The three-dimensional bispherical coordinate can be obtained by rotating the bipolar coordinate around the axis connecting the two focal points  $F_1$  and  $F_2$ . The third coordinate in the bispherical coordinate is denoted by the azimuthal angle  $\phi$  not shown in the figure. Adopted from [61]

The element of a surface in bispherical coordinate can be written as  $dA = h_\eta h_\tau d\eta d\tau$ , where

$$h_\eta = h_\tau = \frac{a}{\cosh \tau - \cos \eta} \quad (.1)$$

with  $2a$  the distance between two focal points. The rest of this section focuses on the derivation of the metric given in Eq. .1.

We first find the relation between the bispherical and cylindrical coordinates based on Fig. .2. For simplicity, we assume a point on the curve in the  $\phi = 0$  plane and write,

$$\begin{aligned} d_2^2 &= (z - a)^2 + r^2, \\ d_1^2 &= (z + a)^2 + r^2. \end{aligned} \quad (.2)$$

To obtain  $z$  and  $r$  as a function of  $\tau$  and  $\eta$ , we set  $d_1 = d_2 e^\tau$  and find,

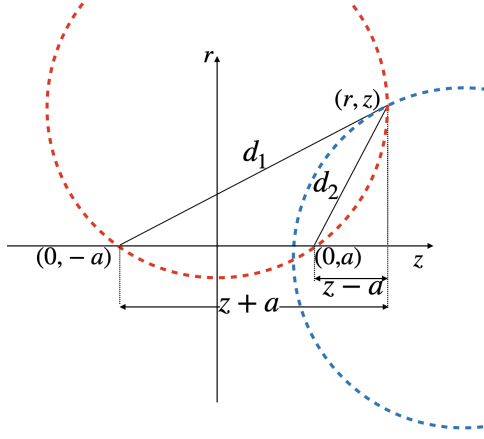


Figure .2: The relation between cylindrical coordinates and bispherical coordinates. For simplicity, we assume a point on the curve in the  $\phi = 0$  plane.

$$\begin{aligned}
 z &= \frac{a \sinh \tau}{\cosh \tau - \cos \eta}, \\
 r &= \frac{a \sin \eta}{\cosh \tau - \cos \eta}.
 \end{aligned}
 \tag{.3}$$

Since the azimuthal angle  $\phi$  is the same in both cylindrical and bispherical coordinates, we can easily obtain the relation between Cartesian and bispherical coordinates as follows,

$$\begin{cases}
 x = \frac{a \sin \eta \cos \phi}{\cosh \tau - \cos \eta} & 0 < \eta < \pi \\
 y = \frac{a \sin \eta \sin \phi}{\cosh \tau - \cos \eta} & -\infty < \tau < \infty \\
 z = \frac{a \sinh \tau}{\cosh \tau - \cos \eta} & 0 < \phi < 2\pi
 \end{cases}
 \tag{.4}$$

We note that the value of  $\tau$  is constant in blue circles shown in Fig .3.

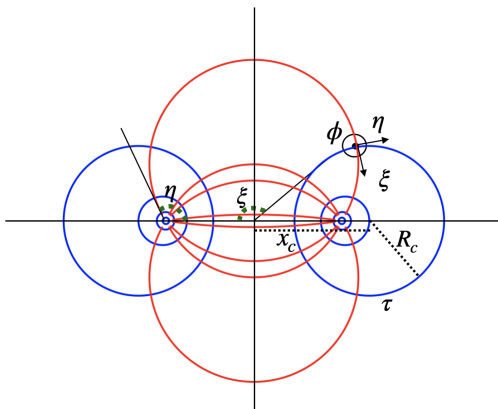


Figure .3: Both  $\xi$  and  $\tau$  along with  $\eta$  are constant values on blue circles and red arcs respectively.  $x_c$  is the  $x$ -component of the right larger blue circle from the origin and the  $R_c$  is the radius of the same circle.

It is straightforward to show that the center and radius of each circle are  $x_c = a/\tanh \tau$  and  $R_c = a/\sinh \tau$ , respectively.

Instead of the parameter  $\tau$ , one can use the angle  $\xi$  presented in Fig. .3 with  $\cot \xi = \sqrt{x_c^2 - R_c^2}/R_c$ , see Fig. .3. So, we can replace instead of  $x_c$  and  $R_c$  their functions. Now, the Cartesian coordinate  $x$ ,  $y$  and  $z$  can be defined as a function of bispherical coordinate  $(\xi, \eta, \phi)$

$$\begin{cases} x = \frac{a \sin \eta \sin \xi \cos \phi}{1 + \sin \xi \cos \eta} & 0 < \eta < \pi \\ y = \frac{a \sin \eta \sin \xi \sin \phi}{1 + \sin \xi \cos \eta} & 0 < \xi < \pi \\ z = \frac{a \cos \xi}{1 + \sin \xi \cos \eta} & 0 < \phi < 2\pi \end{cases} \quad (.5)$$

Since the bipolar coordinate system is orthogonal, its metric tensor is diagonal.

Using Eq. .5, we can find the diagonal terms  $h_\xi^2 = g_{\xi\xi}$  as follows,

$$h_\xi^2 = g_{\xi\xi} = \sum_k \left( \frac{\partial X_k}{\partial \xi} \right)^2 = \left( \frac{\partial x}{\partial \xi} \right)^2 + \left( \frac{\partial y}{\partial \xi} \right)^2 + \left( \frac{\partial z}{\partial \xi} \right)^2. \quad (.6)$$

The other diagonal components can be calculated the same way. Finally, we find,

$$\begin{cases} h_\xi = \frac{a}{1 + \sin \xi \cos \eta}, \\ h_\eta = \frac{a \sin \xi}{1 + \sin \xi \cos \eta}, \\ h_\phi = \frac{a \sin \xi \sin \eta}{1 + \sin \xi \cos \eta}. \end{cases} \quad (.7)$$

## .2 Some useful relations in the bispherical coordinate

To obtain the free energy of a tactoid, we need to calculate  $(\nabla \cdot \mathbf{n})$ ,  $(\mathbf{n} \cdot (\nabla \times \mathbf{n}))$ ,  $(\mathbf{n} \times (\nabla \times \mathbf{n}))$  and  $(\nabla \cdot (\mathbf{n} \nabla \cdot \mathbf{n} + \mathbf{n} \times (\nabla \times \mathbf{n})))$  with  $\mathbf{n}$  the director field. Consider a general vector  $\mathbf{A} = A_1 \hat{u}_1 + A_2 \hat{u}_2 + A_3 \hat{u}_3$ . Its divergence in the bispherical coordinate reads

$$\nabla \cdot \mathbf{A} = \frac{1}{h_1 h_2 h_3} \left( \frac{\partial}{\partial u_1} (h_2 h_3 A_1) + \frac{\partial}{\partial u_2} (h_1 h_3 A_2) + \frac{\partial}{\partial u_3} (h_1 h_2 A_3) \right) \quad (.8)$$

and the curl is,

$$\begin{aligned} \nabla \times \mathbf{A} = & \frac{1}{h_2 h_3} \left( \frac{\partial}{\partial u_2} (h_3 A_3) - \frac{\partial}{\partial u_3} (h_2 A_2) \right) \hat{u}_1 \\ & + \frac{1}{h_1 h_3} \left( \frac{\partial}{\partial u_3} (h_1 A_1) - \frac{\partial}{\partial u_1} (h_3 A_3) \right) \hat{u}_2 + \frac{1}{h_1 h_2} \left( \frac{\partial}{\partial u_1} (h_2 A_2) - \frac{\partial}{\partial u_2} (h_1 A_1) \right) \hat{u}_3 \end{aligned} \quad (.9)$$

The divergence and curl of vector  $\mathbf{n} = \mathbf{1}\hat{\xi} + \mathbf{0}\hat{\eta} + \mathbf{0}\hat{\phi}$  then become

$$\begin{aligned}
\nabla \cdot \mathbf{n} &= \frac{1}{h_\xi h_\eta h_\phi} \frac{\partial}{\partial \xi} (h_\eta h_\phi) \\
&= \frac{(1 + \sin \xi \cos \eta)^3}{a^3 \sin^2 \xi \sin \eta} \left( \frac{\partial}{\partial \xi} \frac{a^2 \sin^2 \xi \sin \eta}{(1 + \sin \xi \cos \eta)^2} \right) \\
&= \frac{2}{a} \cot \xi
\end{aligned} \tag{.10}$$

$$\begin{aligned}
\nabla \times \mathbf{n} &= \frac{1}{h_\xi h_\phi} \left( \frac{\partial}{\partial \phi} h_\xi \right) \hat{\eta} - \frac{1}{h_\xi h_\eta} \left( \frac{\partial}{\partial \eta} h_\xi \right) \hat{\phi} \\
&= \frac{(1 + \sin \xi \cos \eta)^2}{a^2 \sin \xi} \left( \frac{\partial}{\partial \eta} \frac{a}{1 + \sin \xi \cos \eta} \right) \hat{\phi} \\
&= -\frac{\sin \eta}{a} \hat{\phi}
\end{aligned} \tag{.11}$$

We can easily see that  $\mathbf{n} \cdot \nabla \times \mathbf{n} = \mathbf{0}$  and that

$$\mathbf{n} \times \nabla \times \mathbf{n} = \frac{1}{\mathbf{a}} \sin \eta \left( \hat{\xi} \times \hat{\phi} \right) = \frac{1}{\mathbf{a}} \sin \eta \hat{\eta}. \tag{.12}$$

### .3 Scaling theory

To obtain the scaling behavior of the free energy of a tactoid, we set the volume of the droplet  $V = r^2 R$  and its surface area  $S = rR$ . As in the main text, the bipolarity is denoted by  $y = \tilde{R}/R$  and the aspect ratio by  $x = R/r$ . To find the free energy, we need to calculate the volume integral of  $(\nabla \cdot \mathbf{n})^2$  and  $|\mathbf{n} \times \nabla \times \mathbf{n}|^2$  and  $(\mathbf{E} \cdot \mathbf{n})^2$  and the surface integral of  $(\mathbf{q} \cdot \mathbf{n})^2$ , in terms of  $x$ ,  $y$  and  $V$ .

Considering that  $\nabla \cdot \mathbf{n}$  is proportional to  $R/\tilde{R}^2$ , the splay term can then be written as

$$\int (\nabla \cdot \mathbf{n})^2 dV \propto \frac{R^2}{\tilde{R}^4} r^2 R \propto y^{-4} x^{-1} V^{1/3} x^{-1/3}, \quad (.13)$$

where we have used the relation  $r \propto V^{1/3} x^{-1/3}$  between  $r$  and  $V$  in the last term. One can also argue that  $|\nabla \times \mathbf{n}|$  is proportional to  $r/\tilde{R}^2$  because as the width of the droplet increase, the contribution to the bending energy increases too. Further, the bending energy decreases if the director-field becomes more homogeneous. Thus the bending term can be written as

$$\int |\mathbf{n} \times (\nabla \times \mathbf{n})|^2 dV \propto \frac{R^4}{\tilde{R}^4} \frac{r^3}{R^3} r \propto y^{-4} x^{-3} V^{1/3} x^{-1/3}. \quad (.14)$$

Next we need to calculate the scaling behavior of the  $\mathbf{q} \cdot \mathbf{n}$  term associated with the anchoring strength contribution to the free energy. In Sect. V below, we show that

$$\mathbf{q} \cdot \mathbf{n} \sim \left( \frac{r}{R} - \frac{Rr}{\tilde{R}^2} \right). \quad (.15)$$

Thus the contribution of the anchoring strength term to the surface energy scales as,

$$\int \omega (\mathbf{q} \cdot \mathbf{n})^2 dS \propto \omega r R \left( \frac{r}{R} - \frac{Rr}{\tilde{R}^2} \right)^2 \propto \omega r R \left( \frac{r}{R} \right)^2 \left( 1 - \frac{R^2}{\tilde{R}^2} \right) \propto \omega V^{2/3} x^{-5/3} (1 - y^{-2}). \quad (.16)$$

Finally, we need to calculate the interaction of director-field with the electric field as follows,

$$-\frac{1}{8\pi} \epsilon_a \int (\mathbf{E} \cdot \mathbf{n})^2 dV \propto -\epsilon_a E^2 \frac{R^2 r^2}{\tilde{R}^4} R \propto -\epsilon_a E^2 y^{-4} x^{-2} V, \quad (.17)$$

where we have used the expression obtained in Sect. V below for  $\mathbf{E} \cdot \mathbf{n}$  in the limit of large  $\tilde{R}$ .

## .4 Free energy in bispherical coordinates

In this section, we derive Eqs. 5-13 in the main text. We parametrize the director field  $\mathbf{n} \equiv \mathbf{t}/|\mathbf{t}|$  in the cylindrical coordinate with  $\mathbf{t} = 2\rho z \hat{\rho} - (\tilde{\mathbf{R}}^2 + \rho^2 - \mathbf{z}^2)\hat{\mathbf{z}}$ . Here, as in the main text,  $\tilde{R}$  is the distance between the (virtual) boojums,  $R$  is the length of droplet and  $\hat{\rho}$  and  $\hat{\mathbf{z}}$  are the unit vector along the radial direction and the main axis of the tactoid in a cylindrical coordinate system, respectively. In a bispherical coordinate system, we have  $\rho = R \sin \xi \sin \eta / Z$  and  $z = R \cos \xi / Z$  with  $Z = 1 + \sin \xi \cos \eta$ .

We first calculate the divergence and curl of  $\mathbf{n}$  in the cylindrical coordinate and then transfer them to the bispherical one in order to obtain the free energy of a droplet illustrated in Fig. 2. In the cylindrical coordinate, we have

$$\nabla \cdot \mathbf{n} = \frac{1}{\rho} \frac{\partial \rho \mathbf{n}_\rho}{\partial \rho} + \frac{1}{\rho} \frac{\partial \mathbf{n}_\varphi}{\partial \varphi} + \frac{\partial \mathbf{n}_z}{\partial z} \quad (.18)$$

with

$$\mathbf{n} = \frac{2\rho z}{\sqrt{4\rho^2 z^2 + (\tilde{\mathbf{R}}^2 + \rho^2 - \mathbf{z}^2)^2}} \hat{\rho} - \frac{(\tilde{\mathbf{R}}^2 + \rho^2 - \mathbf{z}^2)}{\sqrt{4\rho^2 z^2 + (\tilde{\mathbf{R}}^2 + \rho^2 - \mathbf{z}^2)^2}} \hat{\mathbf{z}} \quad (.19)$$

After some tedious calculation, we find

$$\nabla \cdot \mathbf{n} = \frac{4z}{\left(4\rho^2 z^2 + (\tilde{\mathbf{R}}^2 + \rho^2 - \mathbf{z}^2)^2\right)^{1/2}}, \quad (.20)$$

and

$$\begin{aligned}
(\nabla \cdot \mathbf{n})^2 &= \frac{16z^2}{4\rho^2 z^2 + (\tilde{R}^2 + \rho^2 - z^2)^2} \\
&= \frac{4R^{-2} \cos^2 \xi}{Z^2 \left( \sin^2 \xi \sin^2 \eta \cos^2 \xi / Z^4 + \left( \tilde{R}^2 / 2R^2 + \sin^2 \xi \sin^2 \eta / 2Z^2 - \cos^2 \xi / 2Z^2 \right)^2 \right)}. \tag{.21}
\end{aligned}$$

We set the denominator of the above equation equal to  $N$ , and simplify it to find

$$N = \left( \sin^2 \xi \sin^2 \eta \tilde{R}^2 / R^2 + \left( Z/2 \left( \tilde{R}^2 / 2R^2 - 1 \right) + \sin \xi \cos \eta \right)^2 \right) \tag{.22}$$

It is straightforward to show that

$$NR^4 = |t|^2 Z^2, \tag{.23}$$

which we will use later. The curl in the cylindrical coordinate can be calculated as follows,

$$\nabla \times \mathbf{n} = \left( \frac{1}{\rho} \frac{\partial n_z}{\partial \varphi} - \frac{\partial n_\varphi}{\partial z} \right) \hat{\rho} + \left( \frac{\partial n_\rho}{\partial z} - \frac{\partial n_z}{\partial \rho} \right) \hat{\varphi} + \frac{1}{\rho} \left( \frac{\partial}{\partial \rho} (\rho n_\varphi) - \frac{\partial n_\rho}{\partial \varphi} \right) \hat{z}, \tag{.24}$$

which becomes,

$$\nabla \times \mathbf{n} = \frac{2\rho \left( \tilde{R}^2 + \rho^2 - z^2 \right)^2 + 8\rho^3 z^2}{\left( 4\rho^2 z^2 + \left( \tilde{R}^2 + \rho^2 - z^2 \right)^2 \right)^{3/2}} \hat{\varphi} = \frac{2\rho}{\left( 4\rho^2 z^2 + \left( \tilde{R}^2 + \rho^2 - z^2 \right)^2 \right)^{1/2}} \hat{\varphi}. \tag{.25}$$

Using the above equation, we can calculate the following term

$$\begin{aligned}
|\mathbf{n} \times (\nabla \times \mathbf{n})|^2 &= \frac{4R^2 \sin^2 \xi \sin^2 \eta Z^{-2}}{|\mathbf{t}|^2} \\
&= \frac{4R^2 \sin^2 \xi \sin^2 \eta Z^{-2}}{NR^4 Z^{-2}} \\
&= \frac{4R^{-2} \sin^2 \xi \sin^2 \eta}{N},
\end{aligned} \tag{.26}$$

which we will use later when we calculate the bending energy.

To calculate the contribution of anchoring strength to the free energy, we need to calculate the term  $(\mathbf{q} \cdot \mathbf{n})^2$  with  $\mathbf{q}$  the normal vector to the surface. Setting the unit tangent vector to the surface with  $\mathbf{t}'$ , we then find  $(\mathbf{t}' \times \mathbf{n})^2 = (\mathbf{q} \cdot \mathbf{n})^2$ . We emphasize that  $\mathbf{t}'$  is the tangent vector to the surface, not the tangent vector to the field lines that we denoted  $\mathbf{t}$  above. The unit tangent vector  $\mathbf{t}'$  can be written as  $\mathbf{t}' \equiv \mathbf{t}''/|\mathbf{t}''|$  with  $\mathbf{t}'' = 2\rho z \hat{\rho} - (R^2 + \rho^2 - z^2) \hat{z}$ . Therefore,

$$|\mathbf{q} \cdot \mathbf{n}| = \frac{|\mathbf{t}'' \times \mathbf{t}|}{|\mathbf{t}''||\mathbf{t}|} = \frac{|(2\rho z \hat{\rho} - (R^2 + \rho^2 - z^2) \hat{z}) \times (2\rho z \hat{\rho} - (\tilde{R}^2 + \rho^2 - z^2) \hat{z})|}{\sqrt{4\rho^2 z^2 + (R^2 + \rho^2 - z^2)^2} \sqrt{4\rho^2 z^2 - (\tilde{R}^2 + \rho^2 - z^2)^2}}, \tag{.27}$$

or, in the bispherical coordinate, we can finally write

$$|\mathbf{q} \cdot \mathbf{n}|^2 = \frac{4 \sin^2 \eta \cos^2 \xi \left( \tilde{R}^2 / R^2 - 1 \right)^2}{4N}. \tag{.28}$$

Last but not least, we need to calculate  $\mathbf{E} \cdot \mathbf{n}$  to obtain the effect of the interaction of the external field  $\mathbf{E}$  with the tactoid. Considering that  $\mathbf{n} = \mathbf{t}/|\mathbf{t}|$  and assuming that the electric field is in the  $z$  direction, we find

$$\begin{aligned}
\frac{(\mathbf{E} \cdot \mathbf{t})^2}{|t|^2} &= \frac{E^2 \left( \tilde{R}^2 + \rho^2 - z^2 \right)^2}{|t|^2} \\
&= \frac{E^2 R^4 Z^{-4} \left( Z^2 \tilde{R}^2 / R^2 + \sin^2 \xi \sin^2 \eta - \cos^2 \xi \right)^2}{NR^4 Z^{-2}} \\
&= \frac{E^2 \left( Z^2 \tilde{R}^2 / R^2 + \sin^2 \xi \sin^2 \eta - \cos^2 \xi \right)^2}{N (1 + \sin \xi \cos \eta)^2}.
\end{aligned} \tag{.29}$$

To obtain the free energy given in Eq. 5 in the main text, we insert into Eq. 2 of the paper the expressions obtained above for  $(\nabla \cdot \mathbf{n})^2$  (Eq. .21),  $|\mathbf{n} \times (\nabla \times \mathbf{n})|^2$  (Eq. .26),  $|\mathbf{q} \cdot \mathbf{n}|^2$  (Eq. .28), and  $\mathbf{E} \cdot \mathbf{n}$  (Eq. .29). Note that the volume of a droplet in the bispherical coordinate can be written as,

$$V(\alpha, R) = \int_0^{2\pi} \int_0^\alpha \int_0^\pi h_\xi h_\eta h_\phi \, d\xi \, d\eta \, d\phi = R^3 \phi_v(\alpha), \tag{.30}$$

where  $\alpha$  is the angle shown in Fig. 2 in the main text,  $\phi_v(\alpha)$  is

$$\phi_v(\alpha) = \frac{7\pi}{3} + \frac{\pi}{2} \left( \frac{1 - 4\alpha \cot \alpha + 3 \cos 2\alpha}{\sin^2 \alpha} \right), \tag{.31}$$

and the surface can be expressed as

$$S(\alpha, R) = \int_0^{2\pi} \int_0^\pi h_\xi h_\phi \, d\xi \, d\phi = R^2 \phi_\sigma(\alpha) \tag{.32}$$

with

$$\phi_\sigma(\alpha) = 4\pi \left( \frac{1 - \alpha \cot \alpha}{\sin \alpha} \right). \tag{.33}$$

Using Eq. .28, the term in the free energy originating from the anchoring of the director field to the interface is

$$\begin{aligned}\phi_\omega(\alpha, y) &= \frac{1}{R^2} \int_0^{2\pi} \int_0^\pi (\mathbf{q} \cdot \mathbf{n})^2 h_\xi h_\phi \, d\xi \, d\phi \\ &= \frac{\pi}{2} (y^2 - 1)^2 \sin^3 \alpha \int_0^\pi d\xi \left[ \frac{\sin \xi \cos^2 \xi}{N(y, \xi, \alpha) (1 + \sin \xi \cos \alpha)^2} \right],\end{aligned}\tag{.34}$$

which is equal to Eq. 8 in the main text and cannot be solved analytically.

Note that we have set  $\eta = \alpha$  in the expressions given in Eqs. (8) and (9) in the paper.

Using Eq. .21, we can also calculate the contribution of the splay deformation to the Frank elastic energy as follows,

$$\begin{aligned}\phi_{11}(\alpha, y) &= \frac{1}{R} \int_0^{2\pi} \int_0^\pi \int_0^\alpha (\nabla \cdot \mathbf{n})^2 h_\xi h_\eta h_\phi \, d\xi \, d\eta \, d\phi \\ &= 8\pi \int_0^\pi d\xi \int_0^\alpha d\eta \frac{\sin^2 \xi \cos^2 \xi \sin \eta}{N(y, \xi, \eta) (1 + \sin \xi \cos \eta)^3},\end{aligned}\tag{.35}$$

which cannot be solved analytically either.

Using Eq. .26, the contribution of the bend elastic deformation reads

$$\begin{aligned}\phi_{33}(\alpha, y) &= \frac{1}{R} \int_0^{2\pi} \int_0^\pi \int_0^\alpha |\mathbf{n} \times \nabla \times \mathbf{n}|^2 h_\xi h_\eta h_\phi \, d\xi \, d\eta \, d\phi \\ &= 8\pi \int_0^\pi d\xi \int_0^\alpha d\eta \frac{\sin^4 \xi \sin^3 \eta}{N(y, \xi, \eta) (1 + \sin \xi \cos \eta)^3}.\end{aligned}\tag{.36}$$

Finally, the free energy of the interaction of the nematic drop with an electric field yields an even more daunting integral,

$$\begin{aligned}
\phi_C(\alpha, y) &= \frac{1}{R^3} \int_0^{2\pi} \int_0^\pi \int_0^\alpha (\mathbf{E} \cdot \mathbf{n})^2 h_\xi h_\eta h_\phi \, d\xi \, d\eta \, d\phi \\
&= 8\pi \int_0^\pi d\xi \int_0^\alpha d\eta \frac{\sin^2 \xi \sin \eta}{(1 + \sin \xi \cos \eta)^3} \\
&\quad \times \frac{E_z^2 \left( Z^2 \tilde{R}^2 / R^2 + \sin^2 \xi \sin^2 \eta - \cos^2 \xi \right)^2}{N (1 + \sin \xi \cos \eta)^2}.
\end{aligned} \tag{.37}$$

## .5 Small opening angle

In this section we calculate the free energy in the limit of the small opening angle.

We first expand  $\phi_v(\alpha)$  and  $\phi_\sigma(\alpha)$  given in Eqs. .31 and .33 in the limit of small  $\alpha$ ,

$$\phi_v(\alpha) = \frac{7\pi}{3} + \frac{\pi}{2 \sin^2 \alpha} (1 - 4\alpha \cot \alpha + 3 \cos(2\alpha)) \sim \frac{4\pi\alpha^2}{15} \tag{.38}$$

and

$$\phi_\sigma(\alpha) = 4\pi \frac{1 - \alpha \cot \alpha}{\sin \alpha} \sim \frac{4\pi\alpha}{3}, \tag{.39}$$

and next calculate different contributions to the free energy. Using Eq. .34, the term associated with the anchoring strength in the limit of small  $\alpha$  becomes,

$$\begin{aligned}
\phi_\omega(\alpha, y) &= \frac{\pi}{2} (y^2 - 1)^2 \sin^3 \alpha \int_0^\pi d\xi \left[ \frac{\sin \xi \cos^2 \xi}{N(y, \xi, \alpha) (1 + \sin \xi \cos \alpha)^2} \right] \\
&\sim (y^2 - 1)^2 \sin^3 \alpha \int_0^\pi d\xi \frac{\sin \xi \cos^2 \xi}{(1 + \sin \xi)^4 y^4} \\
&\sim (y^2 - 1)^2 y^{-4} \alpha^3 \\
&\sim (1 - y^{-2})^2 \alpha^3.
\end{aligned} \tag{.40}$$

We employ Eq. .40 to calculate the term associated with the anchoring strength given in Eq. 5 of the paper in the limit of small  $\alpha$ ,

$$\frac{\phi_\omega(\alpha, y)}{\phi_v^{2/3}(\alpha)} \sim (1 - y^{-2})^2 \alpha^3 \alpha^{-4/3} \sim (1 - y^{-2})^2 \alpha^{5/3} \sim (1 - y^{-2})^2 x^{-5/3}. \quad (.41)$$

Using Eq. .35 in the limit of small  $\alpha$ , we find,

$$\begin{aligned} \phi_{11}(\alpha, y) &= 8\pi \int_0^\pi d\xi \int_0^\alpha d\eta \frac{\sin^2 \xi \cos^2 \xi \sin \eta}{N(y, \xi, \eta) (1 + \sin \xi \cos \eta)^3} \\ &\sim y^{-4} \alpha^2 \int_0^\pi \frac{\sin^2 \xi \cos^2 \xi}{y^4 (1 + \sin \xi)^5} \\ &\sim y^{-4} \alpha^2. \end{aligned} \quad (.42)$$

We employ Eq. .42 to calculate the contribution of the splay term to Eq. 5 in the paper,

$$\frac{\phi_{11}(\alpha, y)}{\phi_v^{1/3}(\alpha)} \sim y^{-4} \alpha^{4/3} \sim y^{-4} x^{-4/3}. \quad (.43)$$

Next, to obtain the contribution of the bending term, we calculate Eq. .36 in the limit of small  $\alpha$ :

$$\begin{aligned} \phi_{33}(\alpha, y) &= 8\pi \int_0^\pi d\xi \int_0^\alpha d\eta \frac{\sin^4 \xi \sin^3 \eta}{N(y, \xi, \eta) (1 + \sin \xi \cos \eta)^3} \\ &\sim y^{-4} \alpha^4 \int_0^\pi \frac{\sin^4 \xi}{(1 + \sin \xi)^5} \\ &\sim y^{-4} \alpha^4, \end{aligned} \quad (.44)$$

and use it to find the contribution of bending energy to Eq. 5 of the paper as follows:

$$\frac{\phi_{33}(\alpha, y)}{\phi_v^{1/3}(\alpha)} \sim y^{-4} \alpha^{10/3} \sim y^{-4} x^{-10/3}. \quad (.45)$$

Finally, the interaction with the electric field  $\int (\mathbf{E} \cdot \mathbf{n})^2 dV$  in the limit of small  $\alpha$  becomes,

$$\begin{aligned}
-\int (\mathbf{E} \cdot \mathbf{n})^2 dV &= -\int \frac{E_z^2 (\tilde{R}^2 + \rho^2 - z^2)^2}{4\rho^2 z^2 + (\tilde{R}^2 + \rho^2 - z^2)^2} dV \\
&= -\int E_z^2 \left( 1 + \frac{4\rho^2 z^2}{(\tilde{R}^2 + \rho^2 - z^2)^2} \right)^{-1} dV \\
&\sim -\int E_z^2 \left( 1 - \frac{4 \sin^2 \xi \cos^2 \xi \sin^2 \eta}{(Z^2 \tilde{R}^2 / R^2 + \sin^2 \xi \sin^2 \eta - \cos^2 \xi)^2} \right) dV \quad (.46) \\
&\sim -E_z^2 R^3 \alpha^4 \int_0^\pi \frac{4 \sin^2 \xi \cos^2 \xi}{\tilde{R}^4 / R^4} \frac{\sin^2 \xi}{(1 + \sin \xi)^3} d\xi \\
&\sim -V E_z^2 x^{-2} y^{-4},
\end{aligned}$$

where we dropped the integral as it is just a number. All equations obtained in this section in the limit of the small opening angle are in agreement with the scaling theory presented in the main text.

## .6 Linear analysis

To investigate the dynamical Eqs. (4.11) and (4.12) at the level of a linear response theory, we insert  $\eta_1(\tau) = \eta_{1,\infty}(1 + \delta_1(\tau))$  and  $\eta_3(\tau) = \eta_{3,\infty}(1 + \delta_3(\tau))$  with  $|\delta_1(\tau)| \ll 1$  and  $|\delta_3(\tau)| \ll 1$  perturbations to the steady-state (equilibrium) values  $\eta_{1,\infty}$  and  $\eta_{3,\infty}$ , and linearize them. This produces a set of equations that can be put in the form of the matrix equation  $d\boldsymbol{\delta}/d\tau = -\mathbf{M} \cdot \boldsymbol{\delta}$ , where  $\boldsymbol{\delta} \equiv (\delta_1, \delta_3)^T$  is the perturbation vector and the kinetic matrix  $\mathbf{M}$  becomes

$$\mathbf{M} \equiv \begin{bmatrix} \frac{1}{\eta_{s,\infty}} + \frac{1}{q_1 \eta_{1,\infty}} & \frac{\eta_{3,\infty}}{\eta_{1,\infty} \eta_{s,\infty}} \\ \Gamma \frac{\eta_{1,\infty}}{\eta_{3,\infty} \eta_{s,\infty}} & \Gamma \left( \frac{1}{\eta_{s,\infty}} + \frac{1}{q_3 \eta_{3,\infty}} \right) \end{bmatrix}, \quad (.47)$$

with  $\eta_{s,\infty} = 1 - \eta_{1,\infty} - \eta_{3,\infty}$  the equilibrium fraction of protein subunits free in solution. To find the eigenvalues  $\lambda_{\pm}$  of the matrix  $\mathbf{M}$ , we write  $\det(\mathbf{M} - \lambda_{\pm}\mathbf{I}) = 0$  with  $\mathbf{I}$  the identity matrix, and obtain

$$\lambda_{\pm} = \frac{1}{2}a \pm \frac{1}{2}\sqrt{a^2 - 4b}, \quad (.48)$$

with

$$a \equiv \frac{1}{\eta_{s,\infty}} + \frac{1}{q_1\eta_{1,\infty}} + \Gamma \left( \frac{1}{\eta_{s,\infty}} + \frac{1}{q_3\eta_{3,\infty}} \right), \quad (.49)$$

and

$$b \equiv \frac{\Gamma}{\eta_{s,\infty}} \left[ \frac{1}{q_1\eta_{1,\infty}} + \frac{1}{q_3\eta_{3,\infty}} + \frac{\eta_{s,\infty}}{q_1\eta_{1,\infty}q_3\eta_{3,\infty}} \right]. \quad (.50)$$

In the limit where  $4b/a^2 \ll 1$ , the eigenvalues representing the fundamental relaxation rates reduce to

$$\lambda_+ \sim a \times \left( 1 - \frac{b}{a^2} \right) \quad (.51)$$

and

$$\lambda_- \sim a \times \frac{b}{a^2}, \quad (.52)$$

up to linear order in  $b/a^2$ . Notice that to leading order  $\lambda_- \sim \lambda_+ b/a^2$ , implying that  $\lambda_- \ll \lambda_+$  and there must be a strong separation of time scales. Under conditions where  $q_1\eta_{1,\infty} \gg \eta_{s,\infty}$  and  $q_3\eta_{3,\infty} \gg \eta_{s,\infty}$ , these expressions simplify to Eqs. (4.13) and (4.14). For these conditions to hold, we must have  $q_1\eta_{1,\infty} \gg 1$  and  $q_3\eta_{3,\infty} \gg 1$ : the equilibrium (final) fraction of proteins in both types of capsids cannot be smaller than the reciprocal of their aggregation numbers.

Obviously, for the rates to remain real numbers, we must insist that  $4b \leq a^2$ . For  $\Gamma \rightarrow 0$  and  $\Gamma \rightarrow \infty$ , this is easily verified but for arbitrary values this is not so trivial noting that  $\eta_{1,\infty}$  and  $\eta_{3,\infty}$  are not independent (see Eq. (4.6)). Figure 4.4, showing  $\lambda_{\pm}$  for  $\Gamma = 1$ , suggests this is always the case. Finally, if  $4b \rightarrow a^2$ , the rates approach each other and become equal to

$$\lambda_{\pm} \sim \frac{1}{2}a, \quad (.53)$$

indicating in this particular case the presence of a single time scale.

The solution for  $\delta(\tau)$ , can be written in terms of a linear combination of the (unnormalized) eigenvectors  $\mathbf{v}_{\pm}$  associated with the eigenvalues  $\lambda_{\pm}$ ,

$$\delta(\tau) = c_+ \mathbf{v}_+ \exp\{(-\lambda_+ \tau)\} + c_- \mathbf{v}_- \exp\{(-\lambda_- \tau)\}, \quad (.54)$$

where

$$\mathbf{v}_{\pm} = \begin{pmatrix} \frac{\eta_{3,\infty} \eta_{1,\infty}^{-1} \eta_{s,\infty}^{-1}}{\eta_{s,\infty}^{-1} + q_1^{-1} \eta_{1,\infty}^{-1} - \lambda_{\pm}} \\ -1 \end{pmatrix}, \quad (.55)$$

and  $c_+$  and  $c_-$  are constants that are fixed by the initial conditions  $\delta(0) = c_+ \mathbf{v}_+ + c_- \mathbf{v}_-$ , noting that  $\delta_T(0) = (\eta_T(0)/\eta_{T,\infty}) - 1$ . Notice also that  $\mathbf{v}_{\pm}$  are not orthogonal, unless  $\Gamma = 1$  and  $\eta_{1,\infty} = \eta_{3,\infty}$  in which case the matrix  $\mathbf{M}$  is symmetric. If  $4b = a^2$ , there is only one eigenvector.

## .7 Complete capsid conversions

We made an attempt to fit the experimental data precisely according to our theory, focusing on achieving an exact match between the concentrations of  $T = 1$  and  $T = 3$  after two months. To account for the experimental conditions where only one species is expected to survive at the end, we assigned greater significance to the end points during the data fitting process. Figures .4 and .5 clearly indicate that obtaining a satisfactory fit to the experimental data is not feasible under these conditions.

Figure .4 shows the experimental data illustrating the conversion of a solution primarily composed of  $T = 1$  particles to a solution where the dominant species are the  $T = 3$  particles after  $t = 1440$  hrs. In line with the main text, the symbols represent two sets of experimental data, while the solid lines represent the fitted curves. Our objective is to determine the best-fitting line that passes through the last final experimental data point. The initial conditions are set to  $\eta_1(0) = 0.86$  and  $\eta_3(0) = 0.02$ , and the equilibrium fractions are set at  $\eta_{1,\infty} = 0.02$  and  $\eta_{3,\infty} = 0.85$ . Using these equilibrium fractions, we derive binding energies of  $g_1 = -11.4$  and  $g_3 = -11.8$ , indicating a difference of  $\Delta g = -0.4$ . The corresponding rate constants are  $\Gamma_1 = 39.0 \text{ hrs}^{-1}$  and  $\Gamma_3 = 0.04 \text{ hrs}^{-1}$ , resulting in  $\Gamma = 0.001$ . The agreement between theory and experiment is clearly not ideal with an  $r^2$  value of 0.61. Table .1 presents the rate constants and binding free energies obtained from our data fitting analysis of the interconversion between  $T = 1$  and  $T = 3$ .

Figure .5 shows the experimental data illustrating the conversion of a solution primarily composed of  $T = 3$  particles to a solution where the dominant species are the  $T = 1$  particles after  $t = 1608$  hrs. The initial conditions are set to  $\eta_1(0) = 0.01$  and

$\eta_3(0) = 0.72$ , and the equilibrium fractions are set at  $\eta_{1,\infty} = 0.62$  and  $\eta_{3,\infty} = 0.04$ . Using these equilibrium fractions, we derive binding energies of  $g_1 = -10.5$  and  $g_3 = -10.8$ , indicating a difference of  $\Delta g = -0.3$ . The corresponding rate constants are  $\Gamma_1 = 1.8 \text{ hrs}^{-1}$  and  $\Gamma_3 = 7.8 \text{ hrs}^{-1}$ , resulting in  $\Gamma = 4.4$ . The agreement between theory and experiment is again not ideal, with an  $r^2$  value of 0.425. Table .1 presents the rate constants and binding free energies obtained from our data fitting analysis of the interconversion between  $T = 3$  and  $T = 1$ .

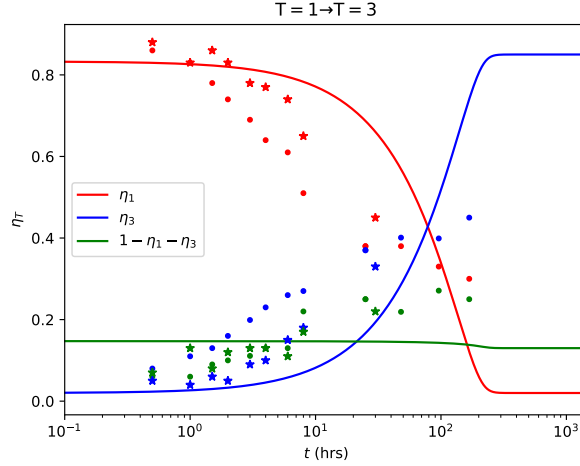


Figure .4: Fraction of protein in various species  $\eta_T$  as a function of time  $t$  in hours. Symbols: results from two data sets where following a quench  $T = 1$  capsids convert into  $T = 3$  capsids. For two months of the measurements of Timmermans *et al.* [134] are shown. The red, blue, and green lines indicate the fractions of  $T = 1$ ,  $T = 3$ , and free subunits. See the text in Appendix B.

Conversion	$\Gamma_1$ [hrs] <sup>-1</sup>	$\Gamma_3$ [hrs] <sup>-1</sup>	$\Gamma$	$g_1$	$g_3$	$\Delta g$
$T = 1 \rightarrow T = 3$	39.0	0.04	0.001	-11.4	-11.8	-0.4
$T = 3 \rightarrow T = 1$	1.8	7.8	4.4	-10.5	-10.8	-0.3

Table .1: The numerical values of the model parameters obtained from fitting the relaxational model to the experimental data for the complete two month conversions of  $T = 1 \rightarrow T = 3$  and  $T = 3 \rightarrow T = 1$  capsids with  $d\tau = 0.01$ .  $\Gamma_1$  and  $\Gamma_3$  are the relaxation rates associated with the assembly and disassembly of the  $T = 1$  and  $T = 3$  capsids, and  $\Gamma = \Gamma_3/\Gamma_1$  their ratio. The dimensionless free energies of binding of coat protein subunits are  $g_1$  and  $g_3$ , and  $\Delta g = g_3 - g_1$  their difference. See also the main text.

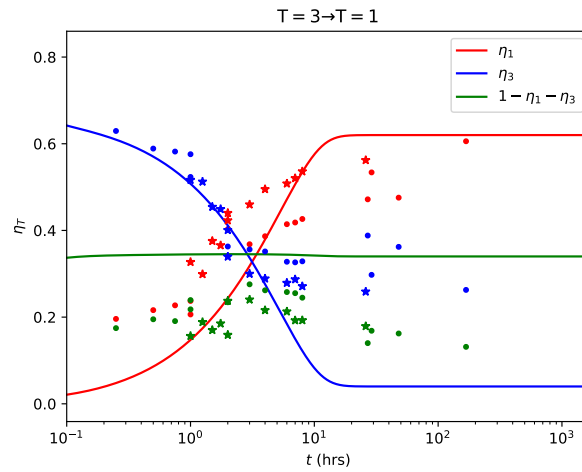


Figure 5: Fraction of protein in various species  $\eta_T$  as a function of time  $t$  in hours. Symbols: results from two data sets where following a quench  $T = 3$  capsids convert into  $T = 1$  capsids. For two months of the measurements of Timmermans *et al.* [134] are shown. The red, blue, and green lines indicate the fractions of  $T = 1$ ,  $T = 3$ , and free subunits. See also the text in Appendix B.

# Bibliography

- [1] Mohammadamin Safdari, Roya Zandi, and Paul Van der Schoot. Effect of electric fields on the director field and shape of nematic tactoids. *Physical Review E*, 103(6):062703, 2021.
- [2] JS van Duijneveldt and DJTJocp Frenkel. Computer simulation study of free energy barriers in crystal nucleation. *The Journal of Chemical Physics*, 96(6):4655–4668, 1992.
- [3] René van Roij. The isotropic and nematic liquid crystal phase of colloidal rods. *European Journal of Physics*, 26(5):S57, 2005.
- [4] M Paul Lettinga, Kyongok Kang, Arnout Imhof, Didi Derks, and Jan K G Dhont. Kinetic pathways of the nematic–isotropic phase transition as studied by confocal microscopy on rod-like viruses. *Journal of Physics: Condensed Matter*, 17(45):S3609–S3618, oct 2005. doi: 10.1088/0953-8984/17/45/055. URL <https://doi.org/10.1088%2F0953-8984%2F17%2F45%2F055>.
- [5] M. Paul Lettinga, Kyongok Kang, Peter Holmqvist, Arnout Imhof, Didi Derks, and Jan K. G. Dhont. Nematic-isotropic spinodal decomposition kinetics of rodlike viruses. *Physical Review E*, 73:011412, Jan 2006. doi: 10.1103/PhysRevE.73.011412. URL <https://link.aps.org/doi/10.1103/PhysRevE.73.011412>.
- [6] Vida Jamali, Natnael Behabtu, Bohdan Senyuk, J. Alex Lee, Ivan I. Smalyukh, Paul van der Schoot, and Matteo Pasquali. Experimental realization of crossover in shape and director field of nematic tactoids. *Physical Review E*, 91:042507, Apr 2015. doi: 10.1103/PhysRevE.91.042507. URL <https://link.aps.org/doi/10.1103/PhysRevE.91.042507>.
- [7] S Fraden, AJ Hurd, RB Meyer, M Cahoon, and DLD Caspar. Magnetic-field-induced alignment and instabilities in ordered colloids of tobacco mosaic virus. *Le Journal de Physique Colloques*, 46(C3):C3–85, 1985.

- [8] H Zöcher. Über freiwillige Strukturbildung in Solen. (Eine neue Art anisotrop flüssiger Medien.). *Zeitschrift für anorganische und allgemeine Chemie*, 147:91–110, 1925. doi: <https://doi.org/10.1098/rsta.2017.0042>. URL [https://ucelinks.cdlib.org/sfx\\_local?genre=article&id=doi:10.1002%2Fzaac.19251470111&sid=literatum%3Arsj&date=1925&atitle=%C3%9Cber%20freiwillige%20Strukturbildung%20in%20Solen.%20%28Eine%20neue%20Art%20anisotrop%20fl%C3%BCssiger%20Medien.%29&jtitle=Z.%20Anorg.%20Allg.%20Chem.&volume=147&spage=91&epage=110](https://ucelinks.cdlib.org/sfx_local?genre=article&id=doi:10.1002%2Fzaac.19251470111&sid=literatum%3Arsj&date=1925&atitle=%C3%9Cber%20freiwillige%20Strukturbildung%20in%20Solen.%20%28Eine%20neue%20Art%20anisotrop%20fl%C3%BCssiger%20Medien.%29&jtitle=Z.%20Anorg.%20Allg.%20Chem.&volume=147&spage=91&epage=110).
- [9] F C Bawden. Liquid crystalline substances from virus-infected plants. *Nature*, 138:1051–1052, Aug 1936. doi: <https://doi.org/10.1098/rsta.2017.0042>. URL [https://ucelinks.cdlib.org/sfx\\_local?genre=article&id=doi:10.1038%2F1381051a0&sid=literatum%3Arsj&date=1936&atitle=Liquid%20crystalline%20substances%20from%20virus-infected%20plants&jtitle=Nature&volume=138&spage=1051&epage=1052](https://ucelinks.cdlib.org/sfx_local?genre=article&id=doi:10.1038%2F1381051a0&sid=literatum%3Arsj&date=1936&atitle=Liquid%20crystalline%20substances%20from%20virus-infected%20plants&jtitle=Nature&volume=138&spage=1051&epage=1052).
- [10] K. Coper and H. Freundlich. The formation of tactoids in iron oxide sols. *Transactions of the Faraday Society*, 33:348–350, 1937. doi: 10.1039/TF9373300348. URL <http://dx.doi.org/10.1039/TF9373300348>.
- [11] Conmar Robinson. Liquid-crystalline structures in solutions of a polypeptide. *Transactions of the Faraday Society*, 52:571–592, 1956. doi: 10.1039/TF9565200571. URL <http://dx.doi.org/10.1039/TF9565200571>.
- [12] Nicolas Puech, Eric Grelet, Philippe Poulin, Christophe Blanc, and Paul van der Schoot. Nematic droplets in aqueous dispersions of carbon nanotubes. *Physical Review E*, 82:020702, Aug 2010. doi: 10.1103/PhysRevE.82.020702. URL <https://link.aps.org/doi/10.1103/PhysRevE.82.020702>.
- [13] Vida Jamali, Evan G Biggers, Paul van der Schoot, and Matteo Pasquali. Line tension of twist-free carbon nanotube lyotropic liquid crystal microdroplets on solid surfaces. *Langmuir*, 33(36):9115–9121, 2017.
- [14] Zvonimir Dogic. Surface freezing and a two-step pathway of the isotropic-smectic phase transition in colloidal rods. *Physical Review Letters*, 91:165701, Oct 2003. doi: 10.1103/PhysRevLett.91.165701. URL <https://link.aps.org/doi/10.1103/PhysRevLett.91.165701>.
- [15] Anna Modlińska, Ahmed M. Alsayed, and Thomas Gibaud. Condensation and dissolution of nematic droplets in dispersions of colloidal rods with thermo-sensitive depletants. *Scientific Reports*, 5:18432, December 2015. doi: 10.1038/srep18432. URL <https://doi.org/10.1038/srep18432>.

- [16] Patrick W. Oakes, Jorge Viamontes, and Jay X. Tang. Growth of tactoidal droplets during the first-order isotropic to nematic phase transition of F-actin. *Physical Review E*, 75:061902, Jun 2007. doi: 10.1103/PhysRevE.75.061902. URL <https://link.aps.org/doi/10.1103/PhysRevE.75.061902>.
- [17] Kimberly L Weirich, Shiladitya Banerjee, Kinjal Dasbiswas, Thomas A Witten, Suriyanarayanan Vaikuntanathan, and Margaret L Gardel. Liquid behavior of cross-linked actin bundles. *Proceedings of the National Academy of Sciences*, 114(9):2131–2136, 2017.
- [18] Kimberly L Weirich, Kinjal Dasbiswas, Thomas A Witten, Suriyanarayanan Vaikuntanathan, and Margaret L Gardel. Self-organizing motors divide active liquid droplets. *Proceedings of the National Academy of Sciences*, 116(23):11125–11130, 2019.
- [19] Young-Ki Kim, Sergij V Shiyankovskii, and Oleg D Lavrentovich. Morphogenesis of defects and tactoids during isotropic–nematic phase transition in self-assembled lyotropic chromonic liquid crystals. *Journal of Physics: Condensed Matter*, 25(40):404202, sep 2013. doi: 10.1088/0953-8984/25/40/404202. URL <https://doi.org/10.1088/0953-8984/25/40/404202>.
- [20] Davide Marenduzzo, Alessandro Flammini, Antonio Trovato, Jayanth R Banavar, and Amos Maritan. Physics of thick polymers. *Journal of Polymer Science Part B: Polymer Physics*, 43(6):650–679, 2005.
- [21] Heinz-S. Kitzerow. Polymer-dispersed liquid crystals from the nematic curvilinear aligned phase to ferroelectric films. *Liquid Crystals*, 16(1):1–31, 1994. doi: 10.1080/02678299408036517. URL <https://doi.org/10.1080/02678299408036517>.
- [22] Ji Hyun Park, JungHyun Noh, Christina Schütz, German Salazar-Alvarez, Giusy Scalia, Lennart Bergström, and Jan P. F. Lagerwall. Macroscopic control of helix orientation in films dried from cholesteric liquid-crystalline cellulose nanocrystal suspensions. *ChemPhysChem*, 15(7):1477–1484, 2014. doi: 10.1002/cphc.201400062.
- [23] Pei-Xi Wang, Wadood Y. Hamad, and Mark J. MacLachlan. Structure and transformation of tactoids in cellulose nanocrystal suspensions. *Nature Communications*, 7:11515, May 2016. doi: 10.1038/ncomms11515. URL <https://doi.org/10.1038/ncomms11515>.
- [24] J.-F. Revol, H. Bradford, J. Giasson, R.H. Marchessault, and D.G. Gray. Helicoidal self-ordering of cellulose microfibrils in aqueous suspension. *International Journal of Biological Macromolecules*, 14(3):170 – 172, 1992. ISSN 0141-8130. doi: [https://doi.org/10.1016/0141-8130\(92\)90001-9](https://doi.org/10.1016/0141-8130(92)90001-9).

//doi.org/10.1016/S0141-8130(05)80008-X. URL <http://www.sciencedirect.com/science/article/pii/S014181300580008X>.

- [25] Subrahmanyam Chandrasekhar. Surface tension of liquid crystals. *Molecular Crystals and Liquid Crystals*, 2(1-2):71–80, 1966. doi: 10.1080/15421406608083061. URL <https://doi.org/10.1080/15421406608083061>.
- [26] Oleg D Lavrentovich. Topological defects in dispersed liquid crystals, or words and worlds around liquid crystal drops. *Liquid Crystals*, 24(1):117–126, 1998.
- [27] A. V. Kaznacheev, M. M. Bogdanov, and S. A. Taraskin. The nature of prolate shape of tactoids in lyotropic inorganic liquid crystals. *Journal of Experimental and Theoretical Physics*, 95:57–63, 07 2002. doi: 10.1134/1.1499901. URL <https://doi.org/10.1134/1.1499901>.
- [28] AV Kaznacheev, MM Bogdanov, and AS Sonin. The influence of anchoring energy on the prolate shape of tactoids in lyotropic inorganic liquid crystals. *Journal of Experimental and Theoretical Physics*, 97(6):1159–1167, 2003.
- [29] Peter Prinsen and Paul van der Schoot. Shape and director-field transformation of tactoids. *Physical Review E*, 68:021701, Aug 2003. doi: 10.1103/PhysRevE.68.021701. URL <https://link.aps.org/doi/10.1103/PhysRevE.68.021701>.
- [30] P Prinsen and P. van der Schoot. Continuous director-field transformation of nematic tactoids. *The European Physical Journal E*, 13(1):35–41, 2004.
- [31] P Prinsen and P van der Schoot. Parity breaking in nematic tactoids. *Journal of Physics: Condensed Matter*, 16(49):8835, 2004.
- [32] R. M. W. van Bijnen, R. H. J. Otten, and P. van der Schoot. Texture and shape of two-dimensional domains of nematic liquid crystals. *Physical Review E*, 86:051703, Nov 2012. doi: 10.1103/PhysRevE.86.051703. URL <https://link.aps.org/doi/10.1103/PhysRevE.86.051703>.
- [33] Ronald H. J. Otten and Paul van der Schoot. Deformable homeotropic nematic droplets in a magnetic field. *The Journal of Chemical Physics*, 137:154901, Jan 2012. doi: 10.1063/1.4756946. URL <https://doi.org/10.1063/1.4756946>.
- [34] J. C. Everts, M. T. J. J. M. Punter, S. Samin, P. van der Schoot, and R. van Roij. A landau-de gennes theory for hard colloidal rods: Defects and tactoids. *The Journal*

- of Chemical Physics*, 144:194901, Jan 2016. doi: 10.1063/1.4948785. URL <https://doi.org/10.1063/1.4948785>.
- [35] Pierre Gilles De Gennes and Jacques Prost. *The physics of liquid crystals*. Oxford University Press, 1993.
- [36] Paul van der Schoot. Remarks on the interfacial tension in colloidal systems. *The Journal of Physical Chemistry B*, 103(42):8804–8808, 1999.
- [37] D Marenduzzo, E Orlandini, and JM Yeomans. Permeative flows in cholesteric liquid crystals. *Physical Review Letters*, 92(18):188301, 2004.
- [38] R D Williams. Two transitions in tangentially anchored nematic droplets. *Journal of Physics A: Mathematical and General*, 19(16):3211–3222, nov 1986. doi: 10.1088/0305-4470/19/16/019. URL <https://doi.org/10.1088/0305-4470/19/16/019>.
- [39] Davide Vanzo, Matteo Ricci, Roberto Berardi, and Claudio Zannoni. Shape, chirality and internal order of freely suspended nematic nanodroplets. *Soft Matter*, 8(47):11790–11800, 2012.
- [40] Luuk Metselaar, Ivan Dozov, Krassimira Antonova, Emmanuel Belamie, Patrick Davidson, Julia M. Yeomans, and Amin Doostmohammadi. Electric-field-induced shape transition of nematic tactoids. *Physical Review E*, 96:022706, Aug 2017. doi: 10.1103/PhysRevE.96.022706. URL <https://link.aps.org/doi/10.1103/PhysRevE.96.022706>.
- [41] Luuk Metselaar. Private communication, 2019.
- [42] E G Virga. Variational theories for liquid crystals. (*Chapman and Hall/CRC, Boca Raton*, 1994), 2015.
- [43] A Rapini and M Papoular. Distorsion d’une lamelle nématique sous champ magnétique conditions d’ancrage aux parois. *Le Journal de Physique Colloques*, 30(C4):C4–54, 1969.
- [44] Zheng Yu Chen and Jaan Noolandi. Numerical solution of the onsager problem for an isotropic-nematic interface. *Physical Review A*, 45(4):2389, 1992.

- [45] Lev Davidovich Landau and Evgenii Mikhailovich Lifshitz. *Course of theoretical physics*. Elsevier, 2013.
- [46] Masao Doi and Samuel Frederick Edwards. *The theory of polymer dynamics*. Oxford University Press, 1988.
- [47] BI Lev, VG Nazarenko, AB Nych, and PM Tomchuk. Deformation and instability of nematic drops in an external electric field. *Journal of Experimental and Theoretical Physics Letters*, 71(6):262–265, 2000.
- [48] JP Straley. The gas of long rods as a model for lyotropic liquid crystals. *Molecular Crystals and Liquid Crystals*, 22(3-4):333–357, 1973.
- [49] Theo Odijk. Elastic constants of nematic solutions of rod-like and semi-flexible polymers. *Liquid Crystals*, 1(6):553–559, 1986.
- [50] Gert Jan Vroege and Henk NW Lekkerkerker. Phase transitions in lyotropic colloidal and polymer liquid crystals. *Reports on Progress in Physics*, 55(8):1241, 1992.
- [51] HH Wensink and GJ Vroege. Isotropic–nematic phase behavior of length-polydisperse hard rods. *The Journal of Chemical Physics*, 119(13):6868–6882, 2003.
- [52] AR Khokhlov and AN Semenov. Influence of external field on the liquid-crystalline ordering in the solutions of stiff-chain macromolecules. *Macromolecules*, 15(5):1272–1277, 1982.
- [53] AN Semenov. Interaction of point defects in a nematic liquid. *Europhysics Letters*, 46(5):631, 1999.
- [54] Weiliang Chen and Derek G Gray. Interfacial tension between isotropic and anisotropic phases of a suspension of rodlike particles. *Langmuir*, 18(3):633–637, 2002.
- [55] ÉV Generalova, AV Kaznacheev, and AS Sonin. Effect of magnetic field on lyotropic nematic in the vanadium pentoxide ( $V_2O_5$ )-water system. *Crystallography Reports*, 46(1):111–113, 2001.
- [56] Takahiro Sato and Akio Teramoto. On the frank elastic constants of lyotropic polymer liquid crystals. *Macromolecules*, 29(11):4107–4114, 1996.

- [57] Clarissa F Dietrich, Peter J Collings, Thomas Sottmann, Per Rudquist, and Frank Giesselmann. Extremely small twist elastic constants in lyotropic nematic liquid crystals. *Proceedings of the National Academy of Sciences*, 117(44):27238–27244, 2020.
- [58] AA Verhoeff, RHJ Otten, Paul van der Schoot, and HNW Lekkerkerker. Magnetic field effects on tactoids of plate-like colloids. *The Journal of Chemical Physics*, 134(4):044904, 2011.
- [59] AA Verhoeff, IA Bakelaar, RHJ Otten, PPAM van der Schoot, and HNW Lekkerkerker. Tactoids of plate-like particles: Size, shape, and director field. *Langmuir*, 27(1):116–125, 2011.
- [60] Phil Lucht. Bipolar coordinates and the two-cylinder capacitor. *Rimrock Digital Technology, Salt Lake City, Utah*, 84103, 2015.
- [61] [https://en.wikipedia.org/wiki/bipolar\\_coordinates](https://en.wikipedia.org/wiki/bipolar_coordinates), 2024. URL [https://en.wikipedia.org/wiki/Bipolar\\_coordinates](https://en.wikipedia.org/wiki/Bipolar_coordinates).
- [62] Massimo Bagnani, Paride Azzari, Salvatore Assenza, and Raffaele Mezzenga. Six-fold director field configuration in amyloid nematic and cholesteric phases. *Scientific Reports*, 9(1):1–9, 2019.
- [63] Pei-Xi Wang and Mark J MacLachlan. Liquid crystalline tactoids: ordered structure, defective coalescence and evolution in confined geometries. *Philosophical Transactions of the Royal Society A: Mathematical, Physical and Engineering Sciences*, 376(2112):20170042, 2018.
- [64] Gustav Nyström and Raffaele Mezzenga. Liquid crystalline filamentous biological colloids: Analogies and differences. *Current Opinion in Colloid & Interface Science*, 38:30–44, 2018.
- [65] Rishikesh K Bharadwaj, Timothy J Bunning, and BL Farmer. A mesoscale modelling study of nematic liquid crystals confined to ellipsoidal domains. *Liquid Crystals*, 27(5):591–603, 2000.
- [66] Andrew DeBenedictis and Timothy J Atherton. Shape minimisation problems in liquid crystals. *Liquid Crystals*, 43(13-15):2352–2362, 2016.
- [67] RH Tromp and P van der Schoot. Quench-induced nematic textures of wormlike micelles. *Physical Review E*, 53(1):689, 1996.

- [68] Siyu Li, Polly Roy, Alex Travesset, and Roya Zandi. Why large icosahedral viruses need scaffolding proteins. *Proceedings of the National Academy of Sciences*, 115(43):10971–10976, 2018.
- [69] Roya Zandi, Bogdan Dragnea, Alex Travesset, and Rudolf Podgornik. On virus growth and form. *Physics Reports*, 847:1–102, mar 2020. ISSN 0370-1573. doi: 10.1016/J.PHYSREP.2019.12.005. URL <https://www.sciencedirect.com/science/article/pii/S0370157320300016?dgcid=coauthor>.
- [70] Anja Kuhnhold and Paul van der Schoot. Structure of nematic tactoids of hard rods. *The Journal of Chemical Physics*, 156(10):104501, 2022.
- [71] Sin-Doo Lee. Comment on effects of elongational flow on the isotropic–nematic phase transition in rod-like systems. *The Journal of Chemical Physics*, 86(11):6567–6568, 1987.
- [72] Szabolcs Varga, George Jackson, and Istvan Szalai. External field induced paranematic-nematic phase transitions in rod-like systems. *Molecular Physics*, 93(3):377–387, 1998.
- [73] Mohammadamin Safdari, Roya Zandi, and Paul van der Schoot. Effect of electric fields on the director field and shape of nematic tactoids. *Physical Review E*, 103(6):062703, 2021.
- [74] Weiliang Chen and Derek G Gray. Interfacial tension between isotropic and anisotropic phases of a suspension of rodlike particles. *Langmuir*, 18(3):633–637, 2002.
- [75] D van der Beek, H Reich, P van der Schoot, M Dijkstra, Tanja Schilling, R Vink, Matthias Schmidt, RHHG van Roij, and H Lekkerkerker. Isotropic-nematic interface and wetting in suspensions of colloidal platelets. *Physical Review Letters*, 97(8):087801, 2006.
- [76] Hamed Almohammadi, Massimo Bagnani, and Raffaele Mezzenga. Flow-induced order–order transitions in amyloid fibril liquid crystalline tactoids. *Nature Communications*, 11(1):5416, 2020.
- [77] Hamed Almohammadi, Sayyed Ahmad Khadem, Massimo Bagnani, Alejandro D Rey, and Raffaele Mezzenga. Shape and structural relaxation of colloidal tactoids. *Nature Communications*, 13(1):2778, 2022.

- [78] Hamed Almohammadi, Sandra Martinek, Ye Yuan, Peter Fischer, and Raffaele Mezzenga. Disentangling kinetics from thermodynamics in heterogeneous colloidal systems. *Nature Communications*, 14(1):607, 2023.
- [79] Massimo Bagnani, Gustav Nystrom, Cristiano De Michele, and Raffaele Mezzenga. Amyloid fibrils length controls shape and structure of nematic and cholesteric tactoids. *ACS Nano*, 13(1):591–600, 2018.
- [80] Stephen Wolfram. *The MATHEMATICA® book, version 4*. Cambridge university press, 1999.
- [81] Masao Doi. Onsager’s variational principle in soft matter. *J. Phys.: Condens. Matter*, 23:284118, 2011.
- [82] PM Lerman. Fitting segmented regression models by grid search. *Journal of the Royal Statistical Society Series C: Applied Statistics*, 29(1):77–84, 1980.
- [83] Bin Li, Vincenzino Vivacqua, Mojtaba Ghadiri, Zhiqian Suna, Zhenbo Wang, and Xiaoyu Li. Droplet deformation under pulsatile electric fields. *Chemical Engineering Research and Design*, 127:180–188, 2017. doi: 10.1016/j.cherd.2017.09.024. URL <https://doi.org/10.1016/j.cherd.2017.09.024>.
- [84] Robijn F Bruinsma, Gijs J L Wuite, and Wouter H Roos. Physics of viral dynamics. *Nature Reviews Physics*, 3(2):76–91, 2021. URL <https://doi.org/10.1038/s42254-020-00267-1>.
- [85] Michael F Hagan. Modeling viral capsid assembly. *Adv Chem Phys*, 155:1–68, 2014. URL <https://doi.org/10.1002/9781118755815.ch01>.
- [86] Eric C Dykeman, Peter G Stockley, and Reidun Twarock. Solving a levinthal’s paradox for virus assembly identifies a unique antiviral strategy. *PNAS*, 111(14):5361–5366, 2014.
- [87] Birgit Rabe, Mildred Delaleau, Andreas Bischof, Michael Foss, Irina Sominskaya, Paul Pumpens, Christian Cazenave, Michel Castroviejo, and Michael Kann. Nuclear entry of hepatitis b virus capsids involves disintegration to protein dimers followed by nuclear reassociation to capsids. *PLoS Pathogens*, 5(8), 2009. doi: 10.1371/journal.ppat.1000563.

- [88] Siyu Li and Roya Zandi. Biophysical modeling of sars-cov-2 assembly: Genome condensation and budding. *Viruses*, 14(10):2089, 2022.
- [89] Hsiang-Ku Lin, Paul van der Schoot, and Roya Zandi. Impact of charge variation on the encapsulation of nanoparticles by virus coat proteins. *Physical biology*, 9(6): 066004, 2012.
- [90] J.B. Bancroft and Ernest Hiebert. Formation of an infectious nucleoprotein from protein and nucleic acid isolated from a small spherical virus. *Virology*, 32(2):354–356, 1967. URL [https://doi.org/10.1016/0042-6822\(67\)90284-X](https://doi.org/10.1016/0042-6822(67)90284-X).
- [91] J. B. Bancroft. The self-assembly of spherical plant viruses. In Kenneth M. Smith, Max A. Lauffer, and Frederik B. Bang, editors, *Advances in Virus Research*, volume 16, pages 99–134. Academic Press, 1970. URL [https://doi.org/10.1016/S0065-3527\(08\)60022-6](https://doi.org/10.1016/S0065-3527(08)60022-6).
- [92] K. W. Adolph and P. J. G. Butler. Studies on the assembly of a spherical plant virus: I. states of aggregation of the isolated protein. *Journal of Molecular Biology*, 88(2): 327–341, 1974. URL [https://doi.org/10.1016/0022-2836\(74\)90485-9](https://doi.org/10.1016/0022-2836(74)90485-9).
- [93] Nancy L. Goicochea, Mrinmoy De, Vincent M. Rotello, Suchetana Mukhopadhyay, and Bogdan Dragnea. Core-like particles of an enveloped animal virus can self-assemble efficiently on artificial templates. *Nano Letters*, 7(8):2281–2290, 2007. ISSN 1530-6984. doi: 10.1021/nl070860e.
- [94] Qing Liu, Ahmed Shaukat, Daniella Kyllönen, and Mauri A. Kostianen. Polyelectrolyte encapsulation and confinement within protein cage-inspired nanocompartments. *Pharmaceutics*, 13(10):1551, 2021. doi: 10.3390/pharmaceutics13101551.
- [95] Rees F. Garmann, Mauricio Comas-Garcia, Charles M. Knobler, and William M. Gelbart. Physical principles in the self-assembly of a simple spherical virus. *Acc. Chem. Res.*, 49(1):48–55, 2016. doi: 10.1021/acs.accounts.5b00350.
- [96] Li He, Zachary Porterfield, Paul van der Schoot, Adam Zlotnick, and Bogdan Dragnea. Hepatitis virus capsid polymorph stability depends on encapsulated cargo size. *ACS Nano*, 7(10):8447–8454, 2013. URL <https://doi.org/10.1021/nn4017839>.
- [97] H. S. Savithri and John W. Erickson. The self-assembly of the cowpea strain of southern bean mosaic virus: Formation of  $t = 1$  and  $t = 3$  nucleatioprotein particles. *Virology*, 126(1):328–335, 1983. doi: 10.1016/0042-6822(83)90482-8.

- [98] Kevin Bond, Irina B Tsvetkova, Joseph Che-Yen Wang, Martin F Jarrold, and Bogdan Dragnea. Virus assembly pathways: Straying away but not too far. *Small*, 16(51):2004475, 2020.
- [99] Sanaz Panahandeh, Siyu Li, Bogdan Dragnea, and Roya Zandi. Virus assembly pathways inside a host cell. *ACS Nano*, 16(1):317–327, 2022. doi: 10.1021/acsnano.1c06335.
- [100] Stefan Paquay, Halim Kusumaatmaja, David J. Wales, Roya Zandi, and Paul van der Schoot. Energetically favoured defects in dense packings of particles on spherical surfaces. *Soft Matter*, 12:5708–5717, 2016. doi: 10.1039/C6SM00489J.
- [101] Sanaz Panahandeh, Siyu Li, and Roya Zandi. The equilibrium structure of self-assembled protein nano-cages. *Nanoscale*, 10(48):22802–22809, 2018.
- [102] A Zlotnick, N Cheng, J F Conway, F P Booy, A C Steven, S J Stahl, and P T P T Wingfield. Dimorphism of hepatitis b virus capsids is strongly influenced by the c-terminus of the capsid protein. *Biochemistry*, 35(23):7412–7421, 1996. doi: 10.1021/bi9604800.
- [103] Xinyu Sun, Dong Li, Zhaoshuai Wang, Qiao Liu, Yinan Wei, and Tianbo Liu. A dimorphism shift of hepatitis b virus capsids in response to ionic conditions. *Nanoscale*, 10:16984–16989, 2018. doi: 10.1039/c8nr03370f. URL <https://doi.org/10.1039/C8NR03370F>.
- [104] Roya Zandi and Paul van der Schoot. Size regulation of ss-RNA viruses. *Biophysical Journal*, 96(1):9–20, 2009. URL <https://doi.org/10.1529/biophysj.108.137489>.
- [105] Paul van der Schoot and Roya Zandi. Impact of the topology of viral rnas on their encapsulation by virus coat proteins. *J. Biol. Phys.*, 39(2):289–299, 2013. doi: 10.1007/s10867-013-9307-y.
- [106] Pepijn Moerman, Paul van der Schoot, and Willem Kegel. Kinetics versus thermodynamics in virus capsid polymorphism. *Journal of Physical Chemistry B*, 120(26):6003—6009, 2016. URL <https://doi.org/10.1021/acs.jpcc.6b01953>.
- [107] K W Adolph and P J G Butler. Assembly of a spherical plant virus. *Philosophical Transactions of the Royal Society of London B Biological Sciences*, 276(943):113–112, 1976. URL <https://doi.org/10.1098/rstb.1976.0102>.

- [108] L. Lavelle, M. Gingery, M. Phillips, W. M. Gelbart, C. M. Knobler, R. D. Cadena-Nava, J. R. Vega-Acosta, L. A. Pinedo-Torres, and J. Ruiz-Garcia. Phase diagram of self-assembled viral capsid protein polymorphs. *The Journal of Physical Chemistry B*, 113(12):3813–3819, 2009.
- [109] Siyu Li, Gonca Erdemci-Tandogan, Jef Wagner, Paul van der Schoot, and Roya Zandi. Impact of a nonuniform charge distribution on virus assembly. *Phys. Rev. E*, 96(2):022401, 2017. ISSN 24700053. doi: 10.1103/PhysRevE.96.022401.
- [110] Yinan Dong, Siyu Li, and Roya Zandi. Effect of the charge distribution of virus coat proteins on the length of packaged rnas. *Physical Review E*, 102(6):062423, 2020. doi: 10.1103/PhysRevE.102.062423.
- [111] Peng Ni, Zhao Wang, Xiang Ma, Nayaran Chandra Das, Paul Sokol, Wah Chiu, Bogdan Dragnea, Michael Hagan, and C. Cheng Kao. An examination of the electrostatic interactions between the N-terminal tail of the Brome Mosaic Virus coat protein and encapsidated RNAs. *J. Mol. Biol.*, 419(5):284–300, 2012. doi: 10.1016/j.jmb.2012.03.023.
- [112] Alireza Ramezani. *Dynamic Processes in Biological Systems: From Capsid Disassembly to Tissue Growth and Bacterial Chemotaxis*. University of California, Riverside, 2023.
- [113] Pablo Ceres and Adam Zlotnick. Weak proteinprotein interactions are sufficient to drive assembly of hepatitis b virus capsids. *Biochemistry*, 41(39):11525–11531, 2002. doi: 10.1021/bi0261645. URL <https://doi.org/10.1021/bi0261645>.
- [114] Robijn F. Bruinsma, William M. Gelbart, David Reguera, Joseph Rudnick, and Roya Zandi. Viral self-assembly as a thermodynamic process. *Physical Review Letters*, 90:248101–248105, June 2003. URL <https://doi.org/10.1103/PhysRevLett.90.248101>.
- [115] D.L.D. Caspar. Assembly and stability of the tobacco mosaic virus particle. volume 18, pages 37–121. Academic Press, 1964. URL [https://doi.org/10.1016/S0065-3233\(08\)60268-5](https://doi.org/10.1016/S0065-3233(08)60268-5).
- [116] W. Chiu, R.M. Burnett, and R.L. Garcea. *Structural Biology of Viruses*. Oxford University Press, 1997.

- [117] Alexander McPherson. Micelle formation and crystallization as paradigms for virus assembly. *BioEssays*, 27(4):447–458, 2005. URL <https://doi.org/10.1002/bies.20196>.
- [118] Adam Zlotnick. To build a virus capsid. an equilibrium model of the self assembly of polyhedral protein complexes. *Journal of Molecular Biology*, 241(1):59–67, 1994. doi: 10.1006/jmbi.1994.1473. URL <https://doi.org/10.1006/jmbi.1994.1473>.
- [119] T. Keef, C. Micheletti, and R. Twarock. Master equation approach to the assembly of viral capsids. *J. Theor. Biol.*, 242(3):713–721, 2006. URL <https://doi.org/10.1016/j.jtbi.2006.04.023>.
- [120] Roya Zandi, Paul van der Schoot, David Reguera, Willem Kegel, and Howard Reiss. Classical nucleation theory of virus capsids. *Biophysical Journal*, 90(6):1939–1948, 2006. URL <https://doi.org/10.1529/biophysj.105.072975>.
- [121] C. Berthet-Colominas, M. Cuillel, M. H. J. Koch, P. Vachette, and B. Jacrot. Kinetic study of the self-assembly of brome mosaic virus capsid. *Eur. Biophys. J.*, 15:159–168, 1987. doi: 10.1007/BF00263680. URL <https://doi.org/10.1007/BF00263680>.
- [122] D. C. Rapaport. Molecular dynamics simulation: a tool for exploration and discovery using simple models. *Journal of Physics: Condensed Matter*, 26(50):503104, 2014. doi: 10.1088/0953-8984/26/50/503104.
- [123] Rees F. Garmann, Aaron M. Goldfain, and Vinothan N. Manoharan. Measurements of the self-assembly kinetics of individual viral capsids around their rna genome. *Proc. Nat. Acad. Sci.*, 116(45):22485–22490, 2019. doi: 10.1073/pnas.190922311.
- [124] Roya Zandi, Bogdan Dragnea, Alex Travesset, and Rudolf Podgornik. On virus growth and form. *Physics Reports*, 847:1–102, 1 2020. ISSN 03701573. doi: 10.1016/j.physrep.2019.12.005.
- [125] Didier Law-Hine, Anil K. Sahoo, Virginie Bailleux, Mehdi Zeghal, Sylvain Prevost, Prabal K. Maiti, Stephane Bressanelli, Doru Constantin, and Guillaume Tresset. Reconstruction of the disassembly pathway of an icosahedral viral capsid and shape determination of two successive intermediates. *The Journal of Physical Chemistry Letters*, 6(17):3471–3476, 2015. URL <https://doi.org/10.1021/acs.jpcllett.5b01478>.

- [126] Antonio Šiber and Rudolf Podgornik. Nonspecific interactions in spontaneous assembly of empty *versus* functional single-stranded rna viruses. *Phys. Rev. E*, 78(5):051915, 2008. doi: 10.1103/PhysRevE.78.051915.
- [127] Maelenn Chevreuil, Didier Law-Hine, Jingzhi Chen, Stéphane Bressanelli, Sophie Combet, Doru Constantin, Jéril Degrouard, Johannes Möller, Mehdi Zeghal, and Guillaume Tresset. Nonequilibrium self-assembly dynamics of icosahedral viral capsids packaging genome or polyelectrolyte. *Nature Communications*, 9(1):3071, 2018. ISSN 2041-1723. doi: 10.1038/s41467-018-05426-8.
- [128] O. M. Elrad and M. F. Hagan. Encapsulation of a Polymer by an Icosahedral Virus. *Phys. Biol.*, 7:045003, 2010. doi: 10.1088/1478-3975/7/4/045003.
- [129] Sanaz Panahandeh, Siyu Li, Laurent Marichal, Rafael Leite Rubim, Guillaume Tresset, and Roya Zandi. How a virus circumvents energy barriers to form symmetric shells. *ACS nano*, 14(3):3170–3180, 2020.
- [130] Nathan M Willy, Joshua P Ferguson, Ata Akatay, Scott Huber, Umidahan Djakbarova, Salih Silahli, Cemal Cakez, Farah Hasan, Henry C Chang, Alex Travesset, et al. De novo endocytic clathrin coats develop curvature at early stages of their formation. *Developmental cell*, 56(22):3146–3159, 2021.
- [131] Maelenn Chevreuil, Lauriane Lecoq, Shishan Wang, Laetitia Gargowitsch, Naïma Nhiri, Eric Jacquet, Thomas Zinn, Sonia Fieulaine, Stéphane Bressanelli, and Guillaume Tresset. Nonsymmetrical dynamics of the hbv capsid assembly and disassembly evidenced by their transient species. *The Journal of Physical Chemistry B*, 124(45):9987–9995, 2020. URL <https://doi.org/10.1021/acs.jpccb.0c05024>.
- [132] Sushmita Singh and Adam Zlotnick. Observed hysteresis of virus capsid disassembly is implicit in kinetic models of assembly. *Journal of Biological Chemistry*, 278(20):18249–18255, 2003. doi: 10.1074/jbc.M211408200.
- [133] Zhaleh Ghaemi, Martin Gruebele, and Emad Tajkhorshid. Molecular mechanism of capsid disassembly in hepatitis b virus. *Proc. Nat. Acad. Sci. USA*, 118(36):e2102530118, 2021. doi: 10.1073/pnas.2102530118.
- [134] Suzanne B. P. E. Timmermans, Alireza Ramezani, Toni Montalvo, Mark Nguyen, Paul van der Schoot, Jan C. M. van Hest, and Roya Zandi. The dynamics of viruslike capsid assembly and disassembly. *Journal of the American Chemical Society*, 144(28):12608–12612, 2022. doi: 10.1021/jacs.2c04074. URL <https://doi.org/10.1021/jacs.2c04074>. PMID: 35792573.

- [135] J. R. Vega-Acosta, R. D. Cadena-Nava, W. M. Gelbart, C. M. Knobler, and J. Ruiz-García. Electrophoretic mobilities of a viral capsid, its capsid protein, and their relation to viral assembly. *The Journal of Physical Chemistry B*, 118(8):1984–1989, 2014. doi: 10.1021/jp407379t.
- [136] P. C. Hohenberg and B. I. Halperin. Theory of dynamic critical phenomena. *Reviews of Modern Physics*, 49(3):435, 1977.
- [137] Paul van der Schoot and Roya Zandi. Kinetic theory of virus capsid assembly. *Physical Biology*, 4(4):296–304, 2007. URL <https://doi.org/10.1088/1478-3975/4/4/006>.
- [138] D. C. Rappaport. Role of reversibility in viral capsid growth: A paradigm for self-assembly. *Phys. Rev. Lett.*, 101(18):186101, 2008. URL <https://doi.org/10.1103/PhysRevLett.101.186101>.
- [139] Yufang Hu, Roya Zandi, Charles M Knobler, and William M Gelbart. Packaging of a polymer by a viral capsid: the interplay between polymer length and capsid size. *Biophysical Journal*, 94(4):1428–1436, 2008. URL <https://doi.org/10.1529/biophysj.107.117473>.
- [140] Willem K Kegel and Paul van der Schoot. Competing hydrophobic and screened-coulomb interactions in hepatitis b virus capsid assembly. *Biophysical Journal*, 86(6):3905–3913, 2004. URL <https://doi.org/10.1529/biophysj.104.040055>.
- [141] Pauli Virtanen, Ralf Gommers, Travis E. Oliphant, Matt Haberland, Tyler Reddy, David Cournapeau, Evgeni Burovski, Pearu Peterson, Warren Weckesser, Jonathan Bright, Stéfan J. van der Walt, Matthew Brett, Joshua Wilson, K. Jarrod Millman, Nikolay Mayorov, Andrew R. J. Nelson, Eric Jones, Robert Kern, Eric Larson, C J Carey, İlhan Polat, Yu Feng, Eric W. Moore, Jake VanderPlas, Denis Laxalde, Josef Perktold, Robert Cimrman, Ian Henriksen, E. A. Quintero, Charles R. Harris, Anne M. Archibald, Antônio H. Ribeiro, Fabian Pedregosa, Paul van Mulbregt, and SciPy 1.0 Contributors. SciPy 1.0: Fundamental Algorithms for Scientific Computing in Python. *Nature Methods*, 17:261–272, 2020. doi: 10.1038/s41592-019-0686-2.
- [142] Douglas C. Montgomery. *Design and analysis of experiments*. John Wiley & Sons, Inc., Hoboken, New Jersey, eighth edition, 2013.
- [143] Lars Onsager. The effects of shape on the interaction of colloidal particles. *Annals of the New York Academy of Sciences*, 51(4):627–659, 1949.

- [144] Ho No Wo Lekkerkerker, Pho Coulon, and van der R Haegen. On the isotropic-liquid crystal phase separation in a solution of rodlike particles of different lengths. *The Journal of chemical physics*, 80(7):3427–3433, 1984.
- [145] Patrick W Oakes, Jorge Viamontes, and Jay X Tang. Growth of tactoidal droplets during the first-order isotropic to nematic phase transition of f-actin. *Physical Review E*, 75(6):061902, 2007.
- [146] Jonathan V Selinger. Interpretation of saddle-splay and the oseen-frank free energy in liquid crystals. *Liquid Crystals Reviews*, 6(2):129–142, 2018.
- [147] Frederick C Frank. I. liquid crystals. on the theory of liquid crystals. *Discussions of the Faraday Society*, 25:19–28, 1958.
- [148] GE Volovik and OD Lavrentovich. Topological dynamics of defects: boojums in nematic drops. *Zh. Eksp. Teor. Fiz.*, 85(6):1997–2010, 1983.
- [149] Liubov V Toropova, Eugenia V Makoveeva, Sergei I Osipov, Alexey P Malygin, Yang Yang, and Dmitri V Alexandrov. Nucleation and growth of an ensemble of crystals during the intermediate stage of a phase transition in metastable liquids. *Crystals*, 12(7):895, 2022.
- [150] Paul van der Schoot. *Molecular Theory of Nematic (and Other) Liquid Crystals: An Introduction*. Springer Nature, 2022.
- [151] Zvonimir Dogic. Filamentous phages as a model system in soft matter physics. *Frontiers in microbiology*, 7:1013, 2016.
- [152] AS Sonin, NA Churochkina, AV Kaznacheev, and AV Golovanov. Mineral liquid crystals. *Colloid Journal*, 79:421–450, 2017.
- [153] Shari P Finner, Ilian Pihlajamaa, and Paul van der Schoot. Geometric percolation of hard nanorods: The interplay of spontaneous and externally induced uniaxial particle alignment. *The Journal of Chemical Physics*, 152(6):064902, 2020.
- [154] Michel PB van Bruggen, Felix M van der Kooij, and Henk NW Lekkerkerker. Liquid crystal phase transitions in dispersions of rod-like colloidal particles. *Journal of Physics: Condensed Matter*, 8(47):9451, 1996.

- [155] Abul K Tarafder, Andriko von K ugelgen, Adam J Mellul, Ulrike Schulze, Dirk GAL Aarts, and Tanmay AM Bharat. Phage liquid crystalline droplets form occlusive sheaths that encapsulate and protect infectious rod-shaped bacteria. *Proceedings of the National Academy of Sciences*, 117(9):4724–4731, 2020.
- [156] M Primicerio. Eg virga, variational theories for liquid crystals”. *Chapman and Hall, London*, 30:736, 1995. doi: 10.1103/PhysRevB.98.167401. URL <https://link.aps.org/doi/10.1103/PhysRevB.98.167401>.
- [157] Alexander Bryan Clark, Mohammadamin Safdari, Selim Zoorob, Roya Zandi, and Paul van der Schoot. Relaxational dynamics of the t-number conversion of virus capsids. *The Journal of Chemical Physics*, 159(8), 2023.
- [158] Kalouna Kra, Siyu Li, Laetitia Gargowitsch, J ril Degrouard, Javier P rez, Roya Zandi, St phane Bressanelli, and Guillaume Tresset. Energetics and kinetic assembly pathways of hepatitis b virus capsids in the presence of antivirals. *ACS nano*, 2023.
- [159] Zan Lu, Yunfeng Chao, Yu Ge, Javad Foroughi, Yong Zhao, Caiyun Wang, Hairu Long, and Gordon G Wallace. High-performance hybrid carbon nanotube fibers for wearable energy storage. *Nanoscale*, 9(16):5063–5071, 2017.
- [160] Francesca Mirri, Anson WK Ma, Tienyi T Hsu, Natnael Behabtu, Shannon L Eichmann, Colin C Young, Dmitri E Tsentalovich, and Matteo Pasquali. High-performance carbon nanotube transparent conductive films by scalable dip coating. *ACS nano*, 6(11):9737–9744, 2012.
- [161] Virginia A Davis, Lars M Ericson, A Nicholas G Parra-Vasquez, Hua Fan, Yuhuang Wang, Valentin Prieto, Jason A Longoria, Sivarajan Ramesh, Rajesh K Saini, Carter Kittrell, et al. Phase behavior and rheology of swnts in superacids. *Macromolecules*, 37(1):154–160, 2004.
- [162] Natnael Behabtu, Colin C Young, Dmitri E Tsentalovich, Olga Kleinerman, Xuan Wang, Anson WK Ma, E Amram Bengio, Ron F Ter Waarbeek, Jorrit J De Jong, Ron E Hoogerwerf, et al. Strong, light, multifunctional fibers of carbon nanotubes with ultrahigh conductivity. *science*, 339(6116):182–186, 2013.
- [163] A Nicholas G Parra-Vasquez, Natnael Behabtu, Micah J Green, Cary L Pint, Colin C Young, Judith Schmidt, Ellina Kesselman, Anubha Goyal, Pulickel M Ajayan, Yachin Cohen, et al. Spontaneous dissolution of ultralong single-and multiwalled carbon nanotubes. *Acs Nano*, 4(7):3969–3978, 2010.

- [164] Virginia A Davis, A Nicholas G Parra-Vasquez, Micah J Green, Pradeep K Rai, Natnael Behabtu, Valentin Prieto, Richard D Booker, Judith Schmidt, Ellina Kesselman, Wei Zhou, et al. True solutions of single-walled carbon nanotubes for assembly into macroscopic materials. *Nature nanotechnology*, 4(12):830–834, 2009.
- [165] Eric Grelet and Richa Rana. From soft to hard rod behavior in liquid crystalline suspensions of sterically stabilized colloidal filamentous particles. *Soft Matter*, 12(20):4621–4627, 2016.
- [166] Eric Grelet. Hard-rod behavior in dense mesophases of semiflexible and rigid charged viruses. *Physical Review X*, 4(2):021053, 2014.
- [167] Zvonimir Dogic and Seth Fraden. Ordered phases of filamentous viruses. *Current opinion in colloid & interface science*, 11(1):47–55, 2006.
- [168] Zvonimir Dogic, Kirstin R Purdy, Eric Grelet, Marie Adams, and Seth Fraden. Isotropic-nematic phase transition in suspensions of filamentous virus and the neutral polymer dextran. *Physical Review E—Statistical, Nonlinear, and Soft Matter Physics*, 69(5):051702, 2004.
- [169] Jorge Viamontes and Jay X Tang. Continuous isotropic-nematic liquid crystalline transition of f-actin solutions. *Physical Review E*, 67(4):040701, 2003.
- [170] Zvonimir Dogic and Seth Fraden. Development of model colloidal liquid crystals and the kinetics of the isotropic–smectic transition. *Philosophical Transactions of the Royal Society of London. Series A: Mathematical, Physical and Engineering Sciences*, 359(1782):997–1015, 2001.
- [171] John D Bernal and Isidor Fankuchen. X-ray and crystallographic studies of plant virus preparations: I. introduction and preparation of specimens ii. modes of aggregation of the virus particles. *The Journal of general physiology*, 25(1):111, 1941.
- [172] HH Wensink and GJ Vroege. Isotropic–nematic phase behavior of length-polydisperse hard rods. *The Journal of chemical physics*, 119(13):6868–6882, 2003.
- [173] FC Bawden, NW Pirie, JD Bernal, and I Fankuchen. Liquid crystalline substances from virus-infected plants. *Nature*, 138(3503):1051–1052, 1936.
- [174] Micah J Green, A Nicholas G Parra-Vasquez, Natnael Behabtu, and Matteo Pasquali. Modeling the phase behavior of polydisperse rigid rods with attractive interactions

with applications to single-walled carbon nanotubes in superacids. *The Journal of chemical physics*, 131(8), 2009.